

https://dspace.org/

Computational study of oxynitride based strong materials

Okeke, Onyekwelu Uzodinma

2010-04-16T08:10:05Z
http://hdl.handle.net/10539/7998

Downloaded from a DSpace repository. https://dspace.org/

Computational Study of Oxynitride Based Strong Materials

ONYEKWELU UZODINMA OKEKE

A THESIS SUBMITTED TO THE FACULTY OF SCIENCE,
UNIVERSITY OF THE WITWATERSRAND, JOHANNESBURG,
IN FULFILMENT OF THE REQUIREMENTS FOR THE DEGREE
OF DOCTOR OF PHILOSOPHY

NOVEMBER 2009

Declaration

I declare that this thesis is my own, unaided work. It is being submitted for the degree of Doctor of Philosophy in the University of the Witwatersrand, Johannesburg. It has not been submitted before for any degree or examination in any other University.

_____

(Signature of candidate)

____ day of _____ 200 ____

Abstract

A spinel oxynitride material in the form M_3NO_3 (M = B, Al, Ga, or In) is considered to be derived from a reaction of the form $MN + M_2O_3 \rightarrow M_3NO_3$. Various possible phases of MN and M_2O_3 that could lead to M_3NO_3 oxynitride spinel material have been considered in the work. The structural, electronic, elastic properties and the relative stabilities of the bulk and the nature of the resulting vacancies or defect-related properties of these oxynitride spinel structures are investigated using *ab*-initio or first principles electronic structure methods based on density functional theory (DFT). The bulk oxynitride spinel structure containing B and Al atoms exhibit higher resistance to compression and shear than those containing Ga and In atoms and therefore, these are suggested to be potentially important hard materials possibly formed under extreme conditions. Calculated energetics of the proposed reaction favor the formation of oxynitride spinels containing Ga and In with such materials having potentially significant optoelectronic applications. From results on defective oxynitride systems, with a vacancy at octahedral or tetrahedral sites, it is suggested that the structural stability of the oxynitride spinel materials could be lowered.

In this thesis, a series of Tersoff empirical potentials for the bulk oxynitride spinel systems is proposed and tested by calculating the structural and elastic properties of the binary nitrides and M_3NO_3 oxynitride spinels using molecular dynamics simulation. The apparent success of treating some binary nitride systems using the Tersoff potential is used as a way forward to obtain a new parameter set that incorporates atomic features into a series of Tersoff potential for ternary oxynitrides spinel phases. The different thermodynamic properties of these oxynitride structure for varying temperature are also predicted such as the Debye temperature, thermal expansion co-efficient and specific heat. It is suggested that these materials will have thermal properties comparable to their binary nitride counterparts.

Acknowledgements

I would like to express my profound gratitude to my supervisor Professor John Edward Lowther, for the new concept on “computational material physics” he has introduced me to. Thank you for your guidance, encouragement and support throughout this project. Over the past three years our relationship has grown to be like father and son.

Many thanks to my family. I am indebted to my parents for standing by me throughout these years. To my brothers and sisters, your prayers made it a worthwhile. May God bless you all. No words are suitable to express my gratitude to my sweetheart Blessing. It was during the later part of this work that we both agreed for a future together, and I’d love to say a big piece of my heart belong to you. “mmwah”

Each individual in the research group and school of physics - no names mentioned and no one forgotten - being friends and colleague are mentioned, for kind support and encouragement. You guys have done great.

I would not fail to acknowledge my bosom friends Onwunta, Gideon, Naziga, Bolaji, and Henry. Your friendships were and are still valuable to me.

I would also like to acknowledge the financial support provided by DST/NRF Center of Excellence in Strong Materials, African Institute for Mathematical Sciences (AIMS), and the University of Witwatersrand, Johannesburg South Africa. Funding this research is well appreciated.

I appreciate and acknowledge the spiritual support from GodFirst City Church and West Campus Village Fellowship. Indeed the prayers of the righteous ones avails much. Thanks to you all.

My special thanks goes to God Almighty, my Father, Lord and Savior. Your love toward me is unending and everlasting. You are the portion of my inheritance and you maintain my lots (Ps. 16:5).

Publications and Patent

1. Onyekwelu U. Okeke and J. E. Lowther, **Theoretical Electronic Structures and Relative Stabilities of the Spinel Oxynitrides M_3NO_3 (*M* = B, Al, Ga, In)**, [*Phys. Rev. B*, 77, 094129 (2008)].

2. Onyekwelu U. Okeke and J. E. Lowther, **Molecular Dynamics of Binary Metal Nitrides and Ternary Oxynitrides**, [*Physica B*, 404, 3577 (2009)].

3. Onyekwelu U. Okeke and J. E. Lowther, ***Ab*-initio Study of Defects in Spinel-type *M*-O-N Oxynitride Structures (*M* = Al, Ga, In)**, [*in preparattion*].

4. Onyekwelu U. Okeke and J. E. Lowther, **Novel Spinel Structure Materials:**
   WO 2009/112934 A2, International Patent Reference: PCT/IB2009/00497 (2009).

Nne m! Ezigbo nne m Mrs. Comfort Okeke!!

Ọ bu n'ihi ihunanya, nkwado na okwukwe e nwere na ebe m nọ mere ọlu a jiri puta ihe.

To my uncle and his wife, Sir Charles and Lady Joy Nwaiwu, my life story cannot be written without having you in it. To Peter and Joyce Huyser, thanks for being my "lovely parents" in South Africa.

Contents

Declaration ii

Abstract iii

Acknowledgements iv

Publications and Patent v

List of Tables xi

List of Figures xv

1 Introduction **1**

1.1 Defining and Measuring Hardness 3

1.2 The Spinel Structure 4

1.3 Cation Arrangement in Spinels 7

1.4 Types of Spinel 9

1.5 Thesis Scope and Outline 10

2 A Review of Group-III Oxides and Nitrides **12**

2.1 Introduction 12

2.2 Forms of Group-III Oxides 13

2.2.1 Boron Oxide (B_2O_3) 13

2.2.2 Aluminum Oxide (Al_2O_3) 14

2.2.3 Gallium Oxide (Ga_2O_3) 15

2.2.4 Indium Oxide (In_2O_3) 16

2.3 Forms of Group-III Nitrides 18
2.3.1 Boron nitride (BN) 18
2.3.2 Aluminum Nitride (AlN) 19
2.3.3 Gallium Nitride (GaN) 20
2.3.4 Indium Nitride (InN) 20

3 Electronic Structure Methods 22

3.1 Introduction 22
3.2 Density Functional Theory 23
3.2.1 The Hohenberg-Kohn Theorem 25
3.2.2 Kohn-Sham Equations 27
3.3 Exchange-Correlation Functional 29
3.3.1 Local Density Approximation (LDA) 30
3.3.2 Generalized Gradient Approximation (GGA) 31
3.4 Plane Wave Pseudopotential Method 33
3.4.1 Plane Wave Basis Set 33
3.4.2 Monkhorst-Pack Grids 35
3.4.3 Pseudopotentials 35
3.5 The Vienna Ab-Initio Simulation Package (VASP) 37

4 Theoretical Study of Spinel Oxynitride M_3NO_3 39

4.1 Computational Parameters 39
4.2 Structural Properties of Spinels 40
4.3 Elastic Properties 45
4.3.1 The Equation of State Bulk Modulus 46
4.3.2 Estimation of the Elastic Constants 51
4.4 Electronic Structure 54
4.4.1 Electronic Density of States (DOS) and Band Structure 54

4.4.2 Electronic Charge Density 62
4.5 Relative Stability of Spinel 65
4.6 Conclusions 66

5 Molecular Dynamics Simulations 68
5.1 Intermolecular Potential Models 72
5.1.1 Introduction 72
5.1.2 Tersoff Potential 73
5.1.3 Tersoff Potential for Ternary Systems from a Binary Potential . . . 74
5.2 Integration Algorithm 77
5.3 Periodic Boundary Conditions 79
5.4 Computational Platforms 80
5.4.1 DL_POLY 80
5.4.2 GULP 81

6 Structural and Thermodynamics Properties of Spinel Oxynitrides 84
6.1 Structural Properties 84
6.2 Thermodynamic Properties 89
6.3 Conclusion 91

7 Defective Study of the Structures of Spinel Oxynitride Materials 94
7.1 Types of Defective Models 95
7.1.1 Constant Anion Model 96
7.1.2 Constant Cation Model 96
7.2 Structure of Spinel $M_{23}N_8O_{24}$ with M Vacancies 97
7.3 Elastic Constants of the Defective Oxynitride Spinel. 100
7.4 Band Structure and DOS of Defective Oxynitride Spinel 100
7.5 Conclusions 101

8 Conclusion **103**

8.1 Recommendation for Further Work 104

A Band Structures and Density of States of Defective Oxynitride Spinel **106**

B RDF Plots for the Ternary Oxynitride Spinel Materials **111**

References **111**

Conferences and Workshops **131**

List of Tables

1.1 Examples of some normal and inverse spinel. 10

4.1 Structural parameters of B_3NO_3, Al_3NO_3, Ga_3NO_3, In_3NO_3. 41

4.2 Fractional coordinates of the cubic spinel lattice for the LDA. The symmetry of this spinel is $P\bar{4}3m$ (No. 215) and it retains the four-fold symmetry in their site occupancy. 43

4.3 Fractional coordinates of the cubic spinel lattice for the GGA. The symmetry of this spinel is $P\bar{4}3m$ (No. 215) and it retains the four-fold symmetry in their site occupancy. 44

4.4 Cell structures of B_2O_3, Al_2O_3, Ga_2O_3, and In_2O_3. 45

4.5 Cell structures of BN, AlN, GaN and InN. 46

4.6 LDA and GGA (in bracket) calculated bulk modulus, pressure derivative, equilibrium volume and the zero-pressure energy of the spinel structures. The parameters were obtained from fitting to the Murnaghan, Birch and Universal equation of states. 48

4.7 LDA and GGA estimated values of Zero-pressure energy, equilibrium volume, pressure derivative and the bulk moduli of the ambient phases of the various materials. The GGA results are in brackets. 49

4.8 LDA and GGA estimated values of Zero-pressure energy, equilibrium volume, pressure derivative and the bulk moduli of the ambient phases of the various materials. The GGA results are in brackets. 50

4.9 Parametrization of the three strains used in calculating the three elastic constants of the cubic spinel structures. The energy expressions were obtained from Eqn. 4.8. Strains 1 is equivalent to simple hydrostatic pressure while strains 2 and 3 are strictly volume conserving to all orders in the strain parameter δ. 52

4.10 Calculated elastic constants and effective (Voigt) isotropic elastic modulii for Spinel Oxynitrides. Experimental values for diamond are B=442-433, G=524-544, E=1142-1164, ν=0.1. For spinel Si_3N_4 B=308 and G=258. All modulii are in GPa. A low (high) value of B/G may be indicative of the material to be brittle (ductile). The smaller value of ν may indicate the resistance of the material to shear. 53

4.11 Calculated band gaps of the spinels and their respective cubic binary nitrides. 56

4.12 ΔE_{stab} values for LDA and GGA (in brackets). *denotes the lowest value of ΔE_{stab} for the phases indicated. The values in column 3 and 4 in each section of the table shows the ΔE_{stab} of the spinels calculated from the total energies of the spinel (column 1), the oxide phases (column 2) and the nitride phases (row 1) respectively using Eqn. 4.15. 66

5.1 Parameters set (1) for the Tersoff potential, for atoms of spinel oxynitride M_3NO_3 where M = B, Al, Ga and In respectively. 83

6.1 Calculated equilibrium properties, elastic constants and effective (Voigt) isotropic elastic modulii for Spinel Oxynitrides compared with the results from *ab*-initio calculations. The calculated properties are from parameter set (1) using the Gulp code and B^{eos} from DL_POLY_3. All modulii are in GPa. 85

6.2 Tersoff potential parameters for BN, AlN, GaN and InN. 86

6.3 The adjusted Parameters (parameter set (2)) for the Tersoff potential, for atoms of spinel oxynitride M_3NO_3, where M = B, Al, Ga and In respectively. 87

6.4 The calculated and experimental elastic constants, equilibrium lattice constants and bulk modulus for the cubic structures BN, AlN, GaN and InN. These properties are calculated from parameter set (2) using the Gulp code. 88

6.5 Calculated equilibrium properties, elastic constants and effective (Voigt) isotropic elastic modulii for the modified Tersoff potentials of Spinel Oxynitrides compared with the results from *ab*-initio calculations. These properties are calculated from parameter set (2) using the Gulp code and B^{eos} from DL_POLY_3. All modulii are in GPa. 89

6.6 Calculated values for the Debye temperature, thermal expansion coefficients and specific heat of some cubic nitrides and the spinel oxynitride compounds. 93

7.1 Theoretical LDA and GGA (in parentheses) results for $M_{23}N_8O_{24}$. This results are compared with the available theoretical and experimental values of $M_{24}N_8O_{24}$. 98

7.2 Calculated LDA elastic constants and effective (Voigt) isotropic elastic modulii for defective oxynitride spinel. The values of the tetrahedral and octahedral vacancy sites have been compared with the bulk oxynitride spinel systems. 101

7.3 Calculated band gaps of the oxynitride spinels and their vacancy sites related structures. 101

List of Figures

1.1 Overview over various methods and models for solving physical and chemical problems. 2

1.2 Schematic of the Knoop indenter. The Knoop hardness is defined as $H_k = P/CL^2$ where P is the load, L is the length of indentation and C is a defined constant. 4

1.3 Knoop hardness as a function of bulk modulus for representative materials. 5

1.4 Two close-packed layers to show the two kinds of interstitial sites between the close-packed structure of the Oxygen ions in the spinel structures. . . . 7

1.5 The unit cell of an ideal spinel structure. 9

3.1 A schematic illustration of all-electron (dashed lines) and pseudo- (solid lines) potentials and their corresponding wave functions. The radius at which all-electron and pseudopotential values match is $\mathbf{r}_c$. 37

4.1 The cubic unit cell of the M_3NO_3 oxynitride spinel structure. The N atoms are at a tetrahedral position inside the cubic unit cell. 42

4.2 Trend in the LDA equation of state derived bulk modulus of spinels and cubic binary nitrides. 50

4.3 Calculated LDA energy band structure and density of states of B_3NO_3. The Fermi energy level is at zero energy. 57

4.4 Calculated LDA energy band structure and density of states of Al_3NO_3. The Fermi energy level is at zero energy. 58

4.5 Calculated LDA energy band structure and density of states of Ga_3NO_3. The Fermi energy level is at zero energy. 59

4.6 Calculated LDA energy band structure and density of states of In_3NO_3. The Fermi energy level is at zero energy. 60

4.7 Trends relating the band gaps with the lattice constants computed from the LDA results. 61

4.8 Calculated charge density distribution of B_3NO_3 and Al_3NO_3 in the (001) plane. The charge density is calculated from the LDA results. High charge density is colored red. 63

4.9 Calculated charge density distribution of Ga_3NO_3 and In_3NO_3 in the (001) plane. The charge density is calculated from the LDA results. High charge density is colored red. 64

4.10 Relative stability of M_3NO_3 spinel as compared with lowest energy ambient phases of M_2O_3 and MN structures as indicated in Table (4.12). 67

5.1 The key stages in MD simulation in the form of a flow chart. 71

6.1 The lattice parameter as a function of temperature for B_3NO_3, Al_3NO_3, Ga_3NO_3 and In_3NO_3. 92

7.1 The unit cell structure of the defective oxynitride spinel structure showing the octahedral (top) and tetrahedral (bottom) configurations. The non bonded atom shows a vacancy site. 99

A.1 Band structure and DOS of Oh and Td vacancy sites for B_3NO_3. The Fermi energy level is at zero energy. 107

A.2 Band structure and DOS of Oh and Td vacancy sites for Al_3NO_3. The Fermi energy level is at zero energy. 108

A.3 Band structure and DOS of Oh and Td vacancy sites for Ga_3NO_3. The Fermi energy level is at zero energy. 109

A.4 Band structure and DOS of Oh and Td vacancy sites for In_3NO_3. The Fermi energy level is at zero energy. 110

B.1 Pair distribution function for B_3NO_3 at 0, 500, 1000 and 2500 K. 112

B.2 Pair distribution function for Al_3NO_3 at 0, 500, 1000 and 2500 K. 113

B.3 Pair distribution function for Ga_3NO_3 at 0, 500, 1000 and 2500 K. 114

B.4 Pair distribution function for In_3NO_3 at 0, 500, 1000 and 2500 K. 115

Chapter 1

Introduction

The modeling of materials has become a very useful tool to make reliable predictions of the electronic, structural and thermodynamic properties of (novel) hard materials. Several approaches are used in the computational modeling of materials (see Fig. 1.1). They are classified as being either *Ab*-initio or semi-empirical methods. *Ab*-initio methods do not depend upon any external parameters except the atomic numbers of the constituent atoms to be modeled and are not preconditioned by any experimental findings. Calculations based on this method have considerably advanced with the development of fast computers. A powerful scheme for such calculations is the density functional formalism that describes the quantum mechanical effects of exchange and correlation and the pseudopotential approximation. Semi-empirical methods on the other hand are applicable to those systems where a significant knowledge exists about the system under specific conditions of temperature and pressure or can be modeled under other conditions. Semi-empirical modeling is an interpolation from one system to the other, probably unknown or experimentally inaccessible, conditions. This approach assumes that interactions in the solid can be represented by two or three-body potentials or force-fields between atoms. The interaction is usually obtained by fitting models to results on molecular systems [1].

A short overview of the typical computational methods used in these calculations is shown

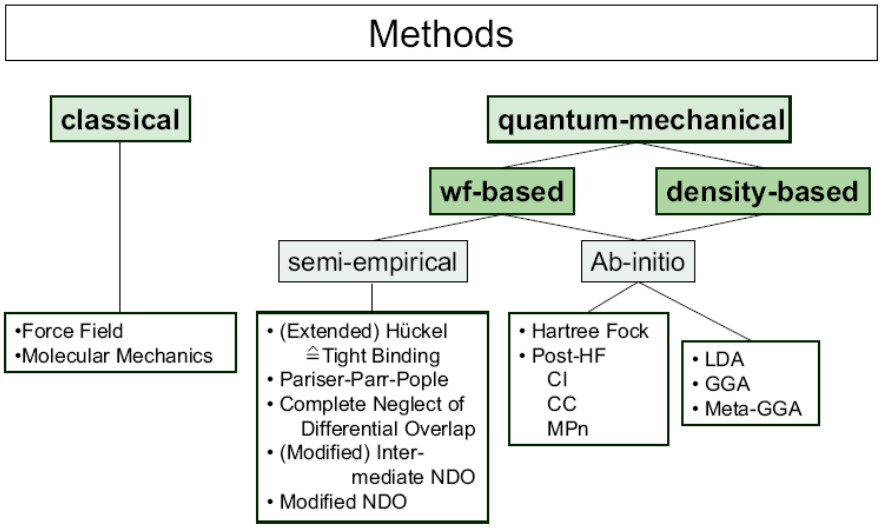


Figure 1.1: Overview over various methods and models for solving physical and chemical problems [2]. wf stands for wave function.

in Fig. 1.1.

Computational modeling of materials has been a driving issue in the research of new materials and provides valuable insight into potentially important new materials and likewise materials that may not be important. Hard materials, especially, are of great interest due to their superior mechanical and chemical properties such as higher compressional strength, thermal conductivity, spectral transmittances, hole mobilities, refractive index, and chemical stability [3]. They possess a strong covalent bonded crystal structure often of high symmetry. The properties of hard materials depend on many parameters like pressure, temperature, porosity, impurities, dislocations, and hardness is often correlated to various other physical properties like ionicity, melting point, band gap, elastic modulus and cohesive energy [4, 5]. Hard materials have been used as gem stones, heat sinks, radiation windows, speaker tweeters, mechanical bearings, surgical knives, container coatings, and, potentially novel semiconductors. One of the major industrial applications of hard materials is as superabrasives [5].

There has been much experimental and theoretical effort in recent years devoted to develop a new class of hard materials with properties that can compete with and even have

properties superior to diamond or cubic boron nitride (*c*-BN) - which are the two well-known super-hard materials. Spinel structures have been found to be potentially important hard materials [6, 7]. The high hardness and high density that characterized a spinel is as a result of the tetrahedral bonded nature of the coordinated cations which is similar to that of diamond the hardest known bulk material [8].

1.1 Defining and Measuring Hardness

The hardness of a material is decided by the process of how resistant the interatomic bonds in the material are against distortions needed to generate deformations and, in part, how defects such as dislocations can move in the system. It is usually measured by pressing a diamond tip into the surface of a sample with a known force and subsequently measuring the size of the indentation made in the surface. Hardness is then simply the force divided by the indent area and is expressed in GPa or Kg/mm^2. The smaller the indentation the harder the material. There are two major hardness measuring techniques of hardness; a Vickers test uses a symmetric diamond tip and a knoop test uses an asymmetric diamond tip [5, 9, 10, 11]. The Knoop indentation test shown in Fig. 1.2 is a widely used standard. However, hardness is too complex to be described by *ab*-intio methods (first principles). Over the last two decades, the search for hard materials has had to be simplified to a search for materials with bulk modulus or shear modulus, which can be evaluated directly by first principles. While there is no one-to-one correspondence between hardness and bulk modulus or shear modulus, there is a rather rough trend that the larger the bulk or shear modulus, the higher the hardness. Diamond has the largest known bulk and shear modulus and the largest hardness value. Daryl Clerc [12], in his work has proposed the electronic factors that determine high bulk moduli in diamond-like materials. For cubic phases (like the cubic spinel structure), hardness is known to scale well with the bulk and shear modulus. Therefore by predicting moduli of novel materials, a hard material may be identified. Fig.

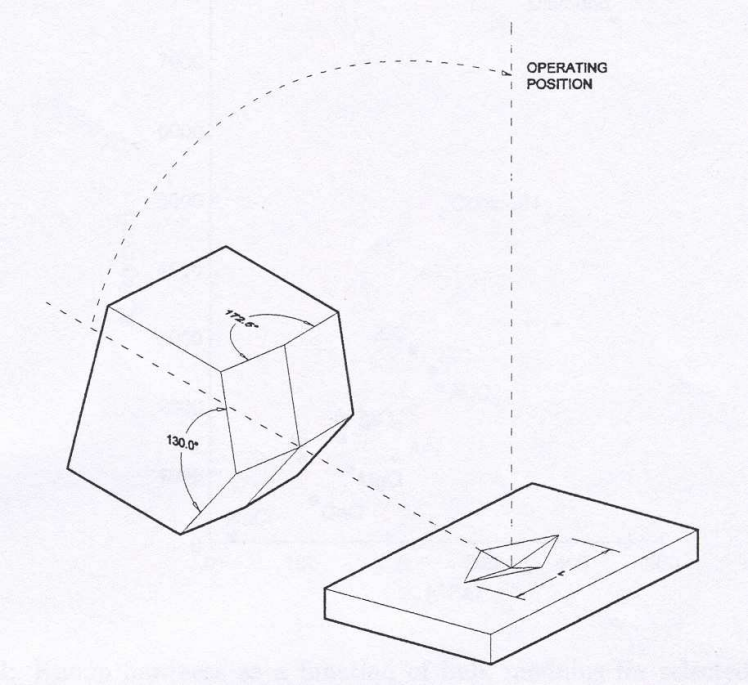


Figure 1.2: Schematic of the Knoop indenter. The Knoop hardness is defined as $H_k = P/CL^2$ where P is the load, L is the length of indentation and C is a defined constant [15].

1.3 compares the knoop indentation hardness with the bulk moduli of selected materials. Materials like metals, however, do not follow this trend. This is as a result of their low shear strength [13, 14].

1.2 The Spinel Structure

The work presented in this study deals with spinel oxynitride based material. The name "spinel" is derived from the Greek word for spark, in reference to the red color of spinels. Excerpt from the Africa Johns collector Beads on spinel [16] states that

> "Many large red stones formerly thought to be rubies or red diamonds recently have been correctly identified as spinel. They are very brilliant and come in many colors including red, pink, blue, and green. They are said to relieve stress and depression and assist with mental rejuvenation. The energy of spinel is the

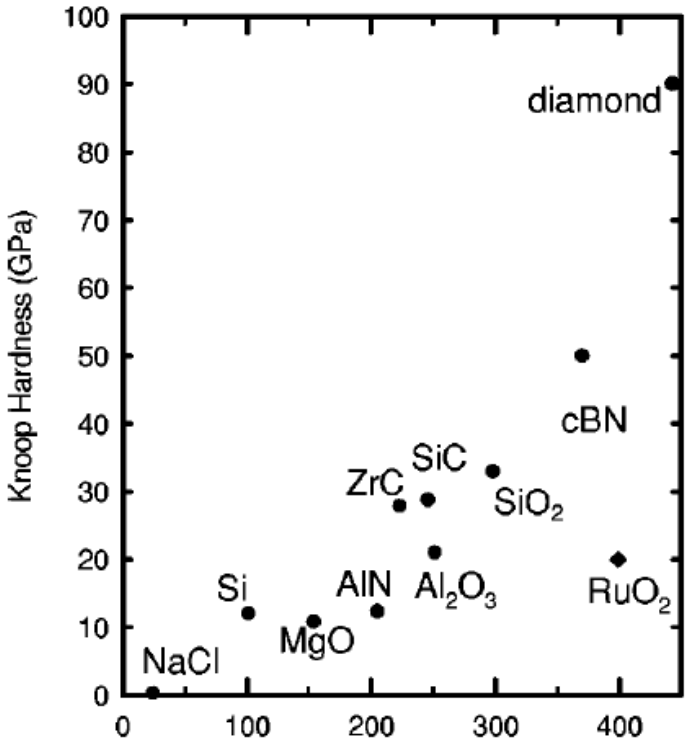


Figure 1.3: Knoop hardness as a function of bulk modulus for representative materials [14].

> energy of beauty. It is known as a "stone of immortality" bringing freshness to all endeavors and initiating rejuvenation to that which is beginning to degrade".

Spinel is one of the known gemstones in an oxide class of materials. It is found as a metamorphic mineral with hardness 8, specific gravity of 3.5-4.1 and it possesses an intermediate to high refractive index, shows a good dispersion, and is available in a wide variety of colors. Spinel structure is in class of mineral spinels known as $MgAl_2O_4$ which is the sole gemstone representative of the spinel group. Spinels exhibit remarkable electrical, magnetic, and other physical characteristics.

The important members of the spinel group include:

- Spinel (Magnesium Aluminium Oxide)- $MgAl_2O_4$, after which this class of mineral is named
- Gahnite (Zinc Aluminium Oxide)- $ZnAl_2O_4$

- Franklinite (Zinc Iron Manganese Oxide)- $ZnFeMnO_4$
- Magnesiochromite (Magnesium Chromium Oxide)- $MgCr_2O_4$
- Magnetite (Iron Oxide)- Fe_3O_4
- Chromite (Iron Chromium Oxide)- $FeCr_2O_4$
- Minium (Lead Oxide)- Pb_3O_4

Magnesium Aluminium Oxide ($MgAl_2O_4$) Spinel with lattice parameter, $a = 0.80898(9)$ nm is a ceramic oxide that is characterized with good optical and insulating features. It has demonstrated strong radiation resistance to amorphisation and to the formulation of defect clusters and dislocation loops due to the large number of cation sites [17, 18].

In general the spinel structure refers to a class of oxides with chemical formula AB_2O_4, where A and B are either divalent (+2) and trivalent (+3) or tetravalent (+4) and divalent cations. This structure has a cubic closed packing (fcc) arrangement of oxide ions with a large unit cell containing eight formula units. The unit cell of a spinel ($A_8B_{16}O_{32}$) contains 56 atoms (i.e 8 A, 16 B, and 32 oxygen atoms). Spinel belongs to the space group of Fd3m, O_h^7 (No. 227) in which the following positions are occupied [19]:

$8a : 000, \frac{1}{4}\frac{1}{4}\frac{1}{4}$. (+ f.c.c);

$16d : \frac{5}{8}\frac{5}{8}\frac{5}{8}, \frac{5}{8}\frac{7}{8}\frac{7}{8}, \frac{7}{8}\frac{5}{8}\frac{7}{8}, \frac{7}{8}\frac{7}{8}\frac{5}{8}$. (+ f.c.c);

$32e : uuu, u\bar{u}\bar{u}, \bar{u}u\bar{u}, \bar{u}\bar{u}u, \frac{1}{4} - u\frac{1}{4} - u\frac{1}{4} - u,$

$\frac{1}{4} - u\frac{1}{4} + u\frac{1}{4} + u, \frac{1}{4} + u\frac{1}{4} - u\frac{1}{4} + u, \frac{1}{4} + u\frac{1}{4} + u\frac{1}{4} - u.$ (+ f.c.c).

where u is an internal parameter for the anion and is often known as the oxygen parameter [20, 21]. The oxygen parameter, u, is the distance between the oxygen ion and the face of the cube edge along the cube diagonal of the spinel sub cell. Besides the spinel-type oxides, some halide, nitride and sulphide also crystallize in this structure (e.g Si_3N_4 and Co_3S_4). The cation to anion ratio distribution of spinel is 3:4 irrespective of there different phases such as binary (Fe_3O_4), ternary ($MgAl_2O_4$) and quaternary ($Si_{6-z}Al_zO_zN_{8-z}$) [22].

1.3 Cation Arrangement in Spinels

The cubic closed-packed array of anions holds two types of voids or interstices, namely, the tetrahedral and the octahedral interstices. Fig. 1.4 illustrates the two kinds of interstitial sites between the close-packed structure of the Oxygen ions in the spinel structures. The shaded layer of atoms lies below the layer with no shading. The interstices with square shape are the tetrahedra sites enclosed by four close-packed atoms forming a tetrahedron as shown in (b). The interstices with round shape are the octahedral sites coordinated by six close-packed atoms which form an octahedron as shown in (c).

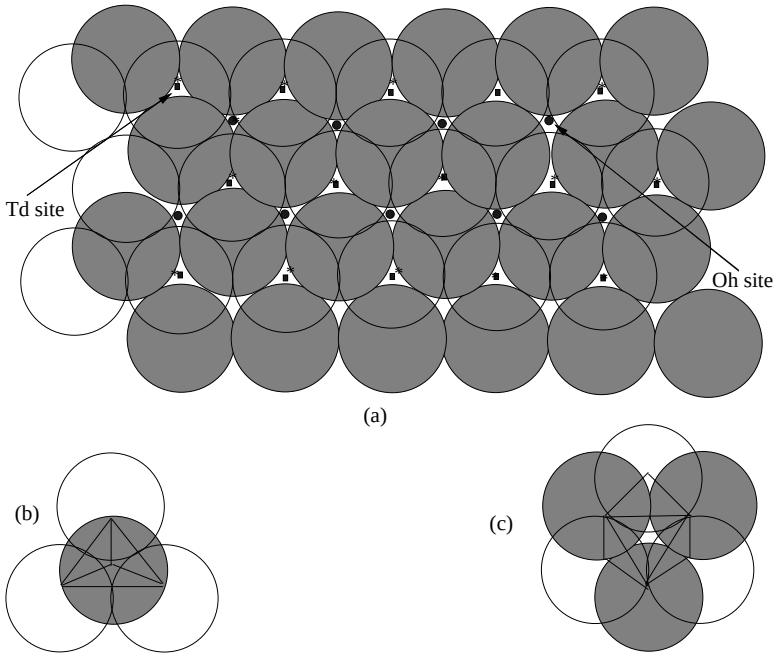


Figure 1.4: Two close-packed layers to show the two kinds of interstitial sites between the close-packed structure of the Oxygen ions in the spinel structures.

The tetrahedral is formed by four lattice atoms of the tetrahedron and is commonly denoted as the *A* site, whereas the octahedral is formed by six lattice atoms of the octahedron is commonly denoted as the *B* site. The relative ionicity (i.e. the ironic radius) and the size of the interstices determines how the cations occupy the site with the tetrahedral or octahedral symmetry [23, 24]. The Ionic distribution is determine by the Madelung potential

(constants) in which the various associated energy terms are written as a function of the ionic distribution. Verwey and *et al* [25] have used the expression in the following Eqn. 1.1 to calculate the Madelung Constants for the total Coulomb energy of the ionic crystal per "molecule" AB_2O_4:

$$V = -\frac{1}{2}(e^2/a)(pM_{tetr} + 2qM_{oct} + 8M_o) = -M_{e^2/a} \tag{1.1}$$

where ep and eq are the ionic charges at tetrahedral and octahedral interstices and M_{tetr}, M_{oct}, and M_o are the local Madelung constants determining the electronic potential at the tetrahedral and octahedral interstices and at the O^{2-} lattice points respectively.

In the unit cell of the spinel, there are a total of $\mathbf{64}$ tetrahedral interstices and $\mathbf{32}$ octahedral interstices between the anions; however, only $\mathbf{8}$ and $\mathbf{16}$ of the tetrahedral and octahedral sites are occupied by the cations respectively. In other words, $\frac{1}{8}$ of the *A* sites and $\frac{1}{2}$ of the *B* sites are occupied by the cations. The tetrahedrally coordinated cations form a diamond cubic sublattice with a repeat unit equal to the lattice parameter. This explains the relatively high hardness and high density that is typical of spinel [7]. Fig. 1.5 shows the unit cell of an ideal spinel structure. This figure shows that there are two types of cubic building units inside a big fcc O-ion lattice, filling all the $\mathbf{8}$ octants.

The position of the cations are fixed by the symmetry of the structure but the anion positions are variable and are specified by the oxygen parameter, u. For instance, when the *A* sites are too small for the cations, the oxygen ions move slightly to be accommodated them and also tend to shrink the size of the *B* site by the same amount as the *A* site expands. In all spinel-like structures the oxygen parameter, u, has a value in the neighborhood of 0.375. However, in actual spinel lattices this ideal pattern is slightly deformed, usually, corresponding to $u > 0.375$, in such a way that the oxygen tetrahedron in the *A* cubes is somewhat expanded and the oxygen octahedron on the *B* cubes is slightly contracted. Accordingly, in that case the octahedrons formed by the six oxide ions directly surrounding the positive ions in the *B* cubes deviate somewhat from the regular octahedrons [19, 23].

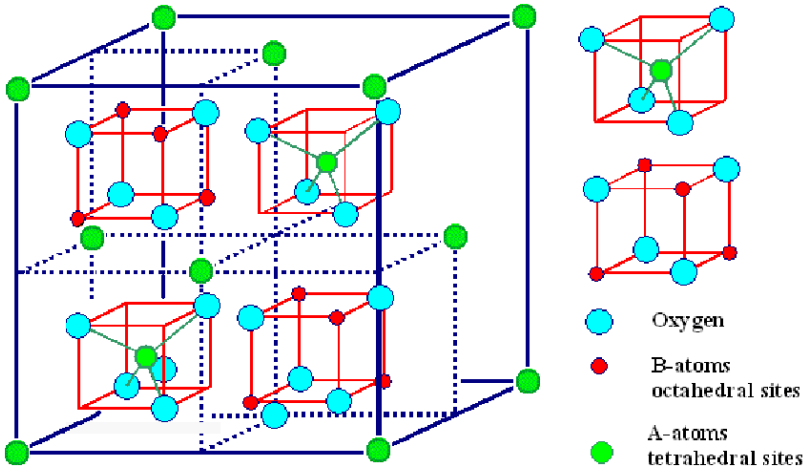


Figure 1.5: The unit cell of an ideal spinel structure [23].

1.4 Types of Spinel

There are two types of limiting configurations of cations in the spinel-structured compounds called normal (or direct) spinel and inverse (or indirect) spinel. The normal spinel, refers to a compound that is composed of divalent and trivalent cations, where the less abundant divalent cations occupy tetrahedral *A* sites and the more abundant trivalent cations occupy the octahedral *B* sites. However, the work done by Barth and Posenjak [26], who based their conclusions upon a detailed discussion of the intensities of X-ray diffraction patterns, pointed out a second possibility called the inverse spinel, $B(AB)\mathrm{O}_4$, which is compose of a tetravalent and a divalent cations, where half of the divalent cations occupy tetrahedral *A* sites and all the tetravalent cations and together with the other half of the divalent cations occupying the octahedral *B* sites [23, 27].

Besides these two arrangements there are also possibilities for some intermediate arrangements of the form $(A_{1-2\lambda}B_{2\lambda})(A_{2\lambda}B_{2-2\lambda})\mathrm{O}_4$ with an average distribution of all ions about the spinel cation positions. Spinels with these configurations are known as intermediate or random spinels. They are located somewhere between the normal and the inverse arrangements. The variable λ is the so-called inversion parameter, which specifies the fraction of

Table 1.1: Examples of some normal and inverse spinel [23].

Type	**Structure**	**Examples**
Normal	$(A^{+2})(B_2^{+3})\mathrm{O}_4$	$ZnFe_2O_4$, $ZnCrFeO_4$, $MgCr_2O_4$, $MnAl_2O_4$
Inverse	$(B^{+3})(A^{+2}B^{+3})\mathrm{O}_4$	$MgFe_2O_4$, $NiFe_2O_4$, $CoFe_2O_4$, Fe_3O_4
Random	$(A^{+2}{}_{1-2\lambda}\ B_{2\lambda}{}^{+3})(A_{2\lambda}{}^{+2}B^{+3}{}_{2-2\lambda})\ \mathrm{O}_4$	$MgCrFeO_4$

A sites occupied by the majority of ions. It ranges from 0 for the normal spinel to 0.5 for the inverse spinel [28]. Table 1.1 illustrates some of the examples of normal, inverse and the intermediate spinel.

1.5 Thesis Scope and Outline

The aim of this work is to examine a spinel structure of compounds formed from group-III oxides and nitrides leading to an oxynitride spinel structure with a chemical formula M_3NO_3. The theoretical properties and predictions are investigated and are performed using *ab*-initio or first principles electronic structure methods based on density functional theory (DFT) and molecular dynamics simulation based on the Tersoff empirical potential. Essentially the chemical equation that we shall consider to represent formation of the oxynitride spinel structure is:

$$M_2O_3 + MN \longrightarrow M_3NO_3$$

where, in the present work, M can represent Boron, Aluminium, Gallium, and Indium.

The scope of this thesis is divided in threefold: the first part of examines the properties such as the electronic structure, equation of state, elastic constants and relative stabilities of possible synthesis phases of the bulk oxynitride spinel. In the second part, we have performed a molecular dynamics simulation using an empirical potential to study and predict

the thermodynamic properties of these systems at varying temperatures. And lastly, the third part is devoted to the study of defect on the oxynitride spinel. Using the Constant Anion Model, with vacancies at the *M* sites, we investigated the effects this could have on the bulk oxynitride spinel.

The thesis is organized as follows. We start by reviewing the constituent parent phases of the material that are the essential building blocks of the oxynitride spinel materials, in Chapter 2. Chapter 3 contain the description of the electronic structure calculation of the density function theory (DFT). DFT allows us to tackle the many body problem and obtain all the ground state properties of the electronic system. We outline in particular the local density approximation and the generalized gradient approximation for exchange-correlation functionals and the treatment of the plane wave basis set and the pseudopotential approximation. In Chapter 4, we present an analysis of the optimized geometries, crystal structure the elastic bulk properties, the electronic structures as well as the relative stabilities of the oxynitride spinel structures. The basic theory of molecular dynamics simulation technique is described in chapter 5. We have proposed a series of Tersoff potential for various oxynitride ternary systems. In what follows, the structural and thermodynamics properties of the MD simulations are discussed in chapter 6. Chapter 7 deals with the defective study of oxynitride spinel structures. Here we also show the vacancy sites (octahedral or tetrahedral) where the the most stable (or lowest energy) structure of these materials are found. The concluding discussions, and the recommendations for further work, are presented in Chapter 8.

Chapter 2

A Review of Group-III Oxides and Nitrides

2.1 Introduction

The spinel oxynitride M_3NO_3 structure could be formed through an alloyed mixture of MN and M_2O_3. These systems have been considered as the essential building blocks of the spinel in this study. They exist in two or more crystallographical phases, which can be stable or metastable states polytypes. The phases of the group-III oxides and nitrides are described in the following sections. These materials are of high technological importance with unique properties. They have wide range of applications from material hardness to optoelectronic devices.

Optimized structural parameters, the zero-pressure energy, equilibrium volume and the bulk moduli of the ambient phases of the group-III oxide and nitride materials are obtained using *ab*-initio LDA and GGA calculations. Both the LDA and GGA estimated values are in good agreement with the experimental results where possible and this serves as a benchmark for the investigation of the spinel oxynitride systems.

2.2 Forms of Group-III Oxides

The suggested oxides of group-III elements (atoms) to be considered are Boron oxide (B_2O_3), Aluminum oxide (Al_2O_3), Gallium oxide (Ga_2O_3) and Indium oxide (In_2O_3).

2.2.1 Boron Oxide (B_2O_3)

Boron oxide, B_2O_3, is an important industrial mineral used as a glass-forming material. It has excellent properties like hardness, insulation, linear and nonlinear optical behavior all of which have made them useful for various electronic and optoelectronic devices. Boron oxide can be produced by direct reaction of boron and oxygen under pressure. It has the advantage of very low heat expansion, high refractive index and high ion conductivity. Because of these characteristics, boron oxide is used widely in glass forming materials (especially in various fast-ion conducting glasses) and a typical example of a covalently bonded network glass. When doped on ceramic materials, it enhances conductivity and structural stability [29, 30]. B_2O_3 is also one of the additives used to modify textural and acid based properties of metal oxides such as Al_2O_3, Ti_2O_3 and MgO [31].

Despite its great importance as a strong network glass former, the structure of B_2O_3 has been a subject of debate for many years now, particularly concerning the prevalence and structural role of boroxol (B_3O_6) groups. According to the first structural model of vitreous B_2O_3, proposed by Zachariasen [32], the glass consisted of a three dimensionally random network of BO_3 triangles. However, this model was challenged [33] and as a result of many spectroscopic investigations such as neutron and X-ray diffraction, Raman spectroscopy, as well as nuclear magnetic resonance (NMR) and nuclear quadrupole resonance (NQR) spectroscopy [34, 35], it has been widely viewed and accepted that the molecular building block of vitreous B_2O_3 is the planar BO_3 triangles (groups) in which the boron atoms are threefold coordinated by oxygen atoms and centered at the basic unit of BO_3 triangles. The three BO_3 triangles can combine to form a boroxol ring (B_3O_6) [34, 35, 36, 37, 38].

A model of vitreous B_2O_3 with boron atoms residing in the boroxol rings has two crystalline forms in which the boron atoms are trigonally or tetrahedrally coordinated to oxygen atoms. They are known as B_2O_3-I and B_2O_3-II. B_2O_3-I is known as the low-pressure structure of B_2O_3, obtained at a pressure of 2 GPa with a hexagonal unit cell and has boron coordinated by three oxygen atoms. B_2O_3-I crystallizes in space group $P3_1$ with $a = 4.336\mathring{A}, c = 8.340\mathring{A}$ as reported by Gurr et al [39]. B_2O_3-II is the high-pressure phase structure of B_2O_3 obtained at a pressure of 6.5 GPa and temperature of $1100\ ^oC$. The structure of B_2O_3-II is orthorhombic with $a = 4.613\mathring{A}, b = 7.803\mathring{A}, c = 4.129\mathring{A}$, and space group $Ccm2$, built up by two sets of tetrahedral with shared corners as described by Prewitt and Shannon [40]. It could be observed that under pressure, crystal B_2O_3 undergoes a structural transformation that increases the boron coordination from BO_3 triangular unit into the BO_4 tetrahedral unit [41].

2.2.2 Aluminum Oxide (Al_2O_3)

Aluminum oxide or alumina is a technological important material that is widely used in numerous applications such as a structural ceramic and optical materials. As a structural ceramic materials it is extensively used as a high temperature, corrosion resistant refractory material on high-speed machine tools for milling and cutting of cast iron and low carbon steel mainly due to its high hardness, chemical durability, mechanical strength, high surface area and oxidation resistant properties. It can also be used as a thin-film devices which is of interest in microelectronics industry as an insulating material. The later applications make use of the electronic structure and bonding present in Al_2O_3 [42, 43, 44, 45].

Alumina (Al_2O_3) is produced by the Bayer process from the calcination of aluminium hydroxides ($Al(OH_3)$, gibbsite) produced by precipitation from sodium aluminate liquor at a certain temperature [46, 47]. Extensive research has been conducted to understand and characterize the diverse phases in Al_2O_3 and to establish the thermodynamics and kinetics related to the transformation between the phases. It is widely believed that alumina exists

in several transient, metastable structural polymorphs such as γ-, η-, δ-, θ-, κ-, and χ-aluminas, as well as the stable α-Al_2O_3. The mestable phases seem to be stabilized by the large surface area that is produced with several preparation techniques. When the samples are heated they recrystallized and transforms into the α structure [45, 48].

The stable α-phase (space group $R\bar{3}c$) which is commonly known as corundum has a hexagonal close packed (hcp) rhombohedral crystal structure with stacking sequence ABAB and lattice parameter $a_o = 4.76\mathring{A}$ and $c_o = 12.99\mathring{A}$. The cation coordinations are such that the Al atom is surrounded by six atoms of two different near-neighbor (NN) distances, and each O atom has four NN Al atoms. On the other hand, the metastable polymorhps such as $\gamma, \eta, \delta, \theta$ are based on a face centered cubic packing of oxygen anions with the aluminium cations being distributed between octahedral and tetrahedral interstices whereas κ and χ are the mestable form of the hexagonal close packed (hcp) array of oxygen anions [44, 48, 49, 50]. However, among the transition aluminas, θ-Al_2O_3 is the most dominant phase [51] (to be considered in this work) since it has a well defined structure in terms of site occupations (in contrast to γ-alumina which is described as a defect spinel structure) and it's often used as a reference structure to those polymorphs [48]. The crystal structure of θ-Al_2O_3 is monoclinic with a space group of $C2/m$ and lattice parameter $a_o = 11.854\mathring{A}$, $b_o = 2.904\mathring{A}$ and $c_o = 5.622\mathring{A}$. The unit cell contains four Al_2O_3 molecules [52].

2.2.3 Gallium Oxide (Ga_2O_3)

Gallium oxide, Ga_2O_3 is the single stable oxidation state of gallium under normal conditions and it is known to be a thermally and chemically stable material which is insulating at room temperature but semiconducting at higher temperatures [53]. Gallium oxide, is a wide band gap material and is of interest due to its interesting unique properties such as conduction, and luminescence. These properties make it a host for gas sensors, and optoelectronic device applications [54, 55]. There have been recent reports of the material being found

as nanotubes [56] and as a relevant catalytic material for light alkane dehydrogenation and aromatization (Cyclar process), and hydrogenation isomerization [57].

The binary oxides of Ga are similar to those of Al but have been studied in less detail. Gallium oxides are found in five different crystalline structures, that is α-, β-, γ-, δ-, and ε-phases [58]. Among these structures, α-Ga_2O_3 is rhombohedral, β-Ga_2O_3 is monoclinic, γ-Ga_2O_3 is cubic and δ-Ga_2O_3 have a bcc structure. ε-Ga_2O_3 has been reported to be in a mestable form. These different structures significantly influence the surface properties of Ga_2O_3, accounting for the variation in catalytic activity among these phases [59, 60]. α, β are the two major forms of Ga_2O_3 and are classified under high and low temperature forms of gallium oxide.

High temperature β-Ga_2O_3 is the most stable form of the metal oxide. The symmetry is $C2/m$ with lattice parameters evaluated as $a = 12.239\mathring{A}$, $b = 3.041\mathring{A}$, and $c = 5.813\mathring{A}$. It contains four molecular units of Ga_2O_3 per unit cell and in which half of the cation sites are octahedrally coordinated and the other half are tetrahedrally coordinated. β-Ga_2O_3 belongs to the group of transparent conductive oxides (TCOs) and it has been suggested that under oxygen-rich condition β-Ga_2O_3 may undergo phase transition although details of the transformed phase are not well understood at this time [61, 62, 63]. α-Ga_2O_3 is the low temperature phase of gallium oxide. The phase transition temperature from α-Ga_2O_3 to β-Ga_2O_3 is about 600 ^{o}C. α-Ga_2O_3 thus has the strong advantage of low synthesis temperature as compared to that of β-Ga_2O_3. The α-Ga_2O_3 is isostructural with α-corundum and the gallium ions are octahedrally coordinated with closely packed array of oxygen ions. The unit cell lattice parameters of α-Ga_2O_3 defined within the space group of $R\bar{3}c$ are $a = 4.980\mathring{A}$, and $c = 13.431\mathring{A}$ [61, 63, 64, 65].

2.2.4 Indium Oxide (In_2O_3)

Indium Oxide (In_2O_3) has been widely used as a material for transparent electrodes in opto-electronic devices such as liquid crystal displays, window heaters, flat panel displays, solar

cells, as a barrier layer in tunnel junctions, as a sensing materials in gas sensors due to its good electrical conductivity and optical transparency. Currently, it has shown remarkable potential applications in the upcoming nano-electronic building blocks and nano-sensors as a result of their unique physical and chemical properties which depend on their mesostructures. Many fabrication techniques such as thermal decomposition of precursors, sol-gel method, chemical vapor decomposition, and dc magnetron sputtering have been successfully developed as a result of its wide applicabilities [66, 67, 68, 69].

In_2O_3 can exist in two different crystal phases namely: body-centered cubic (bcc-In_2O_3) and rhombohedral (rh-In_2O_3) and are characterized by space group symmetries $Ia3$ and $R\bar{3}c$ and which we refer to throughout this work as phases In_2O_3-I (for bcc-In_2O_3) and In_2O_3-II (for rh-In_2O_3) respectively. The physical and optical properties of In_2O_3-I are well known and have been studied both theoretical and experimentally whereas for In_2O_3-II, no information are available and are rarely studied [69, 70] except for the work done by Shannon [71] on In_2O_3-II polytype.

In_2O_3-I is the low-pressure phase of indium oxide. It crystallizes in the cubic bixbyite structure (C-type, rare earth sesquioxide structure) with lattice constant of $10.118\mathring{A}$. It is composed of eight fluorite-type unit cells with systematic anion vacancies. The unit cell consists of two types of In (which are surrounded by oxygen in the octahedral and trigonal prismatic coordinations alternatively) and one type of O atoms located at Wyckoff positions $8b$, $24d$, and $48e$, respectively. All In atoms are coordinated by six oxygen atoms forming a distorted octahedron. The bond length of In-O is ranged from $2.12\mathring{A}$ to $2.21\mathring{A}$. The neighboring octahedral are shared with their corners and edges [70, 72]. In_2O_3-II, on the other hand, is known as the high-pressure metastable phase with a rhombohedral corundum structure. Shannnon, in his work obtained In_2O_3-II polytype by a high pressure synthesis using indium sesquioxide as a source material [71] and it has been reported that the stability and conductivity of this phase should be favorable to that of cubic phase [66]. The lattice constants are $a = 5.478\mathring{A}$ and $c = 14.51\mathring{A}$ with two fluorite-type unit cells. It consists of

one type of In (surrounded by oxygen in trigonal biprism coordination) and one type of O atoms occupying $12c$ and $18e$ Wyckoff positions, respectively [69, 70].

2.3 Forms of Group-III Nitrides

The group-III nitrides namely: BN, AlN, GaN, and InN, are currently being investigated for unique potential. They have uses in optoelectronic devices operating in visible or ultraviolet spectral range as well as in high-temperature, high-power, and high-frequency microelectronics devices and are materials that are characterized by large band gaps and strong (mixed ionic and covalent) bonding. Furthermore, the properties of their different phases, such as hardness, high melting point, high thermal conductivity, large bulk moduli also makes them useful for protective coatings. These outstanding properties are mainly related to the specific role of the nitrogen atoms. The smallness of the nitrogen atoms gives rise to the formation of short bonds, which lead to significantly smaller lattice constants [73, 74, 75].

2.3.1 Boron nitride (BN)

Boron nitride exists in different polytypes, the hexagonal, rhombohedral, cubic, turbostratic, simple cubic, and wurzite phases. The most common crystal phases among them are the less dense hexagonal boron nitride, (*h*-BN) and bulk cubic boron nitride (*c*-BN) structures. The hexagonal phase is a layered (with $AaAa$ stacking sequence), sp^2-bonded material, that is isostructural to graphite. It is a ceramic material that can be obtained by more gently chemical vapor deposition (CVD) methods and experimentally stable at high temperatures of about 900-1500 ^{o}C. Hexagonal boron nitride finds applications as a high-temperature lubricant, as a heat sink or substrate in electronic devices, and in production of ceramic parts and coatings. With a band gap of 5.97 eV, the electronic properties suggest that it may also be useful in the production of a compact ultraviolet laser device that could be

used in optical storage, photocatalysis, sterilization, ophthalmic surgery, and nanosurgery applications [76, 77, 78].

The cubic phase (c-BN) has a zinc-blende lattice structure with cubic symmetry and sp^3-hybridized B-N bonds [79]. Recent experimental results have pointed out that c-BN is the thermodynamically stable phase under ambient conditions [80, 81]. Boron nitride in this form has a variety of interesting properties, including being ultra-hard, as well as having high melting point and high thermal conductivity as well as low friction coefficient. Due to the isoelectronic nature of BN to carbon, *c*-BN is isostructural to diamond and it is the second hardest material known after diamond. For industrial tools used in cutting and shaping iron- or nickel-containing materials, c-BN, is superior to diamond, as the c-BN blades do not deteriorate as a result of reactions with this sort of material. And as a wide gap semiconductor, it has the ability to produce both *n*-type and *p*-tpye conductivities when doped appropriately [79, 82, 83].

2.3.2 Aluminum Nitride (AlN)

Aluminum nitride, AlN, which is generally reported to be nonpolymorphous, crystallizes at standard condition in the wurzite structure [74]. However, several works report the occurrence of zinc-blende structure of AlN [84, 85]. AlN is a good candidate for electronic applications due to its high thermal conductivity, high hardness and elastic stiffness, and high temperature stability (melting temperatures ~ 3000 ^{o}C). It is considered a promising material for high power optical and surface acoustic wave device applications. The binary nitride of Al have an ultrahigh band gap and forms a continuous alloy system with GaN, thereby becoming more important for group-III nitride device development [86, 87].

Wurzite AlN is the only significant III-V based Al semiconductor compound with a direct band energy gap, and it in fact has the largest gap of any material still commonly considered to be a semiconductor. The Zinc-blende (cubic) structure of AlN has been theoretically reported to be mestable and only the calculated lattice parameter ($a = 4.37\mathring{A}$)

is available. Because of the reactivity of AlN, high purity source material and an oxygen-free environment are required to grow AlN crystals of good quality. Therefore, AlN is not a particular easy material to study experimentally and most researchers in the field have concentrated on GaN [74, 85, 88].

2.3.3 Gallium Nitride (GaN)

The nitride of Ga (GaN) is a wide gap semiconductor. Unlike all of the non-nitride wide gap group-III-V semiconductors, GaN has a direct energy gap that makes it suitable for blue lasers and LEDS with important applications in UV-visible optoelectronics and in high-frequency, high-temperature or high-power electronics. Its sensitive to ionizing radiation is low, making it a suitable material for solar cells arrays for satellites [88]. GaN layers are commonly grown on sapphire substrates, where the mismatch in lattice constants and thermal expansion coefficients between the substrates and the GaN layers produces a large density of dislocation. Fabrication of GaN nanowires provides interesting opportunity for studying low dimensional strain free structures [89]. GaN can exist in three well-defined crystalline forms. These are the most common wurzite (also known as hexagonal), and the less common zinc-blende (sometimes refered to as cubic). Under very high pressure, GaN and other nitrides experience a phase transition to the rock-salt structures. Of these structural forms, several fundamental calculations [90, 91, 92] have indicated that the lowest energy phase is the wurzite structure with the cubic phase only marginally higher in energy. To the contrary the rock-salt structures is far higher in energy. For this reason the rock-salt form of GaN has not been considered in this work.

2.3.4 Indium Nitride (InN)

Among the group-III nitrides (BN, AlN, GaN and InN), InN is not very well investigated. High quality bulk InN samples are difficult to grow due to its low thermal stability; reliable experimental information about the properties is therefore scarce [88, 93]. Indium nitride

is a small band gap semiconductor material which has potential application in solar cells and high speed electronics. The use of InN and its alloys with GaN and AlN makes it possible to extend the emission of nitride-based LEDs from ultraviolet to near infrared region. And as such, the InN ternary alloy with GaN namely InGaN, has found application in a variety of heterostructure based optoelectronic devices, such as LEDs and lasers. The InGaN quantum wells are indispensable for light emitting devices because incorporation of small concentrations of In in the active GaN layer increases luminescence efficiency considerably [94]. InN has been predicted to have lowest effective mass for electrons in all the group-III nitride semiconductors, which leads to high mobility ($> 2000\text{cm}^2\text{V}^{-1}\text{S}^{-1}$) and high saturation velocity [95].

Epitaxially grown InN has been reported to have a cubic (zinc-blende) and wurzite (hexagonal) structural symmetry depending on the substrate type and orientation [96]. The techniques commonly used to investigate the symmetry of InN thin films are x-ray diffraction (XRD) and near-edge x-ray absorption fine structure spectroscopy (NEXAFS) with polarized x rays. The development of epitaxial techniques for the growth of InN have demonstrated that the band gap of InN is between 0.7 and 0.9 eV, instead of the previously accepted value of 1.9 eV. The advantage of the cubic structure as it relates to improved device performance could be the isotropic nature of the properties and the existence of common cleavage planes with Si or GaAs substrates. In addition, in the wurzite structures, the piezoelectric fields across the layers localize the carriers leading to an asymmetric well at the interfaces [96, 97].

Chapter 3

Electronic Structure Methods

3.1 Introduction

The object of electronic structure calculations is to obtain the electronic charge density (the real space distribution of electron around the atom). The electronic charge density plays an important role in the theory and understanding of the system of electrons and nuclei which are the fundamental properties of matter. Therefore, if the charge density can be calculated, one can correctly predict the properties such as equilibrium lattice constants, elastic and shear constants, bulk modulus as well as hardness of the material.

Electronic structure methods are termed *ab*-initio or first principle calculations. *Ab*-initio calculations do not contain adjustable parameters except for the information about the constituent atoms (i.e the atomic number) and their geometric position. These calculations not only predict properties on existing materials that may be confirmed by experiments, but can also provide studies on materials that do not yet exist in nature, as is the case for the oxynitride spinel systems. Models that employ this methods are the Kohn Sham Density Functional Theory (KS-DFT), Møller-Plesset n-th order (MPn), Configuration Interaction (CI), and Coupled Cluster (CC) of the Post-HF as shown in Fig. 1.1. The most widespread approach for *ab*-initio quantitative calculations of solid material is the density functional

theory (DFT) [2].

This chapter deals with theoretical formulation of density functional theory, in which the electronic density plays the central role. And also shows how within this framework, the ground-state energy of a system can be determined.

3.2 Density Functional Theory

Density functional theory is one of the most popular and successful quantum mechanical approaches used in computing the electronic structure of matter. The importance of the DFT methods was emphasized by 1998 Nobel Prize in Chemistry, which was awarded to Walter Kohn [98], the founding father of DFT, and John Pople [99], who was instrumental in implementing DFT in computational Chemistry.

DFT is a theory of correlated many-body systems which requires a quantum mechanical approach in finding the ground state properties a system. According to quantum mechanics, the whole information of a system of interacting electrons and nuclei is contained in the many-body wave function Ψ, which can be obtained by solving the time-independent, non-relativistic Schrödinger equation:

$$\hat{\mathrm{H}}\Psi_{\mathrm{i}}(\vec{\mathrm{x}}_1, \vec{\mathrm{x}}_2, ..., \vec{\mathrm{x}}_{\mathrm{N}}, \vec{\mathrm{R}}_1, \vec{\mathrm{R}}_2, ..., \vec{\mathrm{R}}_{\mathrm{M}}) = \mathrm{E}_{\mathrm{i}}\Psi_{\mathrm{i}}(\vec{\mathrm{x}}_1, \vec{\mathrm{x}}_2, ..., \vec{\mathrm{x}}_{\mathrm{N}}, \vec{\mathrm{R}}_1, \vec{\mathrm{R}}_2, ..., \vec{\mathrm{R}}_M) \qquad (3.1)$$

where $\hat{\mathrm{H}}$ is the Hamiltonian for a system consisting of M nuclei and N electrons and the wave-function Ψ is a function of all the electronic and nuclear denoted by $\vec{\mathrm{x}}_{\mathrm{i}}$ and $\vec{\mathrm{R}}_{\mathrm{I}}$. The Hamiltonian can be written as the sum of the kinetic energies and Coulomb interaction of the electrons and ion cores (nuclei):

$$\hat{\mathrm{H}} = -\frac{1}{2}\sum_{\mathrm{i}=1}^{\mathrm{N}}\nabla_{\mathrm{i}}^2 - \frac{1}{2}\sum_{\mathrm{A}=1}^{\mathrm{M}}\frac{1}{\mathrm{M}_{\mathrm{A}}}\nabla_{\mathrm{A}}^2 + \sum_{\mathrm{i}=1}^{\mathrm{N}}\sum_{\mathrm{A}=1}^{\mathrm{M}}\frac{\mathrm{Z}_{\mathrm{A}}}{\mathrm{r}_{\mathrm{iA}}} + \sum_{\mathrm{i}=1}^{\mathrm{N}}\sum_{\mathrm{j}>\mathrm{i}}^{\mathrm{N}}\frac{1}{\mathrm{r}_{\mathrm{iA}}} + \sum_{\mathrm{A}=1}^{\mathrm{M}}\sum_{\mathrm{B}>\mathrm{A}}^{\mathrm{M}}\frac{\mathrm{Z}_{\mathrm{A}}\mathrm{Z}_{\mathrm{B}}}{\mathrm{R}_{\mathrm{AB}}} \qquad (3.2)$$

The sum over A and B run over the M nuclei while the sum over i and j run over the N electrons.

The first two parts describe the kinetic energy of the electrons and nuclei respectively. The remaining three terms represent the attractive electrostatic (Coulomb) interaction between the nuclei and the electrons and the repulsive potential due to the electron and nucleus-nucleus interactions respectively. The Hartree atomic unit mass will be used throughout this work, which means that all the physical quantities are expressed as multiples of fundamental constants and are set to unity (i.e $\hbar = h/2\pi = 4\pi\varepsilon_0 = m = e = 1$).

Due to the large difference in mass between the electrons and nuclei and the fact that the forces on the particles are the same, the electrons respond essentially instantaneously to the motion of the nuclei. Therefore the nuclei can be treated adiabatically, leading to a separation of electronic and nuclear coordinates in the many-body wave function (see Eqn. 3.2). This is called the Born-Oppenheimer approximation. The adiabatic principle reduces the many-body problem of Eqn. (3.2) to the solution of the dynamics of the electrons. The nuclei are considered to be fixed in space and do not move with their kinetic energy taken to be zero and the potential energy due to nucleus-nucleus repulsion is merely a constants. Thus, the Hamiltonian given in Eqn. (3.2). reduces to the so-called electronic Hamiltonian which is central to the theory of electronic structure.

$$\hat{\mathrm{H}}_{\mathrm{elec}} = -\frac{1}{2}\sum_{\mathrm{i}=1}^{\mathrm{N}} \nabla_{\mathrm{i}}^2 - \sum_{\mathrm{i}=1}^{\mathrm{N}}\sum_{\mathrm{A}=1}^{\mathrm{M}} \frac{\mathrm{Z_A}}{\mathrm{r_{iA}}} + \sum_{\mathrm{i}=1}^{\mathrm{N}}\sum_{\mathrm{j}>\mathrm{i}}^{\mathrm{N}} \frac{1}{\mathrm{r_{iA}}} \tag{3.3}$$

Another more transparent way of writing this Hamiltonian equation is:

$$\hat{\mathrm{H}}_{\mathrm{elec}} = \hat{\mathrm{T}} + \hat{\mathrm{V}}_{\mathrm{Ne}} + \hat{\mathrm{V}}_{\mathrm{ee}} \tag{3.4}$$

where $\hat{\mathrm{T}}$ is the kinetic energy term, $\hat{\mathrm{V}}_{\mathrm{Ne}}$ the interaction between the electrons and the nuclei (often called the external interaction, $\hat{\mathrm{V}}_{\mathrm{ext}}$) and $\hat{\mathrm{V}}_{\mathrm{ee}}$ the electron-electron Coulomb interactions. The solution to Eqn. (3.3) is the electronic wave function Ψ_{elec} and the electronic

energy E_{elec}.

With the use of the Born-Oppenheimer approximation, the simplified system consists of electron moving in a fixed external potential. However, Eqn. (3.3) still remains a non-trivial many body problem with a complexity far too big to solve even with modern computers. An enormous simplification of Eqn. (3.3) for studying realistic systems was the advent of density functional theory [100, 101].

DFT in its original formulation, is a theory of the electronic structure of atoms, molecules and solids in their ground states, in which the electronic (charge) density (- the real space distribution of electrons around the atoms) plays a central role. This implies that all aspects of the electronic structure of a system of interacting electrons, in the ground state, in an external potential, are completely determined by the electronic charge density $\rho(\mathbf{r})$ (Note that $\rho(\mathbf{r})$ is a function of only three variables). DFT methods have been found to be computationally efficient and its capable of handling infinite periodic systems and non-periodic systems of very many atoms, currently on the order of 10^3 [102]. The heart of this theory is the Hohenberg-Kohn theorems and the Kohn-Sham single particle equation.

3.2.1 The Hohenberg-Kohn Theorem

The two basic theorems of the density functional formalism were derived by Hohenberg and Kohn in 1964 [103]. The first theorem states that:

the external potential $V_{ext}(\mathbf{r})$ *is (to within a constant) a unique functional of the density* $\rho(\mathbf{r})$*; since, in turn* $V_{ext}(\mathbf{r})$ *fixes* $\hat{H}$ *we see that the full many particle ground-state energy is a unique functional of* $\rho(\mathbf{r})$.

which means:

$$V_{ext}(\mathbf{r}) \Longleftrightarrow \rho(\mathbf{r}) \tag{3.5}$$

The first theorem demonstrates that the electron density uniquely determines the Hamiltonian operator and thus all the properties of the system or (simply put) the energy is a unique functional of the ground state density $\mathrm{E}[\rho(\mathbf{r})]$.

The second Hohenberg-Kohn theory states that:

the functional that delivers the ground state energy of the system, delivers the lowest energy if and only if the input density is the true ground state density,

$$\mathrm{E}_0 \leq \mathrm{E}[\tilde{\rho}(\mathbf{r})] = \mathrm{T}[\tilde{\rho}(\mathbf{r})] + \mathrm{V}_{\mathrm{ext}}[\tilde{\rho}(\mathbf{r})] + \mathrm{V}_{\mathrm{ee}}[\tilde{\rho}(\mathbf{r})] \tag{3.6}$$

In other words, if given any trial density $[\tilde{\rho}(\mathbf{r})]$ representing the correct number of electrons N, the total energy calculated from this density cannot be lower than the true energy of the ground state E_0 and the ground state density can therefore be calculated, in principle exactly. Mathematically this means there is a variational principle for finding the charge density provided that the ground state density satisfy the following equation:

$$\delta\left[\mathrm{E}[\rho(\mathbf{r})] - \mu(\int \rho(\mathbf{r})\mathrm{d}\mathbf{r} - \mathrm{N})\right] = 0 \tag{3.7}$$

where μ is called the chemical potential. It is the langrange parameter associated with the restriction of the density to yield the correct total number of electrons N [101]. Note however, that this theorem is only applicable to ground states. (See Ref. [103] for proof of the first and second theorem).

The Hohenberg-Kohn theorem therefore, guarantees that the ground state energy and density correspond to the minimum of some functional $\mathrm{E}[\rho(\mathbf{r})]$ subject to the constraint that the density contains the correct number of electrons. However, the explicit form of the functional $\mathrm{E}[\rho(\mathbf{r})]$ is not known and an accurate computational implementation of DFT becomes a major challenge.

3.2.2 Kohn-Sham Equations

From the Hohenberg-Kohn theorem (using the electron density as the fundamental quantity), we know that the ground state energy of a system can be written as:

$$\mathrm{E}_0 = \min_{\rho\to\mathrm{N}}\left(\mathrm{F}[\rho(\mathbf{r})] + \int \rho(\mathbf{r})\mathrm{V}_{\mathrm{Ne}}\mathrm{d}\mathbf{r}\right) \tag{3.8}$$

where the universal functional $\mathrm{F}[\rho]$ contains the individual contributions of the kinetic energy, $\mathrm{T}[\rho(\mathbf{r})]$, the coulomb interaction, $\mathrm{J}[\rho(\mathbf{r})]$, and the non-classical portion due to self-interaction correction, exchange (i.e., antisymmetry), and electron correlation effects,

$$\mathrm{F}[\rho(\mathbf{r})] = \mathrm{T}[\rho(\mathbf{r})] + \mathrm{J}[\rho(\mathbf{r})] + \mathrm{E}_{\mathrm{ncl}}[\rho(\mathbf{r})] \tag{3.9}$$

Equation (3.8) can be rewritten as:

$$\mathrm{E}[\rho(\mathbf{r})] = \mathrm{T}[\rho(\mathbf{r})] + \mathrm{J}[\rho(\mathbf{r})] + \mathrm{E}_{\mathrm{ncl}}[\rho(\mathbf{r})] + \int \rho(\mathbf{r})\mathrm{V}_{\mathrm{ext}}\mathrm{d}\mathbf{r} \tag{3.10}$$

The only known term of equation (3.9) is $\mathrm{J}[\rho(\mathbf{r})]$ (also called Hartree energy) which is defined as:

$$\mathrm{J}[\rho] = \frac{1}{2}\int\int \frac{\rho(\mathbf{r})\rho(\mathbf{r}')}{|\mathbf{r}-\mathbf{r}'|}\mathrm{d}\mathbf{r}\mathrm{d}\mathbf{r}' \tag{3.11}$$

while the explicit expressions for $\mathrm{T}[\rho]$ and $\mathrm{E}_{\mathrm{ncl}}[\rho]$ is unknown. To solve this problem Kohn and Sham in 1965 [104] invented an ingenious indirect approach to approximate to a good accuracy, the kinetic and electron-electron functionals. They suggested to calculate the exact kinetic energy of an auxiliary set of one-electron orbitals, of a system of non-interactive electrons with the same density as the real, interacting one

$$\mathrm{T}_{\mathrm{KS}}[\rho] = -\frac{1}{2}\sum_{i=1}^{\mathrm{N}}\langle\varphi_i|\nabla^2|\varphi_i\rangle \tag{3.12}$$

where φ_i are the orbitals of the non-interactive system and T_{KS} (i.e., Kohn-Sham energy) is not equal to the true kinetic energy of the system.

The connection of this artificial system to the one we are really interested in is now established by choosing the effective potential V_{eff} such that the density resulting from the summation of the moduli of the squared orbitals φ_i exactly equals the ground state density of our real target system of the interacting electrons. If there are N electrons in the system the electron density can be calculated from:

$$\rho_S(\mathbf{r}) = \sum_{i=1}^{N} |\varphi_i|^2 = \rho_0(\mathbf{r}) \tag{3.13}$$

The energy fuctional from equation (3.8) within the Kohn-Sham approach can be rewritten as:

$$E[\rho] = T_{KS}[\rho(\mathbf{r})] + \int \rho(\mathbf{r}) V_{ext} d\mathbf{r} + J[\rho(\mathbf{r})] + E_{xc}[\rho(\mathbf{r})] \tag{3.14}$$

or from equation (3.11)

$$E[\rho] = T_{KS}[\rho(\mathbf{r})] + \int \rho(\mathbf{r}) V_{ext} d\mathbf{r} + \frac{1}{2} \int \int \frac{\rho(\mathbf{r})\rho(\mathbf{r}')}{|\mathbf{r} - \mathbf{r}'|} d\mathbf{r} d\mathbf{r}' + E_{xc}[\rho(\mathbf{r})] \tag{3.15}$$

where $E_{xc}[\rho]$ is the exchange-correlation functional. It captures all the many-body interactions and contains everything that is unknown. It can be expressed as:

$$E_{xc}[\rho] = (T[\rho] - T_{KS}[\rho]) + (E_{ee}[\rho] - J[\rho]) \tag{3.16}$$

All quantities except for $E_{xc}[\rho]$ are known and could be easily calculated from the wave-function of the non-interacting system.

Applying the variational theorem from equation (3.7) and expressing the functional from equation (3.15) explicitly in terms of the density built from non-interacting orbitals in equation (3.13), the resulting Kohn-Sham equations, which minimize the energy satisfy

the following set of equations:

$$\left[-\frac{1}{2}\nabla^2 + \mathrm{V_{eff}}(\mathbf{r}) \right] \varphi_i(\mathbf{r}) = \varepsilon_i \varphi_i(\mathbf{r}) \tag{3.17}$$

$$\mathrm{V_{eff}}(\mathbf{r}) = \mathrm{V_{ext}}(\mathbf{r}) + \int \mathrm{d}\mathbf{r}' \frac{\rho(\mathbf{r}')}{|\mathbf{r} - \mathbf{r}'|} + \mathrm{V_{xc}}(\mathbf{r}) \tag{3.18}$$

$\mathrm{V_{xc}}$ is the exchange-correlation potential which is defined as the functional derivative of $\mathrm{E_{xc}}$ with respect to the density [100, 101]:

$$\mathrm{V_{xc}}(\mathbf{r}) = \frac{\delta \mathrm{E_{xc}}[\rho(\mathbf{r})]}{\delta \rho(\mathbf{r})} \tag{3.19}$$

The Kohn-Sham equations (3.17)-(3.18) represent a mapping of the interacting many-body system onto a system of non-interacting electrons moving in an effective potential due to all the other electrons. If the exchange-correlation energy functional were known exactly, then the exact ground state energy and density of the many-body electron problem could be found. The Kohn-Sham equations must be solved self-consistently so that the occupied electronic states generate an electronic charge density that produces the electron potential that was used to construct the equations [105, 106]. The practical implementation of the Kohn-Sham scheme with DFT requires that an approximation has to be made for $\mathrm{E_{xc}}$ (or $\mathrm{V_{xc}}$).

3.3 Exchange-Correlation Functional

The exchange-correlation functional from equation (3.16) is the sum of the error made in using a non-interacting kinetic energy and the error made in treating the electron-electron interaction classically. $\mathrm{E_{xc}}$ is of central importance in the accuracy of DFT calculations, and there has been much work in finding its accurate forms which can only be resolve by approximations. There are basically different types of approximations involved in a

DFT calculation for the unknown E_{xc} functional. The approximations that is of interest in this dissertation can be classified into Local functional (Local Density Approximation (LDA)) and Semi-local or gradient dependent functional (Generalized Gradient Approximation (GGA)).

3.3.1 Local Density Approximation (LDA)

The simplest method of describing the exchange-correlation energy of an electronic system is to use the Local Density Approximation (LDA). It is the basis of all approximate exchange-correlation functions. At the center of this model is the idea of an uniform electron gas. This is a system in which electrons move on a positive background charge distribution such that the total ensemble is neutral. A uniform electron gas is such that in the limit $N \rightarrow \infty$, $V \rightarrow \infty$ (where N is the number of electron and V is the volme), with density, $\rho = \frac{N}{V}$, remaining finite and attains a constant value everywhere. LDA assumes that exchange-correlation energy per electron at a point $\mathbf{r}$ in the electron gas, ε_{xc}, is equal to the exchange-correlation energy per electron in a uniform (homogeneous) electron gas that has the same density as the electron as point $\mathbf{r}$. Thus an approximation of the form is expressed as:

$$E_{xc}^{LDA}[\rho] = \int \rho(\mathbf{r})\varepsilon_{xc}(\rho(\mathbf{r}))d\mathbf{r} \tag{3.20}$$

where $\varepsilon_{xc}(\rho(\mathbf{r}))$ is the exchange-correlation energy density of the uniform electron gas of density $\rho(\mathbf{r})$. It is a function of the local value of the density within the LDA and can be separated into exchange and correlation potential contributions:

$$\varepsilon_{xc}(\rho) = \varepsilon_{x}(\rho) + \varepsilon_{c}(\rho) \tag{3.21}$$

The exchange part, ε_x, which represents the exchange energy of an electron in a uniform electron gas of a particular density, was originally derived by Bloch and Dirac in the late

1920's [107]:

$$\varepsilon_{\mathrm{x}}(\rho) = -\frac{3}{4}\left(\frac{3\rho(\mathbf{r})}{\pi}\right)^{1/3} \tag{3.22}$$

The explicit expression for the correlation energy density, $\varepsilon_{\mathrm{c}}(\rho)$, is unknown. However, highly accurate numerical quantum Monte-Carlo simulations of the homogeneous electron gas can be determined from the work of Ceperley and Alder [108]. On the basis of these results various authors have presented an analytical parameterizations (or expressions) of $\varepsilon_{\mathrm{c}}(\rho)$ based on the sophisticated interpolation schemes. Notable among them are: Hedin and Lundqvist [109], Vosko *et al*. [110], and Perdew and Zunger parameterizations [111]. The parameterization by Perdew and Zunger have been employed in this work.

3.3.2 Generalized Gradient Approximation (GGA)

As LDA approximates the energy of the true density by the energy of a local constant density, it fails in situations where the density is a spatially varying density $\rho(\mathbf{r})$. The first logical step to go beyond LDA was the suggestion of using not only the information of the density $\rho(\mathbf{r})$ at a particular point $\mathbf{r}$, but to supplement the density with the information about the gradient of the charge density, $\nabla\rho(\mathbf{r})$ in order to account for the non-homogeneity of the true electron density. The functionals that include the gradients of the charge density are collectively known as the Generalized Gradient Approximations (GGA) [112, 113]. The exchange-correlation functional, $\mathrm{E_{xc}}$, can be written as:

$$\mathrm{E}_{\mathrm{xc}}^{\mathrm{GGA}}[\rho_{\uparrow}, \rho_{\downarrow}] = \int \mathrm{f}\Big(\rho_{\uparrow}(\mathbf{r}), \rho_{\downarrow}(\mathbf{r}), \nabla\rho_{\uparrow}(\mathbf{r}), \nabla\rho_{\downarrow}(\mathbf{r})\Big)\mathrm{d}\mathbf{r} \tag{3.23}$$

Several suggestions for the explicit dependence of this intergrand f on the densities and their gradients exist, including semi-empirical functionals which contain parameters that are calibrated against reference values rather than being derived from first principles. In practice, $\mathrm{E}_{\mathrm{xc}}^{\mathrm{GGA}}$ is usually split into its exchange and correlation contributions:

$$E_{xc}^{GGA} = E_{x}^{GGA} + E_{c}^{GGA} \tag{3.24}$$

and approximations for the two terms are sought individually. The exchange part can be written as:

$$E_{x}^{GGA} = E_{x}^{LDA} - \sum_{\sigma} \int F(s_{\sigma}) \rho_{\sigma}^{4/3}(\mathbf{r}) d\mathbf{r} \tag{3.25}$$

The argument of the function F is the reduced density gradient for spin σ:

$$s_{\sigma}(\mathbf{r}) = \frac{|\nabla \rho_{\sigma}(\mathbf{r})|}{\rho_{\sigma}^{4/3}(\mathbf{r})} \tag{3.26}$$

where s_{σ} is to be understood as a local inhomogeneity parameter. It assumes large values not only for large gradients, but also in regions of small densities, such as exponential tails far from the nuclei. Likewise, small values of s_{σ} occur for small gradients, typical for bonding regions, but also regions for large density [100].

Two main classes of realizations have been put forward for the function F. The first one is based on a GGA exchange functional developed by Becke [114]. This functional is abbreviated simply as B or sometimes as B88. Functional which are related to this approach includes: Filatov and Theil (FT97) [115], 1997, Perdew (PW92), 1992 [112, 116] and the CAM(A) and CAM(B) functionals developed by Handy *et al* [117, 118] among others.

The second class of GGA exchange functionals use for F a rational function of the reduced density gradient. Prominent representative includes: early functionals of Berke (B86), 1986 [119], recent implementation of Perdew, Burke, and Ernzerhof (PBE), 1996 [113], and functional by Lacks and Gordon (LG), 1993 [120]. In this work we have used the GGA functional developed by Perdew and Wang (PW92)[112]. PW92 includes a real space cut-off also for the correlation functional and takes the Becke exchange with only small refinements. It fulfills almost all of the scaling relations known, including such that were only found after the functional's formulation [2].

3.4 Plane Wave Pseudopotential Method

The preceding sections have demonstrated how the complicated many-body problem of strongly interacting electrons and nuclei can be mapped onto a problem of single-particle moving in an effective external potential for a set of fixed nuclei. In practice, however, the numerical solution of the single-particle Kohn-Sham equations (see eqn. (3.17) and (3.18)) typically proceeds by expanding these equations in a set of basis functions.

3.4.1 Plane Wave Basis Set

Plane waves are classified as fixed basis functions that are orthonormal and energy-independent. They are efficiently used to expand the periodic functions of a solid or crystal. For periodic systems such as the one under study, the potential can be expressed as:

$$\mathrm{V}(\mathbf{r} + n\mathbf{a}) = \mathrm{V}(\mathbf{r}) \tag{3.27}$$

where **a** is a lattice vector and n is an integer.

Applying Bloch's theorem which states that in a periodic solid each electronic wave function can be written as the product of a cell periodic part and a wavelike part [121]:

$$\psi_i(\mathbf{r}) = e^{i\mathbf{kr}}\mathrm{f}_i(\mathbf{r}) \tag{3.28}$$

The cell periodic part of the wave function can be expanded using a basis set of plane waves whose wave vectors are reciprocal lattice vectors of the crystal:

$$\mathrm{f}_i(\mathbf{r}) = \sum_{\mathbf{G}} c_{i,\mathbf{G}} e^{i\mathbf{Gr}} \tag{3.29}$$

where **G** is the reciprocal lattice vector. Thus the electronic wave functions can be expressed as a linear combination of plane waves:

$$\psi_i(\mathbf{r}) = \sum_{\mathbf{G}} c_{i,\mathbf{G}} e^{i(\mathbf{K}+\mathbf{G})\mathbf{r}} \tag{3.30}$$

The summation is over all the reciprocal lattice vector and c_i are the expansion coefficients. In principle, this shows that an infinite plane waves basis set is required to expand the electronic wave functions. The number of wave functions used is controlled by the largest wave vector in the expansion in equation (3.29). This is equivalent to imposing a cutoff on the kinetic energy, as the kinetic energy of an electron with wave vector **K** is given by:

$$\mathrm{E_K} = \frac{\hbar^2 |\mathbf{K}|^2}{2m} \tag{3.31}$$

If a continuum of plane wave basis set states were required to expand each electronic wave function, the basis set would be infinitely large no matter how small the cutoff kinetic energy. Application of the Bloch theorem allows the electronic wave functions to be expanded in terms of a discrete set of plane waves. Introduction of an energy cutoff to the plane wave basis set produces a finite basis set.

When plane waves are used as a basis set for the electronic wave functions, the Kohn-Sham equations take on a very simple form [105]:

$$\begin{aligned} \Big\{ \sum_{\mathbf{G}'} \frac{\hbar^2}{2m} |\mathbf{K}+\mathbf{G}|^2 \delta_{\mathbf{G}\mathbf{G}'} + \mathrm{V_{Ne}}(\mathbf{G}-\mathbf{G}') \\ + \mathrm{V_{ee}}(\mathbf{G}-\mathbf{G}') + \mathrm{V_{xc}}(\mathbf{G}-\mathbf{G}') \Big\} c_{i,\mathbf{K}+\mathbf{G}'} = \varepsilon_i c_{i,\mathbf{K}+\mathbf{G}'} \end{aligned} \tag{3.32}$$

where $\mathrm{V_{Ne}}(\mathbf{G}-\mathbf{G}')$, $\mathrm{V_{ee}}(\mathbf{G}-\mathbf{G}')$ and $\mathrm{V_{xc}}(\mathbf{G}-\mathbf{G}')$ are the Fourier transforms of the electron-nuclei, electron-electron coulomb, and the exchange-correlation potentials. In this form, the kinetic energy is diagonal, and the various potentials are described in terms of their fourier transforms.

A plane wave basis sets is convenient for many reasons such as its easy computer imple-

mentation, the simple diagonal form of the kinetic operator, the efficiency of Fast Fourier Transforms (FFT) between real and reciprocal space, and since it is a transparent and easily understood basis set. Plane waves do not depend on the positions of the atoms and are therefore non-local. Unlike the localized basis sets, correction terms are not needed for the calculation of forces in plane wave expansion. However, the disadvantage of using a plane wave basis set is its inefficiency. More so, due to the nodal structure of the valence wave functions in the core region of the atom, a prohibitively large number of plane waves would be needed for a good representation of these fast oscillations.

3.4.2 Monkhorst-Pack Grids

The finite number of basis set or K-points introduced by Bloch theorem can be used in sampling of the Brillouin zone. A standard method for sampling this points during a self-consistent calculation to find the electronic ground state is the Monkhorst-Pack grid.

Monkhorst-Pack grid [122] is an unbiased method of choosing a set of special K-points in the Brillouin zone which provides an efficient means of integrating periodic functions of the wave vector. The integration can be over the entire Brillouin zone or over specified portions. This points simply generates an expansion of periodic function in reciprocal space functions with proper symmetries which is crucial for the convergence of the results. The dimensions used for the sampling of the Monkhorst-Pack grid in this thesis are given in Chapter 4.

3.4.3 Pseudopotentials

An efficient solution to the problem of plane wave method is by introducing the concept of Pseudopotential approximation which allows the electronic wave functions to be expanded using a much smaller number of plane waves. The pseudopotential approximation is based upon the observation that the core (inner) electrons of different atoms are relatively unaffected by the chemical environment of the atom and that only the valence electrons partici-

pate strongly in interactions between atoms. Thus, the wave functions in the core region are replaced by smoothly varying pseudo wave functions and the interaction in the core region is replaced by a constructed pseudopotential. This is referred as the Frozen-Core approximation. The relationship between all-electron and pseudopotentials and wave functions are illustrated schematically in Fig. 3.1.

The wave functions for the valence electrons are replaced with the pseudo wave functions to give the same energy levels as the all-electron wave functions. The pseudo wave functions differ from the all-electron wave functions only inside a region around the nucleus and are constructed to be node-less. If the pseudo wave function still contained nodes they would not describe the lowest valence state. The nodes in the valence wave functions are necessary to make valence states orthogonal to the core states. Node-less pseudo wave functions reduces the number of required pane waves considerably. The pseudo wave functions corresponding to this modified potential do not exhibit the rapid oscillations of the true wave functions, dramatically reducing the number of of plane waves needed for their representation. A pseudopotential is constructed such that it matches the true potential outside a given radius called the core radius, $\mathbf{r}_c$. Similarly, each pseudo wave function must match the corresponding true wave function beyond this distance [2, 105].

Common pseudopotentials are generated following the prescription of, e.g., Bachelet, Hamann and Schlüter [123], Kleinman and Bylander [124], Vanderbilt (Ultrasoft Pseudopotential) [125] or Troullier and Martins [126]. A more advance method that goes beyond the concept of pseudopotentials called the Projected Augmented Wave (PAW) potentials have been implemented in this work.

Projector Augmented Wave (PAW)

The projector augmented wave method is an all-electron method for efficient ab-initio molecular dynamics simulations with full wave functions. In principle, the PAW method, aims to take the advantages and accuracy of all-electron methods available to the formally

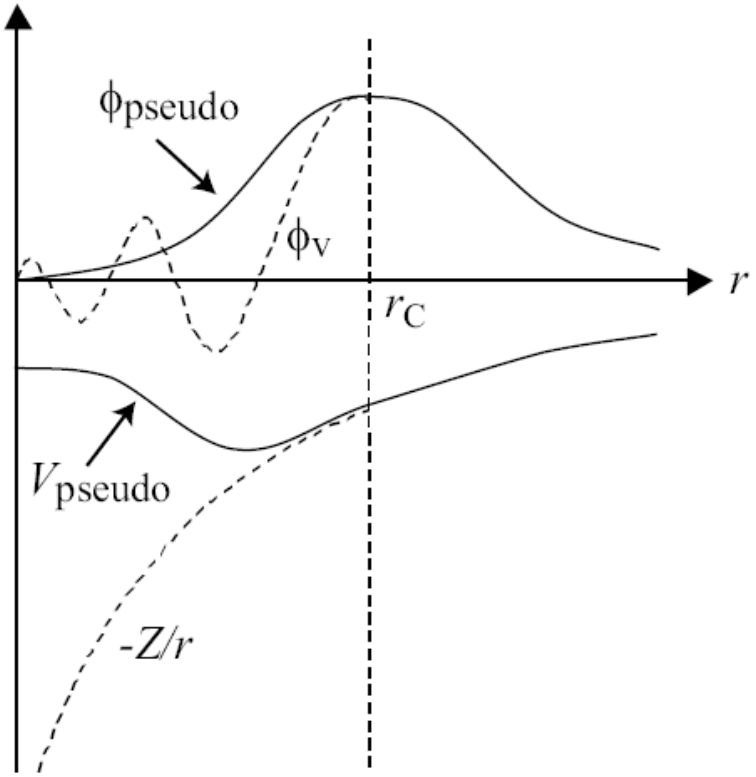


Figure 3.1: A schematic illustration of all-electron (dashed lines) and pseudo- (solid lines) potentials and their corresponding wave functions. The radius at which all-electron and pseudopotential values match is $\mathbf{r}_c$. [2]

more simple pseudopotential approach. It was developed by Peter Blöchl in 1994 [127] and was further established by the Kresse and Joubert (1999) [128] where they derived the relationship that exist between the ultrasoft pseudopotential and the PAW method. The PAW method describes the wave function by a superposition of the plane wave part, the so-called pseudo wave function, and expansions into atomic and pseudo atomic orbitals at each atom. For a complete description of the PAW potential method see Refs. [127, 128].

3.5 The Vienna Ab-Initio Simulation Package (VASP)

The Vienna Ab-Initio Simulation Package (VASP) is a density functional code developed by Georg Kresse and Jürgen Furthmüller [129, 130, 131, 132]. VASP includes an optimised

set of ultrasoft pseudopotentials and PAW potentials for all elements of the periodic system. It solves the Kohn-Sham equations of local density or spin-density functional theory (see Eqn. (3.19)) iteratively within a plane wave basis set. The approach implemented in VASP is based on the (infinite-temperature) local density approximation. The gradient corrected functionals are also implemented to account for the non-locality in exchange-correlation functionals. Detailed descriptions of the methods used in VASP package can be found in the VASP manual home page **http://cms.mpi.univie.ac.at/vasp**.

Chapter 4

Theoretical Study of Spinel Oxynitride M_3NO_3

4.1 Computational Parameters

The local density approximation (LDA) functional of Ceperley and Alder [108], as parameterized by perdew-Zunger [111] and the general gradient approximation (GGA) functional of Perdew-Wang [112] for the exchange-correlation potential in the density functional theory (DFT) and the interaction between the ions and the electrons described by projector augmented wave (PAW) pseudopotential [128], as outlined in Chapter 3 have been implemented through the VASP structure code [129, 130, 131, 132]. The wave function of the valence electrons is also expanded into a plane wave basis set using a cutt-off energy of 500 eV to calculate the optimized geometries, elastic constants, electronic properties and relative stability of oxynitride spinel structure. The d electrons in the core of the atom have been treated as valence electrons.

All results rely on well converged structures and the integration of the special K-points sampling of the Brillouin zone. The Monkhorst-pack grid [122] have been employed to achieve convergence. The energies are converged to better than 10^{-4} eV/atom. This is

one of the methods [122, 133] devised for obtaining very accurate approximations to the electronic potential and the contribution to the total energy from the filled electronic band by calculating the electronic states at special sets of K-points in the Brillouin zone. We used the following Monkhorst-pack grid for the integration of the reciprocal space: $4 \times 4 \times 4$ for the oxynitride M_3NO_3, $8 \times 8 \times 8$ for group-III oxides M_2O_3 and $8 \times 8 \times 8$ for nitrides MN. This is as a result of the differences in crystal symmetry between the compounds. All atoms in the unit cell were fully relaxed and the cell geometry fully optimized.

A comparison of LDA and GGA results is useful in general. Typically, the GGA overestimates slightly cell parameters and underestimates bulk modulus, while the LDA underestimates both lattice parameters and bulk modulus. For a comparison of structures with different environments of the atoms, we have chosen to use the LDA results to compute the trends and some other properties.

4.2 Structural Properties of Spinels

Calculations of bulk ground state properties, such as lattice contants, atomic coordinates, bond lengths, their elastics constants (see section 4.3) helps us to understand, characterize, and predict mechanical properties of materials for their industrial applications. Crystal structure of the spinels have explicitly been examined at length by several authors as introduced in Chapter 1. Here we model the form of spinel oxynitride M_3NO_3, (M = B, Al, Ga and In), and have considered a representative of 56-atom unit cells and assuming a M:N:O ratio of 3:1:3 that corresponds to an ideal stoichiometry of spinel. The structure consists of a series of interpenetrating of pseudo-cubic sub-lattice structures that can be categorized into four-fold symmetries which are commonly used for spinel structure. The M atoms fill the all the cation positions of the spinel structure, both the tetrahedrally coordinated and the octahedrally coordinated sites. The anion sublattice is made up by both N and O, in quantities of one-fourth and three-quarter of all available 32 anion positions, respectively. Each

of the tetrahedral *M* atoms have three oxygen nearest neighbors and one nitrogen neighbor (MO_3N). Of the *M* atoms at the octahedral sites, four *M* atoms have only one oxygen nearest neighbor (MO_6) while the remaining twelve *M* atoms at the octahedral sites have two nitrogen nearest neighbors and four oxygen neighbors (MN_2O_4). Nominally the symmetry of this spinel structure is $P\bar{4}3m$ (No. 215) and is shown in Figure 4.1. As shown in the Figure the most significant element in this cubic unit cell consists of N atoms arrange in a tetrahedral symmetry about the 56 atom unit cell. This structure is quite unique because of the symmetry of the N atoms and as such has no normal or inversion characteristics as discussed earlier for the other spinels. The structure has been observed in Ga_3NO_3 system [134, 135, 136, 137].

Table 4.2 and 4.3 explicitly shows the list of all the fractional coordinate of the various M_3NO_3 spinel structure for both the LDA and GGA. The extensive listing of the coordinates for the cubic cell embraces the space group symmetry of spinel. The calculated optimized structures for all the spinels are given in Table 4.1 and where possible (especially for Ga_3NO_3), a comparison has been made with experiment. The trends can be seen more easily: on going from B_3NO_3 to Al_3NO_3 to Ga_3NO_3 to In_3NO_3. It is seen that on going down the columns of the periodic table, the lattice constant exhibits an increase in accordance with the large size of the atom.

Table 4.1: Structural parameters of B_3NO_3, Al_3NO_3, Ga_3NO_3, In_3NO_3.

Material	LDA (Å)	GGA (Å)	Experiment (Å)
B_3NO_3	6.842	6.947	
Al_3NO_3	7.937	8.057	
Ga_3NO_3	8.267	8.425	8.20 [134]
In_3NO_3	9.285	9.285	

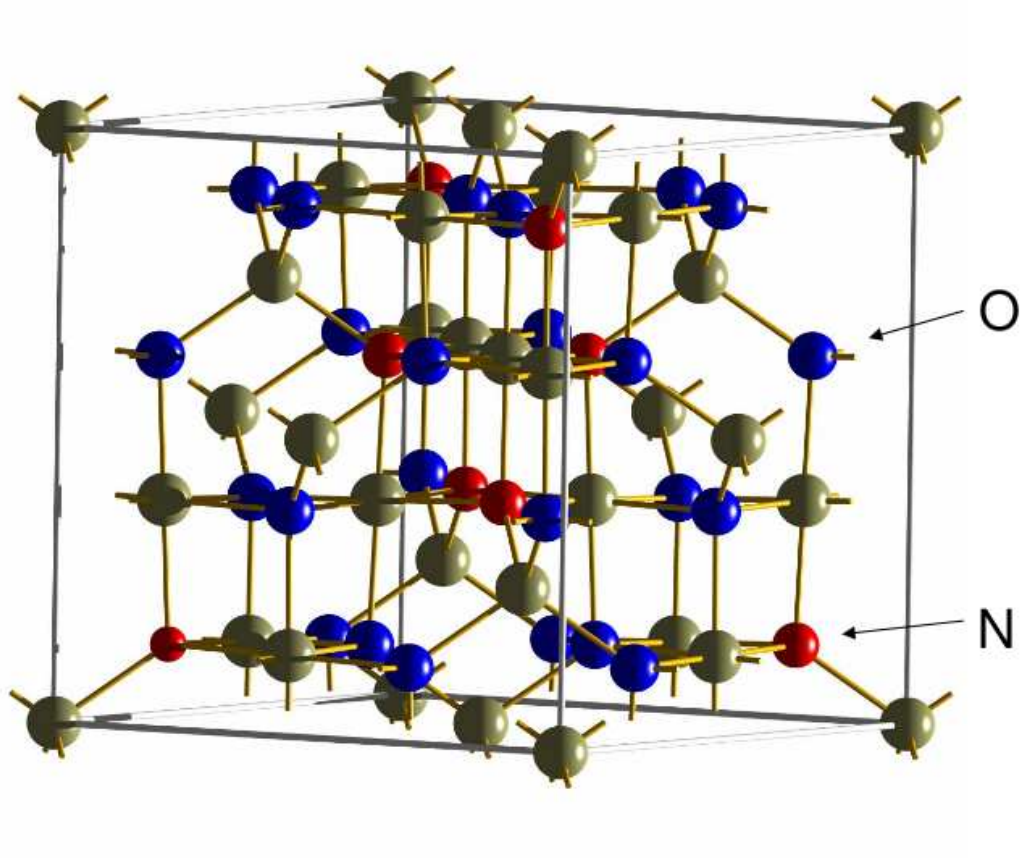


Figure 4.1: The cubic unit cell of the M_3NO_3 oxynitride spinel structure. The N atoms are at a tetrahedral position inside the cubic unit cell.

Table 4.2: Fractional coordinates of the cubic spinel lattice for the LDA. The symmetry of this spinel is $P\bar{4}3m$ (No. 215) and it retains the four-fold symmetry in their site occupancy.

No	Atom	Fractional coordinate	Atom	Fractional coordinate	Atom	Fractional coordinate	Atom	Fractional coordinate
1	B	.6116, .6116, .6116	Al	.6216, .6216, .6216	Ga	.6192, .6192, .6192	In	.6209, .6209, .6209
2	B	.8801, .8801, .6458	Al	.8758, .8758, .6300	Ga	.8757, .8757, .6317	In	.8754, .8754, .6298
3	B	.6458, .8801, .8801	Al	.6300, .8758, .8758	Ga	.6317, .8757, .8757	In	.6298, .8754, .8754
4	B	.8801, .6458, .8801	Al	.8758, .6300, .8758	Ga	.8757, .6317, .8757	In	.8754, .6298, .8754
5	B	.6458, .1199, .1199	Al	.6300, .1242, .1242	Ga	.6317, .1243, .1243	In	.6305, .1241, .1241
6	B	.8801, .3542, .1199	Al	.8758, .3700, .1242	Ga	.8757, .3683, .1243	In	.8760, .3696, .1243
7	B	.6116, .3883, .3883	Al	.6216, .3784, .3784	Ga	.6192, .3808, .3808	In	.6214, .3791, .3791
8	B	.8801, .1199, .3542	Al	.8758, .1242, .3700	Ga	.8757, .1243, .3683	In	.8760, .1243, .3696
9	B	.1199, .6458, .1199	Al	.1242, .6300, .1242	Ga	.1243, .6317, .1243	In	.1241, .6305, .1241
10	B	.3542, .8801, .1199	Al	.3700, .8758, .1242	Ga	.3683, .8757, .1243	In	.3696, .8760, .1243
11	B	.1199, .8801, .3542	Al	.1242, .8758, .3700	Ga	.1243, .8757, .3683	In	.1243, .8760, .3696
12	B	.3883, .6116, .3883	Al	.3784, .6216, .3784	Ga	.3808, .6192, .3808	In	.3791, .6214, .3791
13	B	.1199, .1199, .6458	Al	.1242, .1242, .6300	Ga	.1243, .1243, .6317	In	.1241, .1241, .6305
14	B	.3883, .3883, .6116	Al	.3784, .3784, .6216	Ga	.3808, .3808, .6192	In	.3791, .3791, .6214
15	B	.1199, .3542, .8801	Al	.1242, .3700, .8758	Ga	.1243, .3683, .8757	In	.1243, .3696, .8760
16	B	.3542, .1199, .8801	Al	.3700, .1242, .8758	Ga	.3683, .1243, .8757	In	.3696, .1243, .8760
17	B	1.000, 1.000, 1.000	Al	1.000, 1.000, 1.000	Ga	1.000, 1.000, 1.000	In	.0004, .0004, .0004
18	B	1.000, .5000, .5000	Al	1.000, .5000, .5000	Ga	.0000, .5000, .5000	In	1.001, .5000, .5000
19	B	.5000, 1.000, .5000	Al	.5000, 1.000, .5000	Ga	.5000, .0000, .5000	In	.5000, 1.001, .5000
20	B	.5000, .5000, 1.000	Al	.5000, .5000, 1.000	Ga	.5000, .5000, .0000	In	.5000, .5000, 1.001
21	B	.7469, .7469, .2531	Al	.7476, .7476, .2523	Ga	.7474, .7474, .2526	In	.7458, .7458, .2538
22	B	.7469, .2531, .7469	Al	.7476, .2523, .7476	Ga	.7474, .2526, .7474	In	.7458, .2538, .7458
23	B	.2531, .7469, .7469	Al	.2523, .7476, .7476	Ga	.2526, .7474, .7474	In	.2538, .7458, .7458
24	B	.2530, .2530, .2530	Al	.2523, .2523, .2523	Ga	.2526, .2526, .2526	In	.2544, .2544, .2544
25	N	.8672, .8672, .8672	N	.8644, .8644, .8644	N	.8651, .8651, .8651	N	.8628, .8628, .8628
26	N	.8672, .1328, .1328	N	.8644, .1356, .1356	N	.8651, .1349, .1349	N	.8633, .1367, .1367
27	N	.1328, .8672, .1328	N	.1356, .8644, .1356	N	.1349, .8651, .1349	N	.1367, .8633, .1367
28	N	.1328, .1328, .8672	N	.1356, .1356, .8644	N	.1349, .1349, .8651	N	.1367, .1367, .8633
29	N	.3793, .6207, .6207	N	.3816, .6184, .6184	N	.3801, .6199, .6199	N	.3822, .6178, .6178
30	N	.3793, .3793, .3793	N	.3816, .3816, .3816	N	.3801, .3801, .3801	N	.3826, .3826, .3826
31	N	.6207, .6207, .3793	N	.6184, .6184, .3816	N	.6199, .6199, .3801	N	.6178, .6178, .3822
32	N	.6207, .3793, .6207	N	.6184, .3816, .6184	N	.6199, .3801, .6199	N	.6178, .3822, .6178
33	O	.6243, .1174, .8826	O	.6101, .1170, .8830	O	.6110, .1179, .8821	O	.6091, .1161, .8835
34	O	.8826, .1174, .6243	O	.8830, .1170, .6101	O	.8821, .1179, .6110	O	.8835, .1161, .6091
35	O	.1174, .6243, .8826	O	.1170, .6101, .8830	O	.1179, .6110, .8821	O	.1161, .6091, .8835
36	O	.1174, .8826, .6243	O	.1170, .8830, .6101	O	.1179, .8821, .6110	O	.1161, .8835, .6091
37	O	.6243, .8826, .1174	O	.6101, .8830, .1170	O	.6110, .8821, .1179	O	.6091, .8835, .1161
38	O	.8826, .6243, .1174	O	.8830, .6101, .1170	O	.8821, .6110, .1179	O	.8835, .6091, .1161
39	O	.1174, .1174, .3757	O	.1170, .1170, .3899	O	.1179, .1179, .3890	O	.1166, .1166, .3910
40	O	.8825, .8825, .3757	O	.8830, .8830, .3899	O	.8821, .8821, .3890	O	.8836, .8836, .3904
41	O	.1174, .3757, .1174	O	.1170, .3899, .1170	O	.1179, .3890, .1179	O	.1166, .3910, .1166
42	O	.8825, .3757, .8825	O	.8830, .3899, .8830	O	.8821, .3890, .8821	O	.8836, .3904, .8836
43	O	.3757, .1174, .1174	O	.3899, .1170, .1170	O	.3890, .1179, .1179	O	.3910, .1166, .1166
44	O	.3757, .8825, .8825	O	.3899, .8830, .8830	O	.3890, .8821, .8821	O	.3904, .8836, .8836
45	O	.6302, .6302, .8783	O	.6337, .6337, .8701	O	.6327, .6327, .8717	O	.6334, .6334, .8699
46	O	.8783, .6302, .6302	O	.8701, .6337, .6337	O	.8717, .6327, .6327	O	.8699, .6334, .6334
47	O	.6302, .8783, .6302	O	.6337, .8701, .6337	O	.6327, .8717, .6327	O	.6334, .8699, .6334
48	O	.8783, .3698, .3698	O	.8701, .3663, .3663	O	.8717, .3673, .3673	O	.8706, .3662, .3662
49	O	.6302, .1217, .3698	O	.6337, .1298, .3663	O	.6327, .1283, .3673	O	.6340, .1303, .3662
50	O	.6302, .3698, .1217	O	.6337, .3663, .1298	O	.6327, .3673, .1283	O	.6340, .3662, .1303
51	O	.3698, .8783, .3698	O	.3663, .8701, .3663	O	.3673, .8717, .3673	O	.3662, .8706, .3662
52	O	.1217, .6302, .3698	O	.1298, .6337, .3663	O	.1283, .6327, .3673	O	.1303, .6340, .3662
53	O	.3698, .6302, .1217	O	.3663, .6337, .1298	O	.3673, .6327, .1283	O	.3662, .6340, .1303
54	O	.3698, .3698, .8783	O	.3663, .3663, .8701	O	.3673, .3673, .8717	O	.3662, .3662, .8706
55	O	.3698, .1217, .6302	O	.3663, .1298, .6337	O	.3673, .1283, .6327	O	.3662, .1303, .6340
56	O	.1217, .3698, .6302	O	.1298, .3663, .6337	O	.1283, .3673, .6327	O	.1303, .3662, .6340

Table 4.3: Fractional coordinates of the cubic spinel lattice for the GGA. The symmetry of this spinel is $P\bar{4}3m$ (No. 215) and it retains the four-fold symmetry in their site occupancy.

No	Atom	Fractional coordinate	Atom	Fractional coordinate	Atom	Fractional coordinate	Atom	Fractional coordinate
1	B	.6109, .6109, .6109	Al	.6177, .6177, .6177	Ga	.6183, .6183, .6183	In	.6216, .6216, .6216
2	B	.8811, .8811, .6481	Al	.8754, .8754, .6322	Ga	.8759, .8759, .6328	In	.8758, .8758, .6300
3	B	.6481, .8811, .8811	Al	.6322, .8754, .8754	Ga	.6328, .8759, .8759	In	.6300, .8758, .8758
4	B	.8811, .6481, .8811	Al	.8754, .6322, .8754	Ga	.8759, .6328, .8759	In	.8758, .6300, .8758
5	B	.6483, .1187, .1187	Al	.6322, .1246, .1246	Ga	.6328, .1241, .1241	In	.6300, .1242, .1242
6	B	.8813, .3519, .1189	Al	.8754, .3678, .1246	Ga	.8759, .3672, .1241	In	.8758, .3700, .1242
7	B	.6109, .3887, .3887	Al	.6177, .3823, .3823	Ga	.6183, .3817, .3817	In	.6216, .3784, .3784
8	B	.8813, .1189, .3519	Al	.8754, .1246, .3678	Ga	.8759, .1241, .3672	In	.8758, .1242, .3700
9	B	.1187, .6483, .1187	Al	.1246, .6322, .1246	Ga	.1241, .6328, .1241	In	.1242, .6300, .1242
10	B	.3519, .8813, .1189	Al	.3678, .8754, .1246	Ga	.3672, .8759, .1241	In	.3700, .8758, .1242
11	B	.1189, .8813, .3519	Al	.1246, .8754, .3678	Ga	.1241, .8759, .3672	In	.1242, .8758, .3700
12	B	.3887, .6109, .3887	Al	.3823, .6177, .3823	Ga	.3817, .6183, .3817	In	.3784, .6216, .3784
13	B	.1187, .1187, .6483	Al	.1246, .1246, .6322	Ga	.1241, .1241, .6328	In	.1242, .1242, .6300
14	B	.3887, .3887, .6109	Al	.3823, .3823, .6177	Ga	.3817, .3817, .6183	In	.3784, .3784, .6216
15	B	.1189, .3519, .8813	Al	.1246, .3678, .8754	Ga	.1241, .3672, .8759	In	.1242, .3700, .8758
16	B	.3519, .1189, .8813	Al	.3678, .1246, .8754	Ga	.3672, .1241, .8759	In	.3700, .1242, .8758
17	B	1.000, 1.000, 1.000	Al	1.000, 1.000, 1.000	Ga	1.000, 1.000, 1.000	In	1.000, 1.000, 1.000
18	B	.0001, .5000, .5000	Al	.0000, .5000, .5000	Ga	1.000, .5000, .5000	In	1.000, .5000, .5000
19	B	.5000, .0001, .5000	Al	.5000, .0000, .5000	Ga	.5000, 1.000, .5000	In	.5000, 1.000, .5000
20	B	.5000, .5000, .0001	Al	.5000, .5000, .0000	Ga	.5000, .5000, 1.000	In	.5000, .5000, 1.000
21	B	.7467, .7467, .2533	Al	.7500, .7500, .2500	Ga	.7454, .7454, .2546	In	.7476, .7476, .2523
22	B	.7467, .2533, .7467	Al	.7500, .2500, .7500	Ga	.7454, .2546, .7454	In	.7476, .2523, .7476
23	B	.2533, .7467, .7467	Al	.2500, .7500, .7500	Ga	.2546, .7454, .7454	In	.2523, .7476, .7476
24	B	.2532, .2532, .2532	Al	.2500, .2500, .2500	Ga	.2546, .2546, .2546	In	.2523, .2523, .2523
25	N	.8674, .8674, .8674	N	.8655, .8655, .8655	N	.8648, .8648, .8648	N	.8644, .8644, .8644
26	N	.8674, .1326, .1326	N	.8655, .1345, .1345	N	.8648, .1352, .1352	N	.8644, .1356, .1356
27	N	.1326, .8674, .1326	N	.1345, .8655, .1345	N	.1352, .8648, .1352	N	.1356, .8644, .1356
28	N	.1326, .1326, .8674	N	.1345, .1345, .8655	N	.1352, .1352, .8648	N	.1356, .1356, .8644
29	N	.3795, .6204, .6204	N	.3783, .6217, .6217	N	.3808, .6192, .6192	N	.3816, .6184, .6184
30	N	.3795, .3795, .3795	N	.3783, .3783, .3783	N	.3808, .3808, .3808	N	.3816, .3816, .3816
31	N	.6204, .6204, .3795	N	.6217, .6217, .3783	N	.6192, .6192, .3808	N	.6184, .6184, .3816
32	N	.6204, .3795, .6204	N	.6217, .3783, .6217	N	.6192, .3808, .6192	N	.6184, .3816, .6184
33	O	.6256, .1169, .8832	O	.6117, .1174, .8826	O	.6114, .1183, .8817	O	.6101, .1170, .8830
34	O	.8832, .1169, .6256	O	.8826, .1174, .6117	O	.8817, .1183, .6114	O	.8830, .1170, .6101
35	O	.1169, .6256, .8832	O	.1174, .6117, .8826	O	.1183, .6114, .8817	O	.1170, .6101, .8830
36	O	.1169, .8832, .6256	O	.1174, .8826, .6117	O	.1183, .8817, .6114	O	.1170, .8830, .6101
37	O	.6256, .8832, .1169	O	.6117, .8826, .1174	O	.6114, .8817, .1183	O	.6101, .8830, .1170
38	O	.8832, .6256, .1169	O	.8826, .6117, .1174	O	.8817, .6114, .1183	O	.8830, .6101, .1170
39	O	.1168, .1168, .3743	O	.1174, .1174, .3883	O	.1183, .1183, .3886	O	.1170, .1170, .3899
40	O	.8832, .8832, .3745	O	.8826, .8826, .3883	O	.8817, .8817, .3886	O	.8830, .8830, .3899
41	O	.1168, .3743, .1168	O	.1174, .3883, .1174	O	.1183, .3886, .1183	O	.1170, .3899, .1170
42	O	.8832, .3745, .8832	O	.8826, .3883, .8826	O	.8817, .3886, .8817	O	.8830, .3899, .8830
43	O	.3743, .1168, .1168	O	.3883, .1174, .1174	O	.3886, .1183, .1183	O	.3899, .1170, .1170
44	O	.3745, .8832, .8832	O	.3883, .8826, .8826	O	.3886, .8817, .8817	O	.3899, .8830, .8830
45	O	.6304, .6304, .8787	O	.6326, .6326, .8732	O	.6322, .6322, .8727	O	.6337, .6337, .8701
46	O	.8787, .6304, .6304	O	.8732, .6326, .6326	O	.8727, .6322, .6322	O	.8701, .6337, .6337
47	O	.6304, .8787, .6304	O	.6326, .8732, .6326	O	.6322, .8727, .6322	O	.6337, .8701, .6337
48	O	.8788, .3696, .3696	O	.8732, .3674, .3674	O	.8727, .3678, .3678	O	.8701, .3663, .3663
49	O	.6304, .1215, .3696	O	.6326, .1268, .3674	O	.6322, .1273, .3678	O	.6337, .1298, .3663
50	O	.6304, .3696, .1215	O	.6326, .3674, .1268	O	.6322, .3678, .1273	O	.6337, .3663, .1298
51	O	.3696, .8788, .3696	O	.3674, .8732, .3674	O	.3678, .8727, .3678	O	.3663, .8701, .3663
52	O	.1215, .6304, .3696	O	.1268, .6326, .3674	O	.1273, .6322, .3678	O	.1298, .6337, .3663
53	O	.3696, .6304, .1215	O	.3674, .6326, .1268	O	.3678, .6322, .1273	O	.3663, .6337, .1298
54	O	.3696, .3696, .8788	O	.3674, .3674, .8732	O	.3678, .3678, .8727	O	.3663, .3663, .8701
55	O	.3696, .1215, .6304	O	.3674, .1268, .6326	O	.3678, .1273, .6322	O	.3663, .1298, .6337
56	O	.1215, .3696, .6304	O	.1268, .3674, .6326	O	.1273, .3678, .6322	O	.1298, .3663, .6337

Table 4.4: Cell structures of B_2O_3, Al_2O_3, Ga_2O_3, and In_2O_3.

Phase	Space group	Lattice (Å) LDA (GGA)	Expt (Å)
B_2O_3-I	$P3_1$	a = 4.295 (4.394)	a = 4.336[a]
		c = 8.075 (8.585)	c = 8.340[a]
B_2O_3-II	$Ccm2_1$	a = 4.582 (5.062)	a = 4.613[b]
		b = 7.780 (7.103)	b = 7.803[b]
		c = 4.102 (4.455)	c = 4.129[b]
α-Al_2O_3	$R\bar{3}c$	a = 4.733 (4.805)	a = 4.761[c]
		c = 12.908 (13.123)	c = 12.995[c]
θ-Al_2O_3	$C2/m$	a = 11.695 (11.911)	a = 11.80[d]
		b = 2.895 (2.938)	b = 2.910[d]
		c = 5.593 (5.669)	c = 5.621[d]
α-Ga_2O_3	$R\bar{3}c$	a = 4.978 (5.060)	a = 4.980[e]
		c = 13.351 (13.602)	c = 13.431[e]
β-Ga_2O_3	$C2/m$	a = 12.162 (12.445)	a = 12.230[f]
		b = 3.033 (3.083)	b = 3.040[f]
		c = 5.801 (5.876)	c = 5.80[f]
In_2O_3-I	$Ia3$	a = 10.027 (10.337)	a = 10.118[g]
In_2O_3-II	$R\bar{3}c$	a = 6.158 (6.687)	a = 5.478[h]
		c = 13.349 (13.068)	c = 14.51h[h]

[a][39], [b][40], [c][138], [d][50], [e][61], [f][134], [g][139], [h][69]

The constituent parent phases of the oxynitride spinel structure have been analyzed. The calculated optimized structures of group-III oxides (B_2O_3, Al_2O_3, Ga_2O_3, and In_2O_3) and nitrides (BN, AlN, GaN and InN) are given in Table 4.4 and 4.5. Both LDA and GGA results are in good agreement with the experimental results aside from the value of the c axis of w-InN, and this experimental value possibly needs further examination.

4.3 Elastic Properties

The elastic properties materials can be divided into two classes, the bulk modulus and the elastic constants or shear moduli. The bulk modulus is a function of energy and volume while the shear moduli requires knowledge of the derivative of the energy as a function of a lattice strain [141]. These properties are often used to measure the hardness of materials.

Table 4.5: Cell structures of BN, AlN, GaN and InN. a, b from REF. [140] and [75].

		Lattice (Å)	
Phase	Space group	LDA (GGA)	Expt (Å)
h-BN	$P6_3/mmc$	a = 2.481 (2.504)	a = 2.50399[a]
		c = 5.079 (5.045)	c = 6.6612[a]
c-BN	$P\bar{4}3m$	a = 3.746 (3.626)	a = 3.615[a]
w-AlN	$P6_3mc$	a = 3.091 (3.128)	a = 3.111[a]
		c = 4.945 (5.012)	c = 4.978[a]
c-AlN	$F\bar{4}3m$	a = 4.346 (4.400)	a = 4.380[b]
w-GaN	$P6_3mc$	a = 3.184 (3.211)	a = 3.180[a]
		c = 5.178 (5.231)	c = 5.166[a]
c-GaN	$F\bar{4}3m$	a = 4.499 (4.538)	a = 4.50[b]
w-InN	$P6_3mc$	a = 3.505 (3.585)	a = 3.540[b]
		c = 5.668 (5.787)	c = 5.700[b]
c-InN	$F\bar{4}3m$	a = 4.941 (5.046)	a = 4.980[b]

4.3.1 The Equation of State Bulk Modulus

The equation of state is a pressure-volume or energy-volume relation describing the behavior of a solid under compression and expansion at zero absolute temperature. It is valuable not only for the prediction of the fundamental thermodynamical parameters but also to obtain insight into the nature of the solid state. Bulk modulus of a material measures its resistance to volume reduction under compression. The upper limit of bulk modulus of a material often reflects the intrinsic compressive hardness of the crystal structure. The equilibrium bulk modulus at temperature, T $= 0$, and minimum volume V_0 is defined as:

$$B_0 = -V_0\left(\frac{\partial P}{\partial V}\right)$$

or

$$B_0 = V_0\left(\frac{\partial^2 E}{\partial V^2}\right) \tag{4.1}$$

where P is the applied pressure and E is the internal energy. A calculation of bulk

modulus should allow the unit cell and its contents to move freely at fixed temperature and pressure. This should be performed over a range of pressures or total energies and the bulk modulus extracted from the resulting equilibrium volumes. This is done for a set of volumes obtained after full relaxation of the unit cell for an isotropic strain, and the energy-volume curve are fitted to an isothermal equation of state. The assumption used for most of the equations of state for solids is that near the equilibrium, the bulk modulus varies linearly with pressure:

$$B = B_0 + B_0' P \tag{4.2}$$

from which some are constructed to describe specific crystal structures or materials. The equation of state we used in this study are:

$$E_M(V) = \frac{V_0 B_0}{B_0'(B_0' - 1)} \left[B_0'(1 - \rho^3) + \rho^{3B_0'} - 1 \right] + E_0 \tag{4.3}$$

$$E_B(V) = \frac{9}{16} B_0 V_0 (\rho^2 - 1)^2 \left[B_0'(\rho^2 - 1) - 4\rho^2 + 6 \right] + E_0 \tag{4.4}$$

$$E_V(V) = \frac{V_0 B_0}{(B_0' - 1)^2} \left[4 + \left(6B_0' - 6B_0'\rho^{-1} + 6\rho^{-1} - 10 \right) e^{\frac{3}{2}(B_0' - 1)(1 - \rho^{-1})} \right] + E_0 \tag{4.5}$$

where $\rho = (V_0/V)^{1/3}$ and the fitting parameters B_0, B_0', V_0 and E_0 represents the bulk modulus, pressure derivative of the bulk modulus, equilibrium volume and zero-pressure energy respectively. Equations 4.3, 4.4 and 4.5 are known as the Murnaghan [142], Birch [143, 144] and the Universal equation of state [145, 146, 147] respectively. Of these 3 equations, the Birch equation of state is the most widely used and is known to be extremely successful in matching finite-compression data [148, 149]. The Birch equation of state along side with both the Murnaghan and Universal equations of state were used to fit the

energy-volume points of isotropically scaled unit cells. The main assumption is that no phase transition occurs during the compression of the material. The fitting parameters obtained for all the spinel structure are listed in Table 4.6.

Table 4.6: LDA and GGA (in bracket) calculated bulk modulus, pressure derivative, equilibrium volume and the zero-pressure energy of the spinel structures. The parameters were obtained from fitting to the Murnaghan, Birch and Universal equation of states.

Parameters	B_3NO_3	Al_3NO_3	Ga_3NO_3	In_3NO_3
B_0(GPa)(M)	337.5 (291.9)	232.0 (207.5)	230.9 (176.6)	162.8 (144.8)
B_0(GPa)(B)	339.7 (294.1)	233.2 (208.6)	232.3 (177.7)	163.2 (145.7)
B_0(GPa)(V)	339.7 (294.1)	233.2 (208.6)	232.3 (177.7)	163.2 (145.7)
B_0'	4.64 (4.96)	4.07 (4.10)	4.75 (4.55)	4.58 (5.04)
V_0 ($Å^3$)	38.61 (40.51)	60.32 (63.16)	68.92 (72.21)	89.00 (98.26)
E_0 (eV/atom)	-8.399 (-7.382)	-8.211 (-7.399)	-6.854 (-5.987)	-6.365 (-5.456)

[a]Ref. [150]B_0(GPa)Al_3NO_3 = 234 (203)
[b]Ref. [136]B_0(GPa)Ga_3NO_3 = (210)

From Table 4.6, the Murnaghan bulk modulus is generally low as compared to the Birch and Universal equation of states which for shows the same values for the bulk modulus. The bulk modulus of B_3NO_3 which is 339.7 GPa is higher than the rest of the spinels, and as one move down the B to In, it graudually decrease. We should note that the GGA tends to underestimate the bulk modulus of solids with respect to the LDA [151]. Comparing Table 4.1 with Table 4.6, there is a clear relationship between the lattice constants and bulk modulus of the spinels. A larger lattice constant leads to a smaller bulk modulus. This trend can be understood by the chemical idea of the inter-atomic distance, which means that the compressibility decreases as the inter-atomic distance decreases. The trend in the bulk modulus for the spinel structures and binary nitrides is shown in Fig. 4.2

The result also shows that spinel structure could be potential hard materials in closed comparison with diamond and the cubic boron nitride except for spinel In_3NO_3 which has a very low bulk modulus of 163.2 (145.7). The calculated bulk pressure derivatives, B_0', of each compound falls within the range 3-5 as it is the case of most solids. In Table 4.7 and 4.8, we estimates the LDA and GGA values of Zero-pressure energy, equilibrium volume,

Table 4.7: LDA and GGA estimated values of Zero-pressure energy, equilibrium volume, pressure derivative and the bulk moduli of the ambient phases of the various materials. The GGA results are in brackets.. [a, b, c]from REF. [152], [153], and [70] respectively.

Material	E_0 (eV/atom)	V_0 (Å^3)	B_0'	B_0 (GPa)	B_0(GPa) Other Calc.
B_2O_3-I	-8.439 (-7.456)	39.90 (41.25)	4.02 (12.4)	322 (299)	
B_2O_3-II	-8.925 (-7.720)	49.45 (53.77)	1.72 (3.97)	177 (182)	
$\alpha - Al_2O_3$	-8.312 (-7.480)	56.39 (59.13)	4.07 (4.07)	258 (230)	258[a]
$\theta - Al_2O_3$	-8.262 (-7.471)	62.08 (65.19)	3.74 (3.81)	206 (185)	199[a]
$\alpha - Ga_2O_3$	-6.904 (-6.004)	64.69 (68.01)	4.79 (4.53)	262 (198)	250[b]
$\beta - Ga_2O_3$	-6.866 (-6.035)	70.61 (74.07)	3.85 (4.01)	192 (155)	202[b]
In_2O_3-I	-6.512 (-5.607)	85.13 (93.57)	4.15 (5.11)	172 (156)	172[c]
In_2O_3-II	-6.3660 (-5.48)	90.47 (97.00)	3.02 (4.45)	123 (98)	183[c]

pressure derivatives and the bulk moduli of the ambient phases for group-III oxides (B_2O_3, Al_2O_3, Ga_2O_3, and In_2O_3) and nitrides (BN, AlN, GaN and InN) materials. Both LDA and GGA results are in good agreement with the experimental results (See REf. [152], [153], [70], and [73]).

Table 4.8: LDA and GGA estimated values of Zero-pressure energy, equilibrium volume, pressure derivative and the bulk moduli of the ambient phases of the group-III nitride materials. The GGA results are in brackets.[a]from REF. [73]

Material	E_0 (eV/atom)	V_0 (Å^3)	B_0'	B_0 (GPa)	B_0(GPa) Other Calc.
h-BN	-9.547 (-8.588)	47.40 (48.48)	3.62 (3.52)	321 (310)	397[a]
c-BN	-9.715 (-8.710)	38.79 (31.66)	3.66 (3.74)	400 (373)	400[a]
w-AlN	-8.213 (-7.445)	69.13 (71.79)	4.37 (4.32)	205 (191)	202[a]
c-AlN	-8.190 (-7.423)	69.30 (71.94)	3.95 (3.87)	210 (193)	203[a]
w-GaN	-6.973 (-6.157)	76.98 (79.23)	5.90 (4.49)	210 (170)	207[a]
c-GaN	-6.965 (-6.152)	77.02 (79.28)	4.56 (4.48)	212 (170)	201[a]
w-InN	-6.176 (-5.446)	101.86 (108.46)	5.70 (6.57)	135 (121)	146[a]
c-InN	-6.175 (-5.434)	101.26 (103.10)	7.06 (3.25)	163 (132)	139[a]

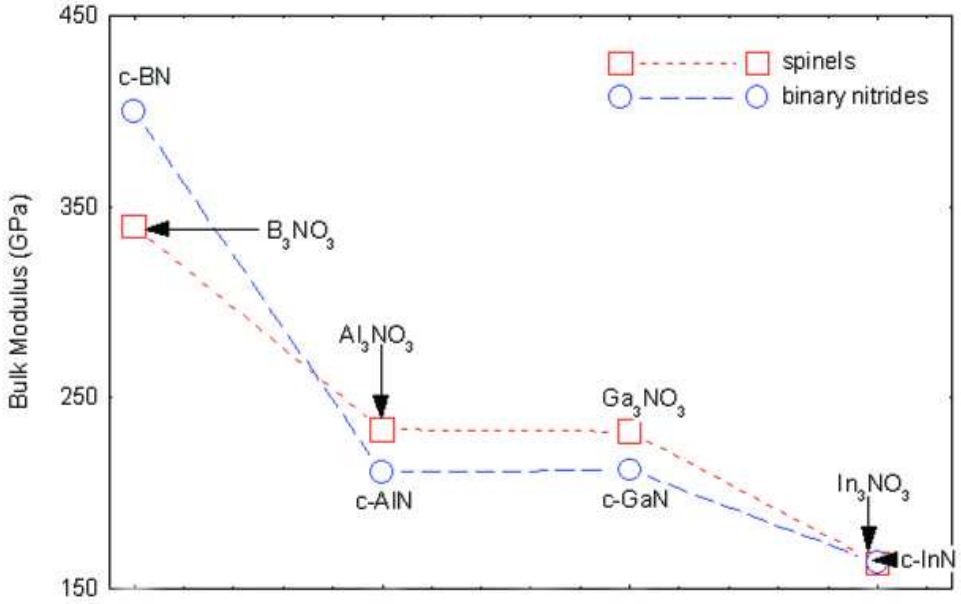


Figure 4.2: Trend in the LDA equation of state derived bulk modulus of spinels and cubic binary nitrides.

4.3.2 Estimation of the Elastic Constants

Using the *ab-initio* approach it is possible to obtain all the elastic constants by an aplication of an appropriate deformation of the unit cell and, thereafter, some estimate of the appropriate effective isotropic moduli. The elastic constants determine the response of the crystal to an externally applied strain (stiffness) or, the stress required to maintain a given deformation. It also provide information about the bonding characteristics between adjacent atomic planes, anisotropic character of the bonding, and structural stability. For small deformations we expect a quadratic dependence of the crystal energy, E, on the strain (Hooke's law). To obtain the total minimum energy for calculating the elastic constants to second order, a crystal is strained and all internal degrees of freedom relaxed according to the rule:

$$\mathrm{R}' = \mathrm{R}(\mathrm{I} + \varepsilon) \tag{4.6}$$

where R' and R are the matrices that contain the components of the strained and unstrained lattice vectors, I is the 3×3 identity matrix, and ε is a symmetric 3×3 non-rotating strain tensor with six independent components:

$$\varepsilon_{ij} = \begin{pmatrix} e_1 & e_6/2 & e_2/2 \\ e_6/2 & e_2 & e_4/2 \\ e_5/2 & e_4/2 & e_3 \end{pmatrix} \tag{4.7}$$

The changes in total energy due to the above strain [Eqn. 4.7] is:

$$\begin{aligned} \frac{\Delta E}{V_0} &\equiv \frac{E(\{e_i\}) - E_0}{V_0} \\ &= \left(1 - \frac{V}{V_0}\right) P(V_0) + \frac{1}{2}\left(\sum_{i=1}^{6}\sum_{j=1}^{6} C_{ij} e_i e_j\right) + O(\{e_i^3\}) \end{aligned} \tag{4.8}$$

where V_0 is the volume of the unstrained lattice, E_0 is the total minimum energy at this unstrained volume of the crystal, $P(V0)$ is the pressure of the unstrained lattice, V is the new volume of the lattice due to strain in Eqn. 4.7 and $O(\{e_i^3\})$ indicates that the neglected terms in the polynomial expansion are cubic and higher powers of the e_i.

There are 21 independent elastic constants C_{ij} from Eqn. 4.8. Symmetry reduces this number to three for the cubic systems, 6 for tetragonal and 9 for for orthorhombic systems. The 3 independent elastic constants for a cubic system such as the spinel structures are C_{11}, C_{12} and C_{44} with each representing three equal elastic constants ($C_{11} = C_{22} = C_{33}$, $C_{12} = C_{23} = C_{31}$, $C_{44} = C_{55} = C_{66}$). A full account of the symmetry of crystals and their elastic constants is given by Nye [154].

Table 4.9: Parametrization of the three strains used in calculating the three elastic constants of the cubic spinel structures. The energy expressions were obtained from Eqn. 4.8. Strains 1 is equivalent to simple hydrostatic pressure while strains 2 and 3 are strictly volume conserving to all orders in the strain parameter δ.

Strain	Parameters	$\Delta E/V$
1	$e_1 = e_2 = e_3 = \delta$	$\frac{3}{2}(c_{11} + 2c_{12})\delta^2$
2	$e_1 = e_2 = \delta$, $e_3 = \{1/(1+\delta)^2 - 1\}$	$3(c_{11} - c_{12})\delta^2$
3	$e_3 = \delta^2/(4 - \delta^2)$, $e_6 = \delta$	$\frac{1}{2}c_{44}\delta^2$

The set of strains $\{e_i, i = 1, 2, ..., 6\}$, in Eqn. leads to a parabolic relationship between $\Delta E/V_0$ ($\Delta E \equiv E - E_0$) and the strain. The parameterizations of these strains and their corresponding form for ΔE of the cubic spinel structures are given in Table 6.1. These energies and strains were fit with the corresponding parabolic equations of $\Delta E/V_0$ as given in Table 6.1 to yield the required second order elastic constants. While computing these energies all atoms are allowed to relax with the cell shape and volume fixed by the set of strains $\{e_i\}$.

The elastic constants for the cubic spinel structure are determined by applying the strains listed in Table 6.1. From these we can deduce the harmonic values of the Bulk modulus B and effective Voigt shear G using the well known expressions:

$$B = \frac{1}{3}(c_{11} + 2c_{12}) \tag{4.9}$$

$$G = \frac{1}{5}(c_{11} - c_{12} + 3c_{44}) \tag{4.10}$$

Table 4.10: Calculated elastic constants and effective (Voigt) isotropic elastic modulii for Spinel Oxynitrides. Experimental values for diamond are B=442-433, G=524-544, E=1142-1164, ν=0.1. For spinel Si_3N_4 B=308 and G=258. All modulii are in GPa. A low (high) value of B/G may be indicative of the material to be brittle (ductile). The smaller value of ν may indicate the resistance of the material to shear.

		c_{11}	c_{12}	c_{44}	B	G	B/G	E	ν
LDA	B_3NO_3	140	381	411	301	198	1.52	488	0.23
	Al_3NO_3	344	179	184	234	143	1.64	357	0.25
	Ga_3NO_3	316	202	131	240	101	2.38	266	0.32
	In_3NO_3	212	136	76	161	61	2.64	162	0.33
GGA	B_3NO_3	72	414	361	300	148	2.03	381	0.40
	Al_3NO_3	310	160	175	210	135	1.56	333	0.24
	Ga_3NO_3	249	146	124	180	95	1.89	242	0.28
	In_3NO_3	202	138	65	159	52	3.06	140	0.35

The bulk and the shear modulus can be used to obtain an effective Young's modulus E and the Poisson ratio ν using the following expressions:

$$E = \frac{9BG}{3B + G} \tag{4.11}$$

$$\nu = \frac{(3B - 2G)}{2(3B + G)} \tag{4.12}$$

The isotropic Poisson ratio is considered as being a measurement of the material to resist shear. The smaller the value the more likely the material will resist shear. The necessary conditions for a mechanical stability of a cubic crystal structures are given by [155]:

$$(c_{11} - c_{12}) > 0, c_{11} > 0, c_{44} > 0, (c_{11} + 2c_{12}) > 0 \tag{4.13}$$

The values of the elastic constants are shown in Table 6.5 together with the effective isotropic values. As with the equation of state Bulk modulus, a steady increase in the bulk and shear modulus is clearly apparent for In_3NO_3 to B_3NO_3. The cubic structure of Al_3NO_3, Ga_3NO_3 and In_3NO_3 satisfies all the stability conditions of Eqn. 4.13. However, a tetragonal elastic instability of B_3NO_3 is found when the value of $(c_{11}-c_{12})$ was calculated. This rather surprising result was checked both for magnitude of calculational displacement in the appropriate distortion of $(c_{11} - c_{12})$ as well as usual convergence criterion. It would thus appear that whilst being a highly compressible structure, B_3NO_3 is unstable against tetrahedral displacement. It is unlikely that the stability is associated with strong covalent bonding interactions between the B-N and the B-O structures that are evident in the tetragonal direction of the spinel unit cell of B_3NO_3. Apart from the material hardness that is known to be generally related to compressibility, as measured by the bulk modulus and to a shear modulus, a further estimate of the physical behavior of material has been introduced by Pugh [155] where he suggested that the ratio of B/G is related to the brittleness of the material with lower values suggesting that the material is more brittle. According to Pugh, when $B/G < 1.75$ the material has a ductile features and when $B/G > 1.75$ the material shows brittle character.

4.4 Electronic Structure

4.4.1 Electronic Density of States (DOS) and Band Structure

The density of states, band structures and their *k*-space integrals are the common tools for the electronic structure visualization and characterization of quantum systems. These analysis provide very useful information about the distribution of the states in *k*-space and energy. The physical understanding of different characteristic properties of a material can be traced to understanding their electronic states. For example, band gap have been used as an indicator for mechanical hardness and more importantly they can also stabilize a crys-

tal in a particular structure. The identification of Kohn-Sham eigenvalues with electronic states is often problematic, however, the unoccupied Kohn-Sham states are used to compare band structures and, in most cases, band gaps with experiment. The LDA predicted band structure plots are show in Fig. 4.3 to 4.6. The x-axis in the band structure plots represents the special high symmetry points in the reciprocal space between which the bands have been chosen to be plotted. The energy band structure for Ga_3NO_3 and In_3NO_3 has been discussed earlier [134, 137] and also in our recent paper [156]. Both these materials have direct energy gaps in the 56-atom unit cell and thus have potentially important optoelectronic properties. B_3NO_3 and Al_3NO_3 oxynitrides, on the other hand, also have a direct gap at the Γ of the cubic unit cell. Notably for all the spinel oxynitrides, the upper levels of the valence bands are relatively flat- this is characteristic features of all spinel structures [22]. However, there is a significant *K* dispersion in the conduction bands.

We have also called the density of states (DOS) for these oxynitride materials. The DOS are related to the band structure:

$$d(E) = \int_{BZ} \delta(E - E(\mathrm{K}))d\mathrm{K} \tag{4.14}$$

The calculated densities of states of each of the spinels structure are displayed in Fig. 4.3 to 4.6 along side with their respective band structure plots. In the DOS-plots the x-axis is energy and the y-axis is the number of the eigenvalues (states) at a particular energy level, whereby the energy distribution are measured relative to their Fermi energy. The Fermi energy level is indicated by a vertical dotted line. The energy scale is chosen so that the Fermi energy level is located at 0 eV. There is an overall resemblance of the density of states for the spinels with more populated electron density in their valence band (VB) than as compared to their conduction band (CB). The conduction bands as we move from B_3NO_3 to In_3NO_3 are shifted towards lower energies. In the vicinity of the Fermi level, the DOS are substantially similar since they all reflect *M*-N-O bonding, where *M* represents

B, Al, Ga and In. The DOS can be projected into its partial components or partial DOS (PDOS) with respect to the different atoms to explain how the spinel atoms are bonded together, however, we do not wish to go into great detail of the spinel bonding mechanism.

The calculated energy band gaps are summarized in Table 4.11 where comparison is also made with the energy band gap of deduced for the binary zinc-blende nitride structures. We recall that both LDA and GGA calculations generally underestimates the band gaps of materials. This underestimation is apparently due to the approximate nature of DFT functionals so actual band gaps of the spinel should be larger than the calculated values given in Table 4.11. Comparing the spinels with their respective cubic binary nitrides as it relates with their lattice constants and band gaps, a characteristic trend similar to both material can be observed as shown in Fig. 4.7. The trend shows that a decreasing band gaps corresponds with an increase in lattice constants for both material.

Table 4.11: Calculated band gaps of the spinels and their respective cubic binary nitrides.

	Band gap (eV)			Band gap (eV)		
Spinel	LDA	GGA	Nitride	LDA	GGA	Expt. (eV)[a]
B_3NO_3	4.60	4.43	c-BN	4.47	4.40	6.1 - 6.4[a]
Al_3NO_3	4.02	3.70	c-AlN	3.10	3.09	4.5 - 6.2[a]
Ga_3NO_3	1.72	1.37	c-GaN	1.97	2.43	3.30[a]
In_3NO_3	0.40	0.40	c-InN	0	0	0.6 - 0.7[b]

[a]Ref. [75], [b]Ref. [157]

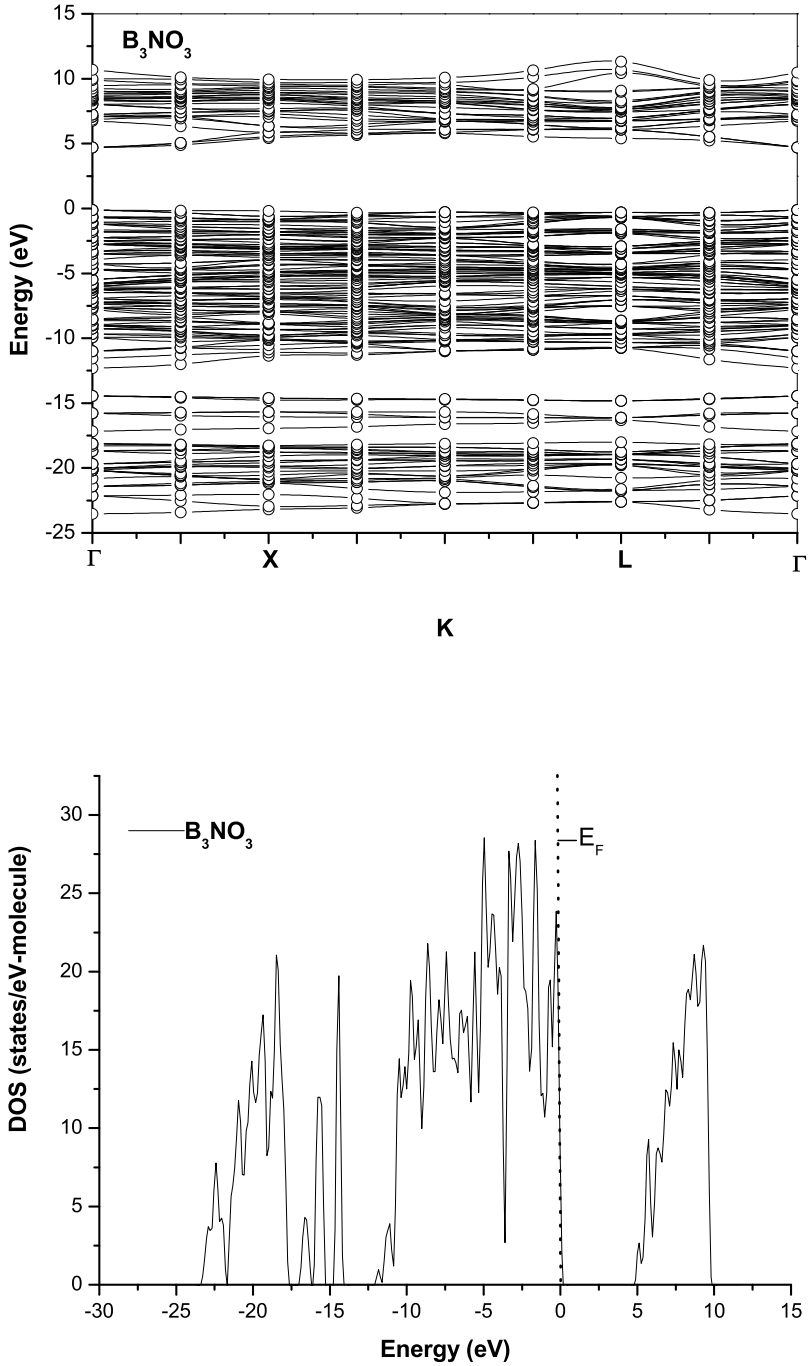


Figure 4.3: Calculated LDA energy band structure and density of states of B_3NO_3. The Fermi energy level is at zero energy.

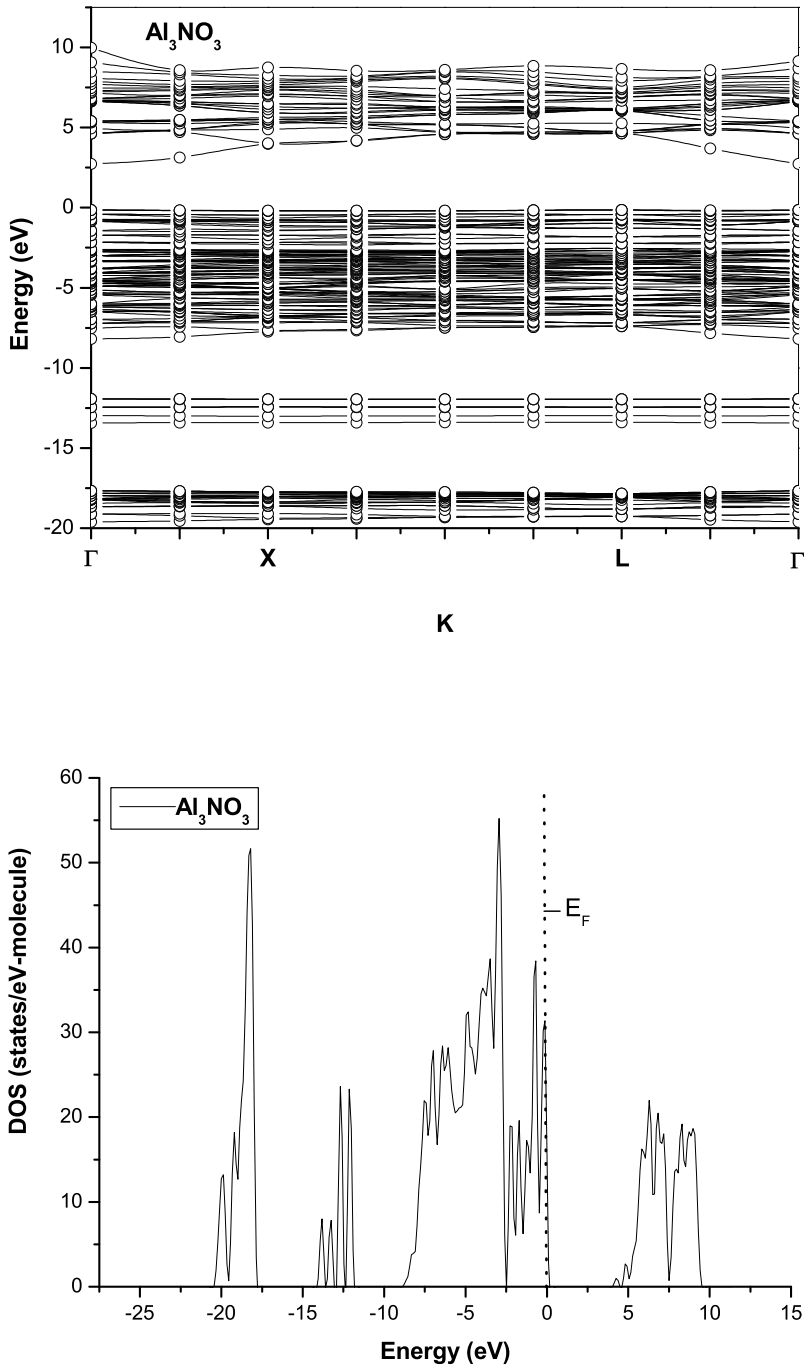


Figure 4.4: Calculated LDA energy band structure and density of states of Al_3NO_3. The Fermi energy level is at zero energy.

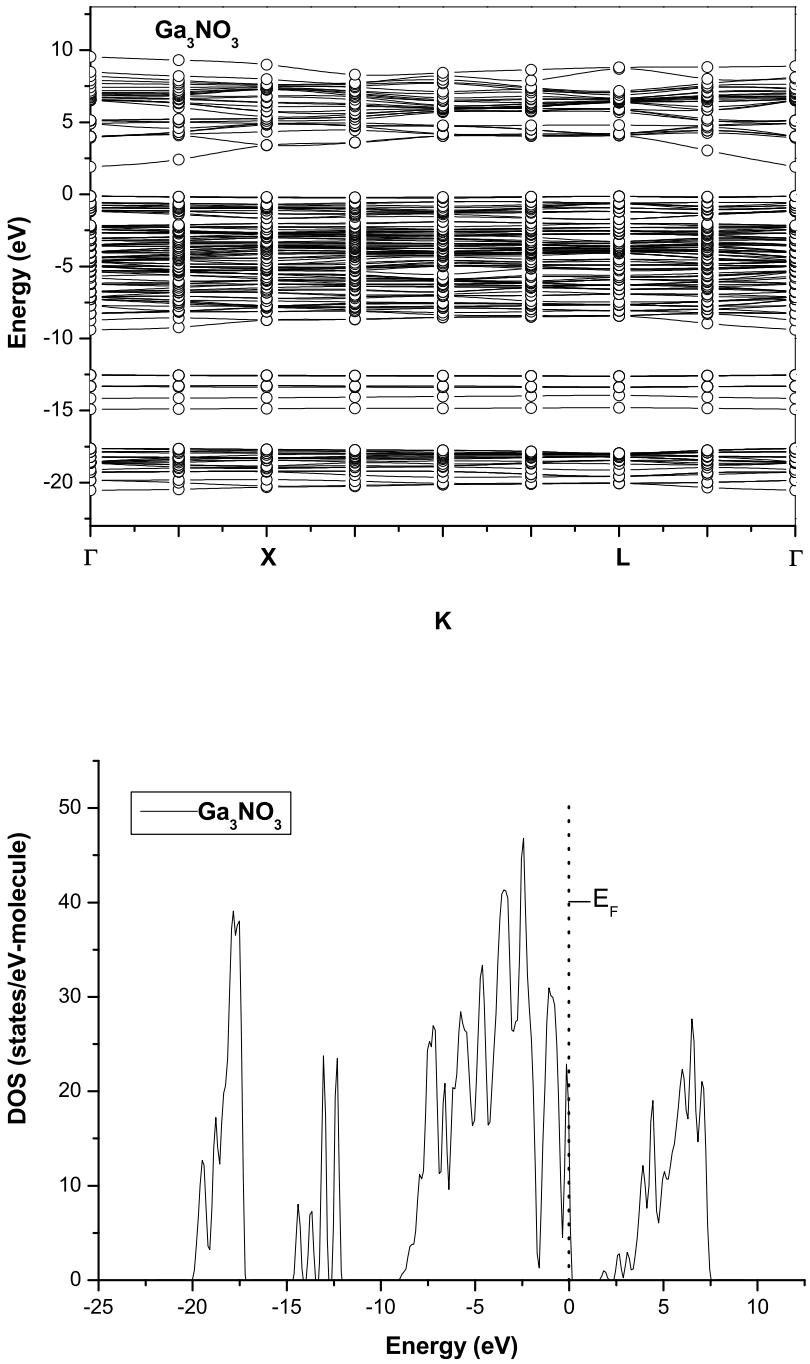


Figure 4.5: Calculated LDA energy band structure and density of states of Ga_3NO_3. The Fermi energy level is at zero energy.

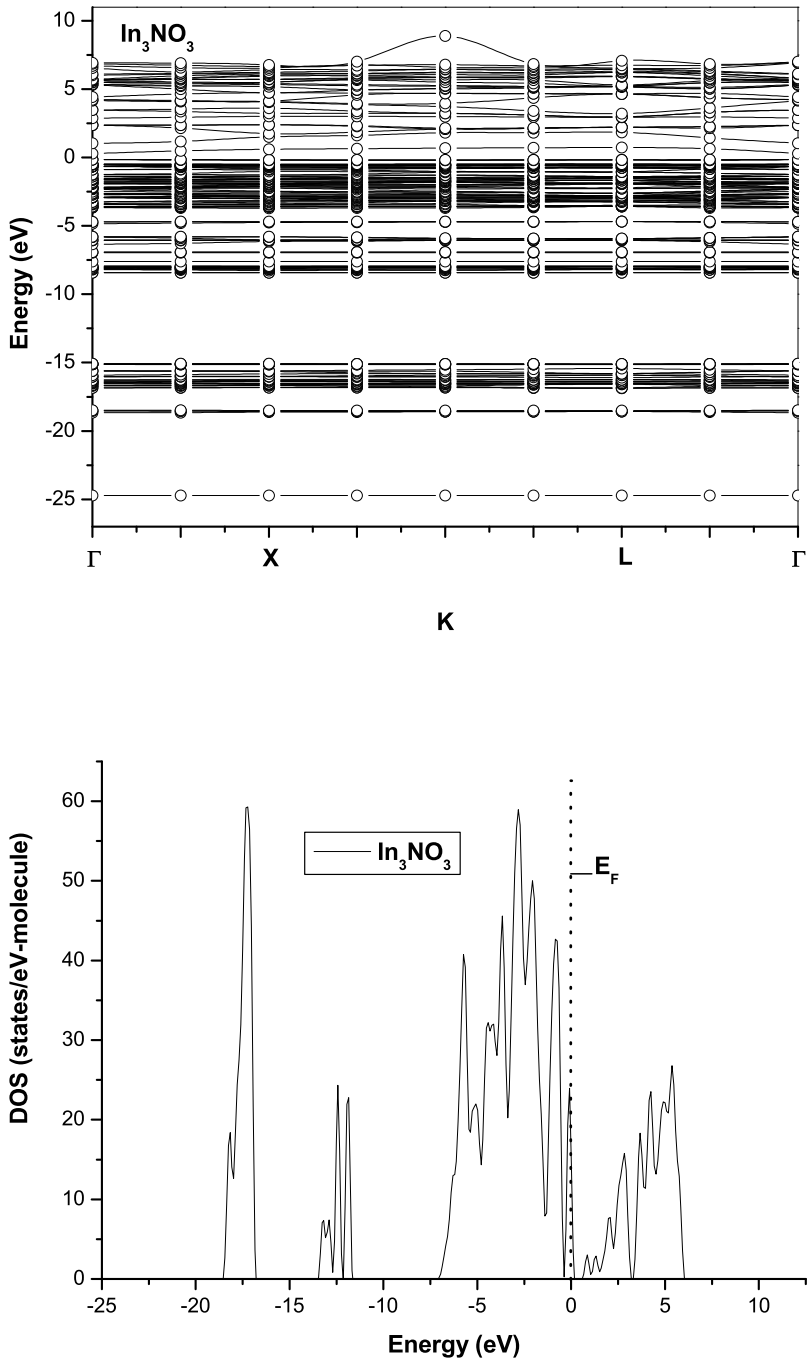


Figure 4.6: Calculated LDA energy band structure and density of states of In_3NO_3. The Fermi energy level is at zero energy.

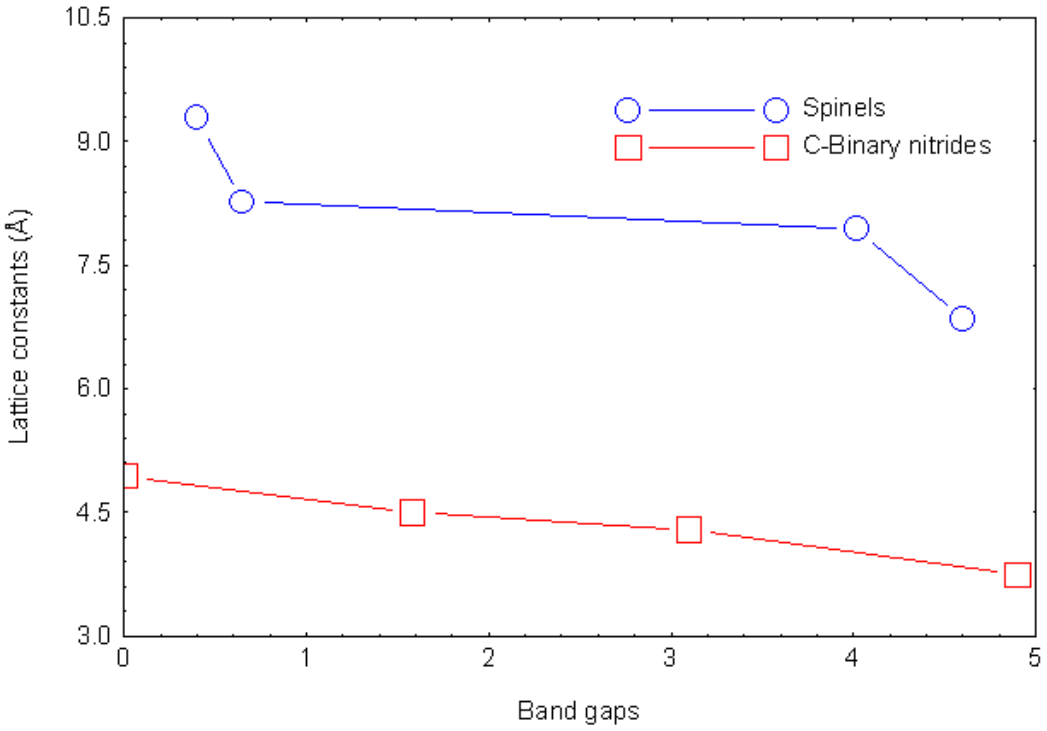
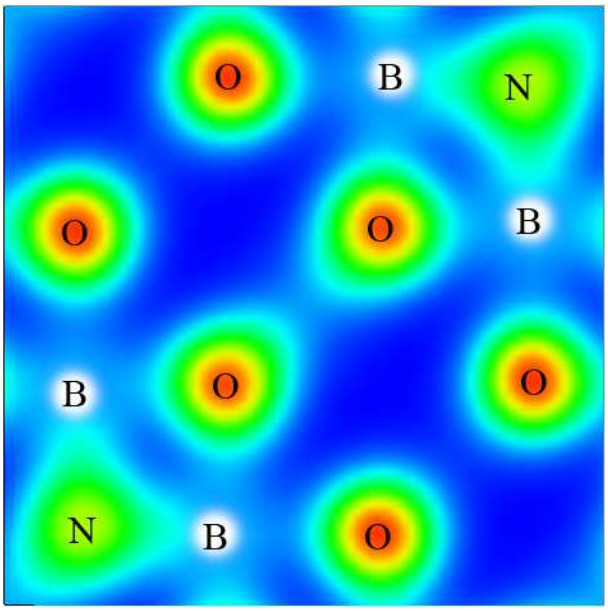


Figure 4.7: Trends relating the band gaps with the lattice constants computed from the LDA results.

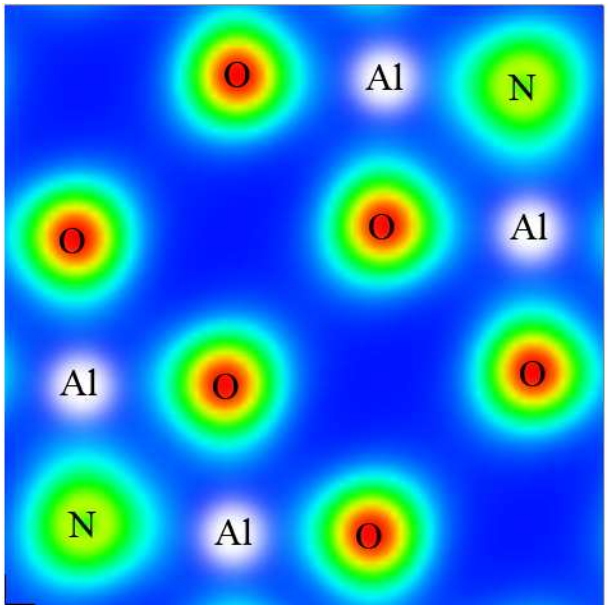
4.4.2 Electronic Charge Density

Since the fundamental entity in density functional theory (DFT) is the charge density, DFT also allow us to display the distribution of the electrons around the constituent atoms in the solid or material. Charge density can be used to understand features of the electronic properties in a material, for example differences in bonding between different structures of the same compounds, changes in bonding between compounds and the charge transfer or ionicity

The calculated charge density distribution in the 001 plane of the spinel structures are displayed along the A-O-N bonds (where A represents B, Al, Ga, O) in Fig. 4.8 and 4.9. The covalent bonding steadily increases from B to In, especially with N. We have seen earlier that the incompressibility and shear constants increases from the In_3NO_3 to B_3NO_3 spinel. The reason for this is directly attributed to the reduction in covalent bonding from B_3NO_3 to In_3NO_3. This is clearly seen in Figure 4.8 and 4.9. In the case of B_3NO_3 we notice that B is preferentially bonded to N although at the same time there appears some evidence of formation of a O-O bond. The A atoms (regions in light blue) are connected by the O and N atoms (region in red and yellow respectively).

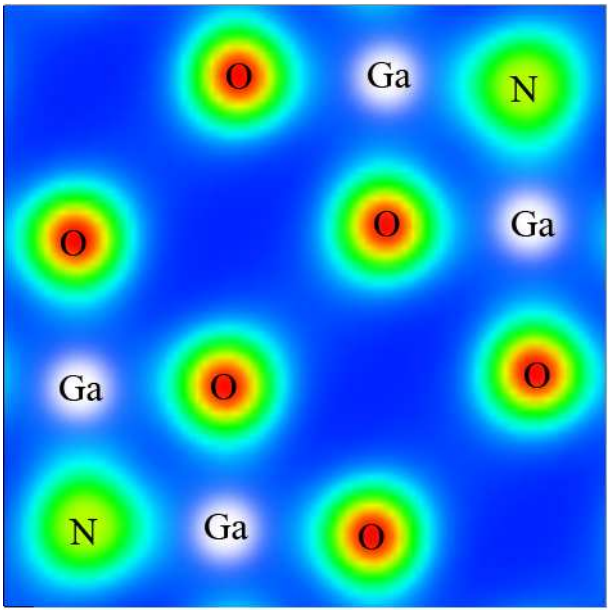


(a) B_3NO_3 Spinel.

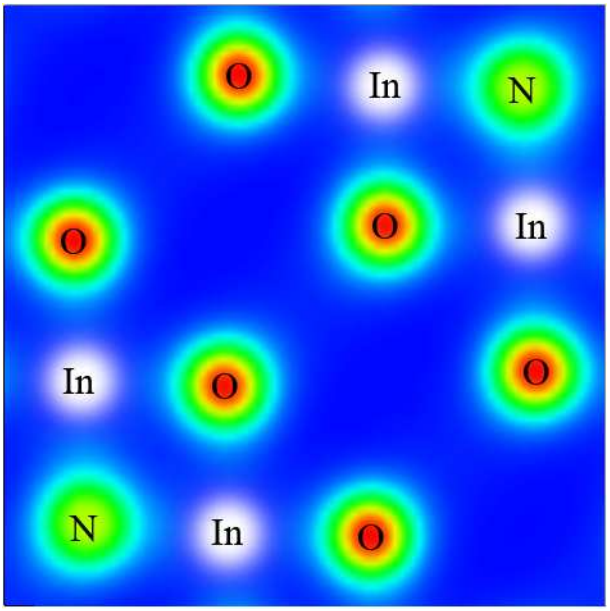


(b) Al_3NO_3 Spinel.

Figure 4.8: Calculated charge density distribution of B_3NO_3 and Al_3NO_3 in the (001) plane. The charge density is calculated from the LDA results. High charge density is colored red.



(a) Ga_3NO_3 Spinel.



(b) In_3NO_3 Spinel.

Figure 4.9: Calculated charge density distribution of Ga_3NO_3 and In_3NO_3 in the (001) plane. The charge density is calculated from the LDA results. High charge density is colored red.

4.5 Relative Stability of Spinel

The relative stability of the spinels, A_3NO_3, have been estimated with respect to the simple mixture of each of its constituent phases. A measure of the relative stability of the spinel is defined by Eqn. 4.15 without any application of extreme conditions such as pressure or temperature:

$$\Delta E_{stab} = E_{tot}[\mathrm{M_3NO_3}] - E_{tot}[\mathrm{MN}] - E_{tot}[\mathrm{M_2O_3}] \tag{4.15}$$

where M represents B, Al, Ga, and In. In the above equation E_{tot} is the total energy at the optimized geometry and corresponds to the free energy of the compound at zero temperature and zero pressure. ΔE_{stab} represents the estimation of the relative stability of the spinels, M_3NO_3. A spinel with positive value of ΔE_{stab} is likely to be metastable under ambient conditions i.e. zero pressure and temperature whereas a negative value of ΔE_{stab} suggests that the spinel phase would be stable.

In Table 4.12 we give the calculated values for each of the family of oxide and nitride structures considered here. At this stage it is to be noted that these values will have some degree of calculated uncertainty - conservatively estimated to be about 0.05 eV/atom. However it is noted that there is a variation depending upon the component phases. The stable state of the spinel could be observed in In_3NO_3 with a possible mixture of In_2O_3-I and any of the polymorph of the indium nitride (InN). The trend in the relative stability is shown in Figure 4.10 for the lowest energy components indicated in Table 4.12.

Table 4.12: ΔE_{stab} values for LDA and GGA (in brackets). *denotes the lowest value of ΔE_{stab} for the phases indicated. The values in column 3 and 4 in each section of the table shows the ΔE_{stab} of the spinels calculated from the total energies of the spinel (column 1), the oxide phases (column 2) and the nitride phases (row 1) respectively using Eqn. 4.15.

spinel	oxide	nitride	
		h-BN	c-BN
	B_2O_3-I	3.086 (2.851)	0.405* (0.434)*
B_3NO_3			
	B_2O_3-II	3.433 (3.039)	0.753 (0.622)
		w-AlN	c-AlN
	$\alpha - Al_2O_3$	0.053 (0.060)	0.067 (0.065)
Al_3NO_3			
	$\theta - Al_2O_3$	0.017* (0.053)*	0.031 (0.059)
		w-GaN	c-GaN
	$\alpha - Ga_2O_3$	0.046 (0.062)*	0.068 (0.062)
Ga_3NO_3			
	$\beta - Ga_2O_3$	0.019* (0.083)	0.041 (0.083)
		w-InN	c-InN
	In_2O_3-I	-0.054 (0.022)	-0.054* (0.018)*
In_3NO_3			
	In_2O_3-II	0.052 (0.106)	0.051 (0.103)

4.6 Conclusions

We have presented an extensive investigation of a novel spinel cubic phase of the form M_3NO_3 (where *M*=B, Al, Ga or In) with a nominal symmetry of $P\bar{4}3m$ (No. 215). To dates only Ga_3NO_3 has been synthesized (See REF [136, 137]) and we now suggest that at least three other forms of the material should receive attention for use as a possible material. Our theoretical study showed that there is a definite trend in going from B_3NO_3 to In_3NO_3 especially in the bulk modulus, shear constants, band gaps and charge densities as compared with their lattice constants. However, in addition, there is a variation in the elastic constants of the spinels. While being fairly increasing in going from In_3NO_3 to Al_3NO_3, there is an abrupt reduction in the B_3NO_3 spinel structure. The latter effect is being attributed to a tetragonal elastic instability possibly due to the asymmetric nature of

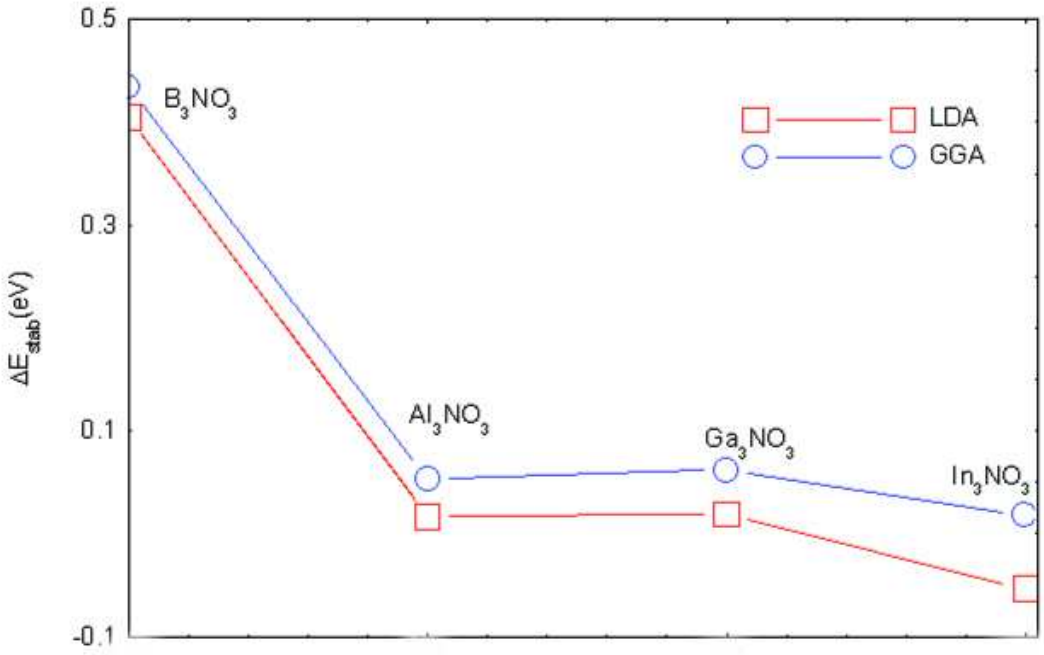


Figure 4.10: Relative stability of M_3NO_3 spinel as compared with lowest energy ambient phases of M_2O_3 and MN structures as indicated in Table (4.12).

B-O and B-N strong bonding in the B_3NO_3 spinel unit cell. All the results imply that spinels considered in this work are quite incompressible structures, and based on the calculated values of the shear constants, Al_3NO_3 could be a new hard material with possible novel applications.

The energy band gaps of the oxynitride spinels M_3NO_3 decreases systematically as M is changed from B to In. As with GaN and InN, the possibility that such an oxynitride spinel structures in the form of M_3NO_3 could have interesting applications as a new optoelectronic material should be considered.

Chapter 5

Molecular Dynamics Simulations

In practice a systematic study of the relationship between composition and the properties of a *M*-N-O oxynitride spinel material (where *M*=B, Al, Ga, In) could be very difficult because of the very high temperatures and pressures involved in their synthesis. Computer simulation techniques are a powerful means of investigating materials where extreme conditions are concerned [158]. Computer simulation provides a direct route from the microscopic details of a system to macroscopic properties of experimental interest in the hope of understanding the properties of system in terms of their structure and interactions between them. Classical molecular-scale computer simulation sometimes referred to as computer experiment involves a three step procedure: (a) model individual particle of the system, (b) simulate the movements of a large number of the model particles, and (c) analyze the simulation data for required collective phenomenon [159]. These techniques involve a model as specified in terms of molecular structure and intermolecular interactions. Result from computer simulations are then compared with predictions and experimental data [160].

There are two main types of techniques used in the computer simulations, namely: Molecular Dynamics (MD) and Monte Carlo (MC) methods. MD and MC methods are both based on a molecular description of the system of interest; the main ingredient in each case is the law that description of the interactions between the constituent particles or atoms

of the system.

The Monte Carlo method is a stochastic technique where sampling can be biased towards regions of specific interest. It is defined by representing the solution of a problem as a parameter of a hypothetical population, and using a random sequence of numbers to construct a sample of the population, from which statistical estimates of the parameter can be obtained [161]. MC simulations are not constrained by natural timescale and can often handle fluctuating numbers of particles in configuration space. There is no true dynamical information with this method and are therefore used to study static or equilibrium properties of model systems.

Molecular dynamics (MD) merges computer simulation with statistical mechanics to compute equilibrium and transport properties of a classical many-body system. It is an important and widely used theoretical tool for the analysis and modeling of the detailed microscopic behavior of many different types of systems, including gases, liquids, solids surfaces and clusters over time scales from picoseconds to microseconds [162]. The idea of MD simulation was introduced by Alder and Wainwrite in 1957 [163] and they found the phase transition mechanism of hard-sphere particles in 1959 [164]. In an MD simulation, the classical (Newton's) equations of motion governing the microscopic time evolution of a many body system are solved numerically. This information can be used to monitor the microscopic mechanisms of energy and mass transfer in chemical and physical processes, and dynamical properties such as absorbtion spectra and rate constants. Equilibrium properties include the energy, temperature and pressure of a system. Transport properties that can be studied include the diffusion coefficient, shear viscosity and thermal conductivity of a system. MD therefore, is a deterministic techniques, i.e., given initial position and velocities, the time evolution of the system is completely determined. The total energy, E of the system is conserved as the system moves along the trajectory. The obvious advantage of MD over MC is that it gives a dynamical history of an atomic system and can also be performed on systems that contain thousands, hundreds of thousands or even millions of

atoms, depending on the application.

Statistical mechanics is applied to MD simulation to interpret instantaneous measurement in terms of equilibrium properties. In statistical mechanics, a macroscopic property of a system is an average of that property over all possible states. This is referred as an ensemble average. The ergodic hypothesis states that the time-averaged properties of a real system are equal to its ensemble averages, so by taking the average of measurements in a molecular dynamics simulation, we obtain the microscopic properties of the system [160, 162].

Various statistical ensembles are used in molecular dynamics simulations and are usually characterized by fixed values of thermodynamic variables such as energy, E; temperature, T ; pressure, P; volume, V; or particle number, N. One fundamental ensemble is called the microcanonical ensemble and is characterized by constant particle number, N; constant volume, V; and constant total energy, E, and is denoted the NVE ensemble. Other examples (for the extended systems) include the canonical or NVT ensemble, the isotropic isothermal-isobaric or NPT ensemble, and the anisotropic isothermal-isobaric or $N\underline{\sigma}T$ ensemble. The thermodynamic variables that characterize an ensemble can be regarded as experimental control parameters that specify the conditions under which an experiment is performed.

The key stages in MD simulation [165] is shown in the form of a flow chart in Fig.5.1. The arrows in the figure track the operations that would be perform by a computer program. We start by specifying the initial atomic or particle positions and velocities usually in a simulation box (or cell) containing a regular array of particles arranged and located at lattices sites and given a random velocities. The particles interact through a potential. The implemented potential determines the extent to which the simulation results represents the system of interest and are used to calculate the total forces acting on each particle. This is obtained by summing the forces exerted on it by all the particles in the system. It is normally assumed that the forces between the particles are pair forces i.e. they act exclusively

between pairs of the particles or atoms. The system is made to evolve with time, with the motion of each atom described by Newton's equations of motion. The co-ordinates and

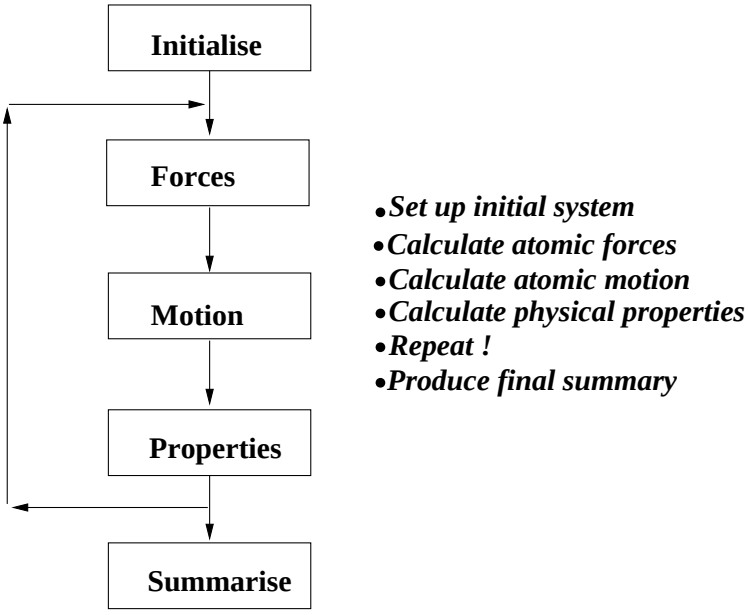


Figure 5.1: The key stages in MD simulation in the form of a flow chart [165].

velocities are periodically updated by integrating the Newton's equations of motion using an integration algorithm. In order to study the time evolution of the system, the updating procedure needs to be repeated several thousand times as indicated by the backward flow of the arrows in Fig. 5.1. The system is then allowed to settle into equilibrium, which is indicated by a constant temperature. After equilibrium has been achieved, the co-ordinate and the velocities of successive time steps are stored and analyzed.

5.1 Intermolecular Potential Models

5.1.1 Introduction

Computer simulation of intermolecular interactions of a system are based on potential energy functions. Within the Born-Oppenheimer approximation, the potential energy is a function of the positions of the nuclei. The total potential energy of a system of *N* atoms can be expanded into terms that depend on individual atoms, pairs, triplets and so on:

$$U(\mathbf{r}_1, \mathbf{r}_2, ...) = \sum_i V_1(\mathbf{r}_i) + \sum_i \sum_{j>i} V_2(\mathbf{r}_i, \mathbf{r}_j) + \sum_i \sum_{j>i} \sum_{k>j>i} V_3(\mathbf{r}_i, \mathbf{r}_j, \mathbf{r}_k) + ... \quad (5.1)$$

The $\sum_i \sum_{j>i}$ notation indicates a summation over all distinct pairs i and j without counting any pair twice. The first term in eqn. 5.1, $V_1(\mathbf{r}_i)$, represents the effect of an external field on the system. The remaining terms represent particle interactions. The V_2 and V_3 are termed as two-body (pairwise) and three-body potential interactions, respectively. Higher order terms are small in comparison with V_2 and V_3 and are therefore neglected [166]. Most work considers only the pairwise interactions, since their contribution is the most significant.

Intermolecular potential function provides detail understanding of the origin of structural features of bulk solid materials and their defects which are often hard to obtain from quantitative quantum mechanical calculations. In recent years, many (empirical) potential models have been developed and applied to a number of different systems. This model differ in degree of sophistication, functional form, fitting strategy and range of interaction, and each can accurately model various specific configurations. Examples of these potential includes: the Lennard-Jones potential [167], Buckingham potential [167], ZBL potential [168], Stillinger-Weber Potential [169], Brenner potential [170], Finnis-Sinclair potentials [171], and Tersoff potential [172] among others. Tersoff, Brenner, and Finnis-Sinclair potentials are all classified as a bond-order potential. By bond-order potential they can,

with the same parameters, describe several different bonding states of an atom, and thus to some extent may be able to describe chemical reactions correctly. And also they share the common idea that the strength of a chemical bond depends on the bonding environment, including the number of bonds and possibly also angles and bond length [173]. The molecular dynamics calculation of the structural and thermodynamic properties of spinel oxynitride materials will be performed by using the Tersoff potential.

5.1.2 Tersoff Potential

The relevance of MD simulations depends crucially on the choice of interatomic potentials used to describe the energy surface between the particles in a simulation. Recently, there has been intense interest developed in modeling the energetics of covalent systems with classical interatomic potentials. Among the many empirical model potentials that have been developed for several element and compound materials in recent years, the Tersoff [172] potential has proved to be the most successful due to it's flexibility and short range of the interatomic interactions. It has been used in a wide range of applications to condensed phases and it reproduces many of the properties of the system. This potential has been applied to the static structural analysis of group VI elements [174, 175, 176], some III-V compounds [177, 178], Si-B-N [179], SiO[180, 181], Cu-Ag alloys [182], CuBr [183], AlN [184], GaN [185], BN [186] and others.

The Tersoff potential has been developed for calculating energies and structure-related properties of multi-component covalently bonded systems. The central idea is that the strength of each atomic bond depends on the local environment, i.e. an atom with many neighbors forms a weaker bond than an atom with few neighbors. Effectively, this means that the strength of the potential depends on the presence of the surrounding atoms. Having 11 atomic and 2 bi-atomic semi-empirical parameters in the potential the total energy is modeled as a sum of pair-like interactions where a pair-like interaction (which plays the role of a bond order) depends on the local environment giving a many-body potential [187].

The Tersoff potential has a limited ability to describe the differences in chemical reactivity but well describes the chemical differences of valence *s* and *p* electron properties. Tersoff-type potential has good transferability and has been an effective tool for examining new materials [184] such as those under study.

Often much success of the Tersoff potential has come about when it effectively treats a binary system as being monatomic - for example in the case of BN, there has been some success with a potential when each atom - whether it be B or N - is regarded as being a "pseudo-atom" of BN [184]. In this way important properties like lattice constants, elastic modulii can reproduced. The clear shortcoming is that any chemical effects are excluded.

Extension to ternary systems has not been as straight forward especially for metal oxynitrides [188]. In this study we suggest that a way forward to treat such ternary systems could be through the Tersoff parametrization for treating binary systems as "pseudo-atoms". Then based on this potential, properties of ternary structures can be estimated. Application is made to properties of some recently studied spinel oxynitrides [156].

5.1.3 Tersoff Potential for Ternary Systems from a Binary Potential

The Tersoff potential is based on a bond-order concept [see Ref.[174, 175, 176]]. The energy *E*, as a function of the atomic coordinates, between two neighboring atoms *i* and *j*, is taken to be [187]:

$$E = \sum_i E_i = \frac{1}{2} = \sum_{i \neq j} V_{ij}, \quad V_{ij} = f_C(r_{ij})[f_R(r_{ij}) + b_{ij} f_A(r_{ij})]; \tag{5.2}$$

where f_R and f_A are the repulsive and attractive pair potential respectively:

$$f_R(r_{ij}) = A_{ij}\text{exp}(-\lambda_{ij} r_{ij}), \quad f_A(r_{ij}) = B_{ij}\text{exp}(-\mu_{ij} r_{ij}); \tag{5.3}$$

and f_C is a smooth cutoff function with parameters *R* and *S* so chosen that to include the first-neighbor shell:

$$f_C(r_{ij}) = \begin{cases} 1 & : r_{ij} < R_{ij} \\ \frac{1}{2} + \frac{1}{2}\cos[\pi(r_{ij} - R_{ij})/(S_{ij} - R_{ij}] & : R_{ij} < r_{ij} < S_{ij} \\ 0 & : r_{ij} > S_{ij} \end{cases} \tag{5.4}$$

The parameter b_{ij} expresses a dependence that can accentuate or diminish the attractive force relative to the repulsive force, according to the local environment, such that

$$\begin{aligned} b_{ij} = \chi_{ij}(1 + \beta_i^{\eta_i}\zeta_{ij}^{\eta_i})^{-1/2\eta_i}, \quad \zeta_{ij}^{\eta_i} = \Sigma_{k\neq i,j} f_C(r_{ik})\omega_{ik} g(\theta_{ijk}) \\ g(\theta_{ijk}) = 1 + c_i^2/d_i^2 - c_i^2/[d_i^2 + (h_i - \cos\theta_{ijk})^2] \end{aligned} \tag{5.5}$$

here *i*, *j*, and *k* label the atoms of the system, r_{ij} is the length of the *ij* bond, and θ_{ijk} is the bond angle between bonds *ij* and *ik*. The term ζ_{ij} defines the effective coordination number of an atom i i.e. the number of nearest neighbors, taking into account the relative distance of the two neighbors, i and k, $r_{ij} - r_{ik}$, and the bond angle, θ_{ijk}, between them with respect to the central atom i. The function $g(\theta)$ has a minimum for $h_i = \cos\theta_{ijk}$, the parameter d_i determines how sharp the dependence on angle is, and c_i expresses the strength of the angular effect. Further mixed parameters for multicomponent systems are defined as:

$$\begin{aligned} \lambda_{ij} = (\lambda_i + \lambda_i)/2, \qquad \mu_{ij} = (\mu_i + \mu_i)/2 \\ A_{ij} = (A_i A_j)^{1/2}, \qquad B_{ij} = (B_i B_j)^{1/2}, \\ R_{ij} = (R_i R_j)^{1/2}, \qquad S_{ij} = (S_i S_j)^{1/2} \end{aligned} \tag{5.6}$$

Singly subscripted parameters, such as λ_i and η_i, depend only on the type of atom. The chemistry between different atom types is locked in the bi-atomic parameters χ_{ij} and ω_{ij}:

$$\begin{aligned} \chi_{ii} &= 1, \qquad & \chi_{ij} &= \chi_{ji} \\ \omega_{ii} &= 1, \qquad & \omega_{ij} &= \omega_{ji} \end{aligned} \tag{5.7}$$

which define only one independent parameter for each per pair of atom types. The χ parameter is used to strengthen or weaken the heteropolar bonds, relative to the value obtained by simple interpolation. Charge transfer between *M*-O, *M*-N, and N-O are taken into account through the parameter χ_{M-O}, χ_{M-N}, χ_{N-O} in our model (where *M*=B, Al, Ga or In). The ω parameter is used to permit greater flexibility when dealing with more drastically different types of atoms. In this study ω have been set to be 1 for *M*-O and *M*-N systems while N-O is set to 0.6381 [187]. The parameters λ_{ij}, μ_{ij}, A_{ij}, B_{ij}, R_{ij}, S_{ij} are assumed to be expressed by single subscript parameters depending only on the atomic types. There are thirteen adjustable parameters: $A, B, \lambda, \mu, R, S, \beta, n, c, d, h$ and the specified interaction parameters χ and ω.

In the case of a binary system - such as BN, AlN, GaN or InN, effective one-atom potentials have been deduced to give a satisfactory description of many properties of such a system. Table 6.2 lists such Tersoff potentials for these binary systems as obtained from previous work.

The challenge is to use the above potentials but to invert the parametric form described above for the binary Tersoff potential into a form that would be useful for describing the ternary system with implicit inclusion of an atomic character. For example with BN we can take $A_i = A_{ij}/A_j$ etc. to get (say) parameters for atomic N in terms of parameters for (say) atoms B.

This work uses the potential parameters proposed by K. Matsunaga *et al* [158] for B, Kroll [189] for N, Munetoh *et al* [190] for O and Nakamura *et al* [177] for Al, Ga and In

respectively which are summarized in Table 5.1.

5.2 Integration Algorithm

The objective of a molecular dynamics simulation is to generate molecular trajectories in phase space by solving differential equation numerically. An object in a system moves under the Newton's equation of motion. The classical Newton's equation of motion for an object in the system is given by:

$$F_i = m\ddot{r}_i = -\nabla_{r_i} U \tag{5.8}$$

where F_i is the force, m is the mass of the molecule and U is the potential function which describes the intermolecular interactions. Given the potential, the forces in the system can be calculated which in turn can be used to evolve the system in time.

To evolve the system in time, an integration algorithm has to be used after the forces have been calculated from the interaction potential. Integration algorithms are based on finite difference method. The finite difference methods are subject to truncation errors and round-off errors. Truncation errors arise because the algorithm is based on a truncated Taylor series expansion. Round-off errors arise from the actual implementation of the algorithm, for example the precision of computer arithmetic [159].

There are various methods of finite difference approaches for numerical integration of Newton's equation of motion, of which there are two that excel in their simplicity of implementation, numerical stability, low memory requirement and satisfactory accuracy, namely: the Verlet algorithm and the leaf-frog methods [167]. The Verlet algorithm is the simplest finite difference method that has been widely use in molecular dynamics. It is derived from a combination of two Taylor expansions, combined as follows. First write the

Taylor series for position from time t forward to $t + \Delta t$:

$$r(t + \Delta t) = r(t) + \frac{dr(t)}{dt}\Delta t + \frac{1}{2}\frac{d^2r(t)}{dt^2}\Delta t^2 + \frac{1}{3!}\frac{d^3r(t)}{dt^3}\Delta t^3 + O(\Delta t^4) \tag{5.9}$$

Then write the Taylor series from t backward to $t - \Delta t$:

$$r(t - \Delta t) = r(t) - \frac{dr(t)}{dt}\Delta t + \frac{1}{2}\frac{d^2r(t)}{dt^2}\Delta t^2 - \frac{1}{3!}\frac{d^3r(t)}{dt^3}\Delta t^3 + O(\Delta t^4) \tag{5.10}$$

Adding these two expansions, the Verlet algorithms becomes:

$$r(t + \Delta t) = 2r(t) - r(t - \Delta t) + \frac{d^2r(t)}{dt^2}\Delta t^2 + O(\Delta t^4) \tag{5.11}$$

or

$$r(t + \Delta t) = 2r(t) - r(t - \Delta t) + \frac{F(t)}{m}\Delta t^2 + O(\Delta t^4) \tag{5.12}$$

The truncation error is $O(\Delta t^4)$. In the Verlet algorithm, the velocity of the particles, $\upsilon(t)$ can be derived from the difference of $r(t + \Delta t)$ from $r(t - \Delta t)$,

$$\upsilon(t) = \frac{r(t + \Delta t) - r(t - \Delta t)}{2\Delta t} + O(\Delta t^2) \tag{5.13}$$

Verlet's algorithm is a two-step method because it estimates $r(t + \Delta t)$ from the current position $r(t)$ and the previous position $r(t - \Delta t)$ [159, 166].

The leap-frog method is a modification of the Verlet algorithm. This algorithm evaluates the velocities at half-integer time steps and uses these velocities to compute the new positions. The leap-frog method can be derived from the Verlet scheme, by defining the velocities at half-integer time steps as follows:

$$\upsilon(t - \frac{1}{2}\Delta t) = \frac{r(t) - r(t - \Delta t)}{\Delta t} \tag{5.14}$$

and

$$v(t+\frac{1}{2}\Delta t) = \frac{r(t+\Delta t) - r(t)}{\Delta t} \tag{5.15}$$

From eqn. (5.15), an expression for the new positions, based on the old positions and velocities is given by

$$r(t+\Delta t) = r(t) + v(t+\frac{1}{2}\Delta t)\Delta t \tag{5.16}$$

The update of the velocities can be obtained from the Verlet algorithm (see eqn. (5.12)):

$$v(t+\frac{1}{2}\Delta t) = v(t-\frac{1}{2}\Delta t) + \frac{F(t)}{m}\Delta t \tag{5.17}$$

The leap-from method ensures that both the positions and the velocity can be stored and calculated. For each time step, the velocities for the current time t may be calculated by the formula:

$$v(t) = \frac{v(t-\frac{1}{2}\Delta t) + v(t+\frac{1}{2}\Delta t)}{2} \tag{5.18}$$

or

$$v(t) = v(t-\frac{1}{2}\Delta t) + \frac{1}{2}\frac{F(t)}{m}\Delta t \tag{5.19}$$

and the total energy $H = K + U$ (where K: kinetic energy, U: potential energy) can be calculated at the same time t as for potential energy. This is necessary because for an isolated system the total energy should be conserved [166, 191].

The leap-frog method is useful when the velocity is required at the same instant for reasons of kinetic energy calculation. In this study we have applied the leaf-frog method to time integration algorithm.

5.3 Periodic Boundary Conditions

The use of periodic boundary conditions (PBC) in MD simulations is to overcome the problem of surface effects (i.e. interaction of atoms with the container walls) and to simulate

more closely the properties of the system. The assumption is to consider a volume, V, containing a number of N atoms. This volume V is called the primary cell; it is representative of the bulk material to the extent that the bulk is assumed to be composed of the primary cell surrounded by exact replicas of itself. These replicas are called image cells. The image cells are each the same size and shape as the primary cell and each image cell contains N atoms, which are image of the atoms in the primary cell. Thus the primary cell is imagined to be periodically replicated in all directions to form a macroscopic sample of the substance of interest [159]. Often, the minimum image convention is employed when the potential range is not too long. And by minimum image convention, only interactions between an atom in the primary cell and the closest periodic image of its neighbors is considered.

5.4 Computational Platforms

We have used GULP [192] and DL_POLY_3 [162, 187] as computational tools to investigate the structural and thermodynamical properties.

5.4.1 DL_POLY

DL_POLY is a general purpose molecular dynamics simulation package (software) designed to run on a wide range of computers; from single-processor workstations to multi-processor computers, with accent on the efficient use of multi-processor power. DL_POLY is a FORTRAN package of subroutines and data files written by W. Smith, T. R. Forester, and I. Todorov and designed for MD study of a wide range of systems such as liquids and solutions, spectroscopy, ionic materials of high complexity, molecular crystals, polymers (both biological and synthetic macromolecules), glasses, membranes, proteins, solid and liquid interfaces, catalysis, liquid crystals, intercalation and clathrates, and novel systems.

DL_POLY to date is made up of two known versions, namely: DL_POLY_2 and DL_POLY_3. DL_POLY_2 is based on a replicated data (RD) parallelization strategy and permit simula-

tion of systems up to 30, 000 atoms. DL_POLY_3 on the other hands, is a MD software with inherent parallelization design based on domain decomposition (DD) and linked cells algorithms. It exhibits excellent parallel performance and ability to handle simulations of systems of order of tens of millions of atoms and beyond.

In this study, we have used DL_POLY_3 code to calculate the thermodynamical properties of the spinel oxynitride material. In the MD scheme, we have used the Tersoff potential force field for the intermolecular interaction, leap-frog method for the integration algorithms together with *NPT* Berendsen f_1 f_1 (f_1 f_1 = 0.1 1.0 represent the thermostat and barostat relaxation times in picoseconds (ps) respectively) ensemble. Simulations are performed within the cubic periodic boundary conditions, with 448 atoms. Coordinates and velocities were updated after time steps of 0.0001 ps. After 100 000 iterations with an equilibration time steps of 1000, different average properties are then calculated.

5.4.2 GULP

The General Utility Lattice Program (GULP) is a program for performing a variety of types of simulation on materials using boundary conditions of 0-D (molecules and clusters), 1-D (polymers), 2-D (surfaces, slabs and grain boundaries), or 3-D (periodic solids). The GULP code focus mainly on analytical solutions, through the use of static lattice or lattice dynamics lattice rather than on molecular dynamics [192]. Variety of force fields can be implemented within the GULP code such as the Tersoff potential which we have used in the study. Analytical derivatives are included up to at least second order for most force fields, and to third order for many. A detailed description of the GULP program can be found in the GULP home page **https://www.ivec.org/gulp**.

Structural optimization or the energy minimization in the GULP program uses the Newton-Raphson method based on an approximate Hessian Matrix, H. Hessian Matrix, H is calculated from the static second derivatives of the internal energy. This matrix is updated subsequently for a number of cycles by using the Broyden-Fletcher-Goldfarb-

Shanno, (BFGS) algorithm. The BFGS algorithm is generally recognized as the more efficient optimizer [192, 193]. Physical properties based on the curvature of the energy surface about the minimum can therefore be calculated from the optimized structure. These include crystal properties, such as the elastic constants, bulk modulus, shear modulus, Young modulus and the Poisson ratios among others.

Using the Tersoff potential for ternary systems, we have calculated these properties by simulating 448 atoms of the various 56-atomic spinel related structures within a $2 \times 2 \times 2$ supercell. For supercell higher than a $2 \times 2 \times 2$ cell, we found no significant system size dependence for the simulated structural properties.

Table 5.1: Parameters set (1) for the Tersoff potential, for atoms of spinel oxynitride M_3NO_3 where M = B, Al, Ga and In respectively.

Elements	B [158]	Al [177]	Ga [177]	In [177]	N [189]	O [190]
A (eV)	2.7702 $\times 10^2$	746.698	2839.821	4403.956	1.1000 $\times 10^4$	1.88255 $\times 10^3$
B (eV)	1.8349 $\times 10^2$	40.451	114.786	329.104	2.1945 $\times 10^2$	2.18787 $\times 10^2$
$\lambda(\mathring{A}^{-1})$	1.9922	2.4647	3.2834	2.9039	5.7708	4.17108
$\mu(\mathring{A}^{-1})$	1.5856	0.9683	1.715	1.7978	2.5115	2.35692
β	1.6000 $\times 10^{-6}$	1.094932	0.2358624	2.10871	1.0562 $\times 10^{-1}$	1.1632 $\times 10^{-7}$
n	3.9929	6.086505	3.4729041	3.40223	12.4498	1.04968
c	5.2629 $\times 10^{-1}$	0.074836	0.0762977	0.084215	7.9934 $\times 10^4$	6.46921 $\times 10^4$
d	1.5870 $\times 10^{-3}$	19.569127	19.796474	19.2626	1.3432 $\times 10^2$	4.11127
h	0.5000	-0.659266	7.1459174	7.39228	-0.9973	-8.45922 $\times 10^{-1}$
$R(\mathring{A})$	1.8	3.5	3.4	3.4	2.0	1.7
$S(\mathring{A})$	2.1	3.7	3.6	3.6	2.3	2.0
Interactions $(i-j)$	B-N	Al-N	Ga-N	In-N		
χ_{i-j}	1.1593	1.1593	1.1593	1.1593		
ω_{i-j}	1.0000	1.0000	1.0000	1.0000		
Interactions $(i-j)$	B-O	Al-O	Ga-O	In-O	N-O	
χ_{i-j}	1.0025	1.0025	1.0025	1.0025	0.9685	
ω_{i-j}	1.0000	1.0000	1.0000	1.0000	0.6381	

Chapter 6

Structural and Thermodynamics Properties of Spinel Oxynitrides

6.1 Structural Properties

To test the reliability of the Tersoff potential, we investigate the elastic properties of the oxynitride materials and their lattice constants using some existing Tersoff potentials obtained from the literature. The choice used was given in Table 5.1. Using the potentials in Table 5.1 calculated bulk properties are obtained and are given in Table 6.1. To determine the isothermal bulk modulus, B^{eos} at zero pressure for these materials, we have analyzed simulated data at different pressures from 0 GPa to 50 GPa and fitted the behaviour to a third order Birch equation of state [143, 194].

The calculated elastic properties do not show good agreement with our recent results from the *ab*-intio calculations based on the local density approximation (LDA) [156]. We infer from this, that the Tersoff potentials from Table 5.1 may not be reliable especially for a three component systems of the spinel oxynitrides of Al, Ga and In atoms. The potentials for B atom seems to be in good agreement when the cutoff parameter χ is adjusted but this may be fortuitous.

Table 6.1: Calculated equilibrium properties, elastic constants and effective (Voigt) isotropic elastic modulii for Spinel Oxynitrides compared with the results from *ab*-initio calculations. The calculated properties are from parameter set (1) using the Gulp code and B^{eos} from DL_POLY_3. All modulii are in GPa.

	Spinel	$c_{1,1}$	$c_{1,2}$	$c_{4,4}$	B	G	E	ν	a(Å)	B^{eos}
Present	B_3NO_3	864	198	198	420	184	791	0.18	7.117	258
	Al_3NO_3	446	220	220	294	117	300	0.33	8.917	96.4
	Ga_3NO_3	234	84	84	134	47	190	0.26	8.636	183
	In_3NO_3	34	26	25	28	7	6	1.3	10.343	37.4
Calculation[a]	B_3NO_3	190	418	415	342	203	508	0.25	6.842	339
	Al_3NO_3	344	179	184	234	143	357	0.25	7.937	233
	Ga_3NO_3	316	202	131	240	101	266	0.32	8.267	232
	In_3NO_3	212	136	76	161	61	162	0.33	9.037	163

[a]Reference [156]

At this point we point out there has been extensive work in establishing Tersoff potentials for binary nitride systems but treating atoms in this systems as "pseudo-atoms"[158, 195, 184]. In other words in c-BN, for example as Tersoff potential has been obtained for a "BN" pseudo-atom. Obviously the shortcoming of this is that any chemical interactions are not considered. In order to obtain a new set of values for the Tersoff potential of these materials, we therefore adjusted and obtained the potential parameters for Al, Ga and In atoms respectively from the potentials of B, BN, AlN, GaN and InN counterparts, that have been presented in Refs. [158, 195, 184] and also in Table 6.2. The expression employed is essentially the reverse of the expressions given in the Tersoff equations for binary systems [196].

In Table 6.3 we present the parameters obtained here together with adjusted parameter, χ and ω. To test the reliability of the new potentials in Table 6.3, we have again obtained equilibrium lattice constants, bulk modulus and their elastic and shear constants. First we have used the new potentials to obtain results for the binary cubic nitrides for BN, AlN, GaN and InN as a benchmark and these are given in Table 6.4. As we can see from Table 6.4 there is a good agreement with other calculations and the experiment but we stress that

Table 6.2: Tersoff potential parameters for BN, AlN, GaN and InN.

Elements	BN[a]	AlN[a]	GaN[a]	InN[b]
A (eV)	4460.8	1730.0	2975.4	3297.0
B (eV)	3613.4	246.1	540.31	280.0
$\lambda(\mathring{A}^{-1})$	2.9984	3.20	3.3718	3.3
$\mu(\mathring{A}^{-1})$	2.7842	1.853	2.22	1.853
β	1.1134 $\times 10^{-5}$	1.1 $\times 10^{-6}$	1.5724 $\times 10^{-7}$	1.1 $\times 10^{-6}$
n	0.36415	0.72	0.72751	0.72
c	1092.9287	100390	38049	100390
d	12.38	16.217	4.384	16.217
h	-0.5413	-0.598	-0.57058	-0.598
$R(\mathring{A})$	2.1	2.34	2.4	2.6405
$S(\mathring{A})$	0.2	0.15	0.2	0.15

[a]Reference [195]
[b]Reference [184]

unlike many of the earlier works these potentials retain an atomic character.

Secondly, for the interaction *M*-N-O of the cubic oxynitride spinels, we have presented summary of the results in Table 6.5. As a follow up for the benchmark results, again we seen an agreement with the *ab*-initio calculations based on the local density approximation (LDA). This gives us confidence in applicability of the potentials to the ternary system.

We have also calculated the radial distribution function g(r) for these system. The RDF plots in Appendix B shows how the positional peak distances for all the pairs of the oxynitride spinel system, are affected at finite temperatures.

Table 6.3: The adjusted Parameters (parameter set (2)) for the Tersoff potential, for atoms of spinel oxynitride M_3NO_3, where M = B, Al, Ga and In respectively.

Elements	B [158]	Al	Ga	In	N [189]	O [190]
A (eV)	2.7702 $\times 10^{2}$	107.4	184.8	204.7	1.1000 $\times 10^{4}$	1.88255 $\times 10^{3}$
B (eV)	1.8349 $\times 10^{2}$	12.50	27.44	14.22	2.1945 $\times 10^{2}$	2.18787 $\times 10^{2}$
$\lambda(\mathring{A}^{-1})$	1.9922	2.126	2.240	2.193	5.7708	4.17108
$\mu(\mathring{A}^{-1})$	1.5856	1.055	1.264	1.055	2.5115	2.35692
β	1.6000 $\times 10^{-6}$	0.1581 $\times 10^{-6}$	0.2260 $\times 10^{-6}$	0.1581 $\times 10^{-6}$	1.0562 $\times 10^{-1}$	1.1632 $\times 10^{-7}$
n	3.9929	7.895	7.977	7.895	12.4498	1.04968
c	5.2629 $\times 10^{-1}$	48.34	18.32	48.34	7.9934 $\times 10^{4}$	6.46921 $\times 10^{4}$
d	1.5870 $\times 10^{-3}$	0.2079 $\times 10^{-2}$	0.5620 $\times 10^{-3}$	0.2079 $\times 10^{-2}$	1.3432 $\times 10^{2}$	4.11127
h	0.5000	0.5524	0.5270	7.39228	0.5524	-8.45922 $\times 10^{-1}$
$R(\mathring{A})$	1.8	2.006	2.057	2.263	2.0	1.7
$S(\mathring{A})$	2.1	2.421	2.432	2.753	2.3	2.0
Interactions $(i-j)$	B-N	Al-N	Ga-N	In-N		
χ_{i-j}	1.1593	4.2001	3.12379	3.7393		
ω_{i-j}	1.0000	1.0000	1.0000	1.0000		
Interactions $(i-j)$	B-O	Al-O	Ga-O	In-O	N-O	
χ_{i-j}	0.9988	2.8650	3.20298	3.0880	0.9685	
ω_{i-j}	1.0000	1.0000	1.0000	1.0000	0.6381	

Table 6.4: The calculated and experimental elastic constants, equilibrium lattice constants and bulk modulus for the cubic structures BN, AlN, GaN and InN. These properties are calculated from parameter set (2) using the Gulp code.

	c-BN	c-AlN	c-GaN	c-InN
$c_{1,1}$				
Present	594	440	365	273
Other calculations	774^a, 837^b, 990^c	348^d, 302^e, 304^b	296^h, 322^i, 259^e	184^b, 189.6^e, 187^j
Experiment	820^f	328^g	264^g	172^g
$c_{1,2}$				
Present	302	107	110	83
Other calculations	179^a, 182^b, 441^c	168^d, 163^e, 152^b	138^h, 156^i, 155.1^e	116^b, 119.6^e, 125^j
Experiment	190^f	139^g	153^g	119^g
$c_{4,4}$				
Present	290	72	82	62
Other calculations	433^a, 493^b, 394^c	135^d, 192^e, 199^b	126^h, 138^i, 189.4^e	177^b, 147.8^e, 86^j
Experiment	480^f	133^g	68^g	37^g
B				
Present	389	206	186	140
Other calculations	384^k, 404^l, 400^b	212^l, 203^b, 208.3^e	212^l, 201^b, 189.7^e	163^l, 139^b, 142.9^e
Experiment	400^f	202^g	185^g	136^g
Å				
Present	3.656	3.777	3.914	4.121
Other calculations	3.746^l, 3.590^b	4.346^l, 4.320^b	4.499^l, 4.460^b	4.980^l, 4.920^b
Experimental	3.615^m	4.370^m	4.500^m	4.980^m

[a]Reference [197] [d]Reference [198] [g]Reference [199] [j]Reference [200] [m]Reference [140]
[b]Reference [73] [e]Reference [184] [h]Reference [201] [k]Reference [202]
[c]Reference [203] [f]Reference [204] [i]Reference [205] [l]Reference [156]

Table 6.5: Calculated equilibrium properties, elastic constants and effective (Voigt) isotropic elastic modulii for the modified Tersoff potentials of Spinel Oxynitrides compared with the results from *ab*-initio calculations. These properties are calculated from parameter set (2) using the Gulp code and B^{eos} from DL_POLY_3. All modulii are in GPa.

	Spinel	$c_{1,1}$	$c_{1,2}$	$c_{4,4}$	B	G	E	ν	a(Å)	B^{eos}
Present	B_3NO_3	616	183	183	327	155	532	0.23	7.125	323
	Al_3NO_3	405	159	136	240	124	295	0.27	7.478	214
	Ga_3NO_3	316	135	139	221	107	273	0.26	7.195	217
	In_3NO_3	265	106	106	158	63	205	0.28	8.203	181
Calc. [156]	B_3NO_3	190	418	415	342	203	508	0.25	6.842	339
	Al_3NO_3	344	179	184	234	143	357	0.25	7.937	233
	Ga_3NO_3	316	202	131	240	101	266	0.32	8.267	232
	In_3NO_3	212	136	76	161	61	162	0.33	9.037	163

6.2 Thermodynamic Properties

We finally investigate the thermodynamic properties of the metal nitrides and ternary spinel oxynitrides M_3NO_3. We consider the thermal expansion coefficient and the specific heat at zero pressure. The thermal expansion and specific heat are of practical and theoretical importance and together, both are essential tools for predicting the thermodynamic equation of state. The thermal expansion coefficient, α measures how the lattice constant or volume responds to an isometric change in temperature. It is obtained from the temperature derivative of the lattice constants for cubic materials or volumes for non cubic compounds,

$$\alpha = \frac{1}{a}\left(\frac{\partial a}{\partial T}\right)\Big|_p \qquad \text{or} \qquad \alpha = \frac{1}{v_0}\left(\frac{\partial v}{\partial T}\right)\Big|_p \tag{6.1}$$

where a is the lattice parameter and v_o is the volume at zero pressure. At temperatures below the Debye temperature, quantum effects are important in determining the thermodynamic properties. Since molecular dynamics treats the motion of atoms somewhat classically it is unlikely that the method will be valid at lower temperatures where sensitive

quantum effects are important. For this reason we follow a recent suggestion [197] only to examine α above the Debye temperature. From the elastic constant $c_{1,1}$ in Table 6.5, we can calculate the Debye temperature using the following empirical relation [206] for cubic structures:

$$\theta_D = -11.3964 + 0.3475c_{1,1} - 1.6150 \times 10^{-5}c_{1,1}^2 \tag{6.2}$$

This analysis allow us to use such empirical relation to predict Debye temperature of compounds from structural properties. The calculated Debye temperatures are shown in Table 6.6. We notice that the Debye temperature increases with increasing material rigidity or hardness as expected and the values deduced using the above empirical equation are not too inconsistent with experiment. The Debye temperature of the ternary spinel oxynitride compounds have also been deduced and cubic binary nitride counterpart and in some cases with diamond. Note that Eqn. 6.2 formally applies only to cubic materials as is the case with the present application.

In Figure 6.1, we display the variation of the lattice parameter versus temperature, for the oxynitride spinel M_3NO_3. From the change in cell parameter with temperature - and recalling that we are only considering temperature changes above the Debye temperature - we proceed to calculate α from the change in cell constant with temperature by fitting this to a second order polynomial for B_3NO_3, Al_3NO_3, Ga_3NO_3, and In_3NO_3 respectively:

$$a(T)(\mathring{A}) = 7.32 - 7.32 \times 10^{-5}T + 5.67 \times 10^{-8}T^2 \tag{6.3}$$

$$a(T)(\mathring{A}) = 8.05 - 8.09 \times 10^{-6}T + 1.87 + \times 10^{-7}T^2 \tag{6.4}$$

$$a(T)(\mathring{A}) = 7.35 - 3.45 \times 10^{-4}T + 5.43 \times 10^{-7}T^2 \tag{6.5}$$

$$a(T)(\mathring{A}) = 8.38 + 3.26 \times 10^{-4}T + 2.89 \times 10^{-8}T^2 \tag{6.6}$$

The calculated values are given in Table 6.6. In the case of the binary nitride there is quite a deviation - up to an order of magnitude in reported experimental values so we suggest

that further work is needed here, There is good agreement between calculated values and experiment for c-BN, c-GaN and diamond.

Finally the specific heat at constant volume (C_v) of the nitrides and spinel M_3NO_3 is calculated using the Tersoff potential - again at temperatures above the Debye temperatures for reasons mentioned earlier. The constant volume heat capacity measures how the internal energy responds to an isometric change in temperature. It is obtained from the temperature derivative of the total energy of the system:

$$C_v = \left(\frac{\partial E}{\partial T}\right)\Big|_v \tag{6.7}$$

From the gradient of the energy-temperature curve, we estimated the specific heat of these ternary oxynitride spinel materials and we display these values in Table 6.6 along side results for cubic binary nitrides and diamond. The specific heat values are approaching the classical Dulong-Petit result (3 k_B), which is obtained at high temperature for all solids. Notably in the case of the binary nitrides values we obtain are comparable to experimentally measured values.

6.3 Conclusion

We have proposed a series of Tersoff potentials for various ternary spinel systems incorporating boron, some metals with oxygen and nitrogen, and tested the validity of the potentials by calculating the structural, elastic and thermodynamical properties of binary nitrides and M_3NO_3 (M = B, Al, Ga and In) spinels using molecular dynamics simulations. The parameters are derived in such a way to retain an atomic character. Structural and elastic properties are in agreement with available theoretical and experimental data. Different thermodynamic properties such as Debye temperature, thermal expansion coefficient and specific heat are also predicted and, in the main, show agreement with experiment for binary nitrides. We also made some suggestion as to the thermal behavior of potentially

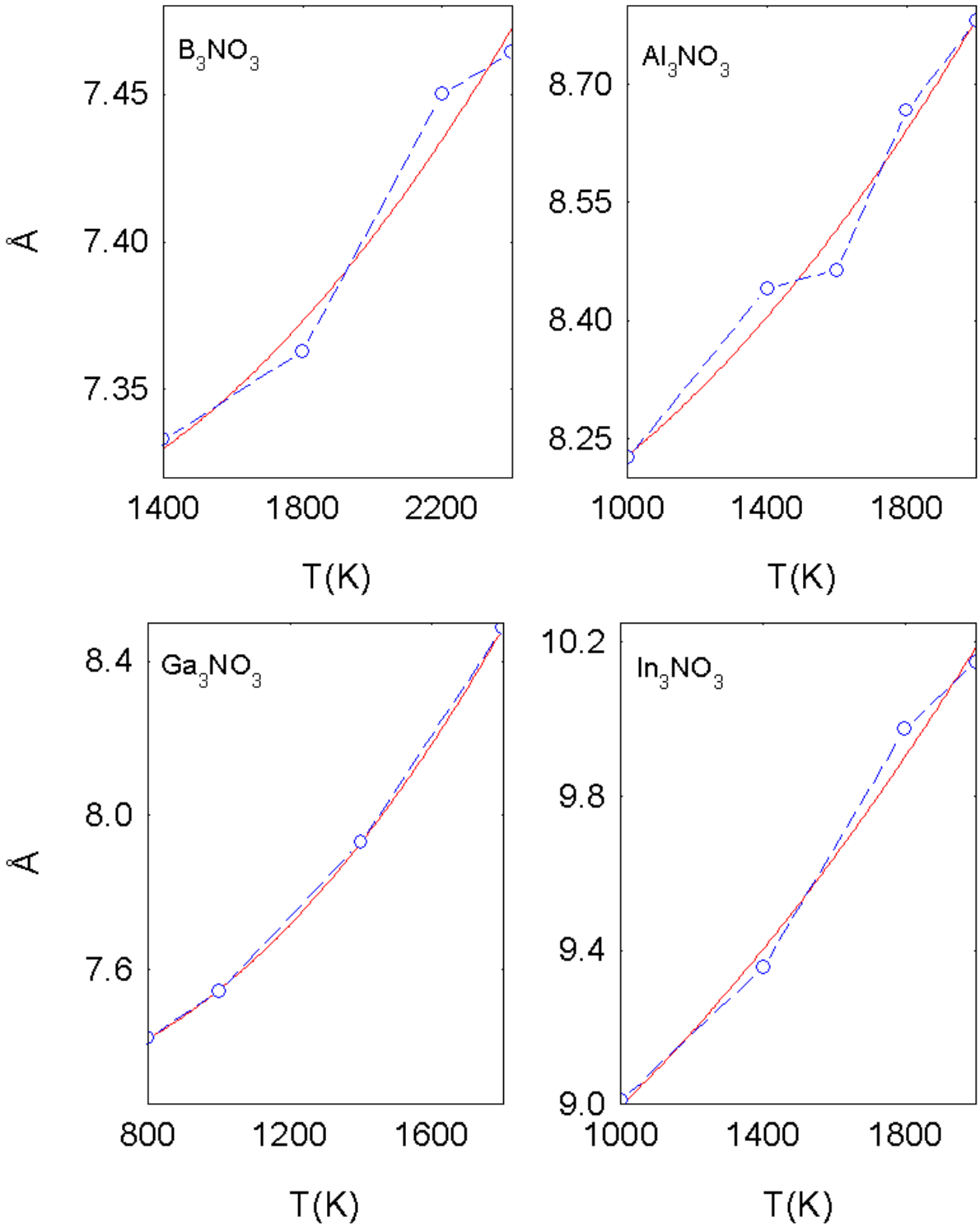


Figure 6.1: The lattice parameter as a function of temperature for B_3NO_3, Al_3NO_3, Ga_3NO_3 and In_3NO_3.

Table 6.6: Calculated values for the Debye temperature, thermal expansion coefficients and specific heat of some cubic nitrides and the spinel oxynitride compounds.

Material	θ_D (K)	α (K^{-1}) $\times 10^{-5}$	C_v (k_B)
c-BN calc.	1483	1.668	2.41
expt.	(1962.1)[a], (1710)[b]	(0.539)[a], (0.6166)[b]	(1.332)[a], (3.02)[b]
	(1730)[c], (1700)[d]	(1.15)[c], (0.596)[d]	(5.53)[c], (3.02)[d]
c-AlN calc.	1205	5.511	3.20
expt.	(911.6)[e]	(0.622)[e]	(3.03)[e]
c-GaN calc.	1042	5.129	3.28
expt.	(823)[f], (607)[g]	(0.561)[f], (4.49)[g]	(3.11)[f], (3.01)[g]
c-InN calc.	817	5.166	1.50
Diamond calc.	1858	0.5627	3.08
expt	(2220)[h], (2240)[i]	(0.48)[j], (0.08)[k]	3.10[h]
B_3NO_3	1516	1.345	2.72
Al_3NO_3	1131	5.011	2.39
Ga_3NO_3	925	8.791	1.93
In_3NO_3	796	8.910	1.52

[a][207], [b][197], [c][208], [d][209], [e][210], [f][201], [g][211], [h][212], [i][213], [j][214], [k][215]

new spinel oxynitrides and it is suggested that such materials will have thermal properties comparable to their binary nitride counterparts.

The results show the ability of the empirical potential in combination with the molecular dynamics simulation, to predict and give some understanding into basic physical properties of the binary nitrides and make prediction of the thermal properties of ternary spinel oxynitrides B_3NO_3, Al_3NO_3, Ga_3NO_3, and In_3NO_3.

Chapter 7

Defective Study of the Structures of Spinel Oxynitride Materials

So far we have discussed a well ordered bulk spinel structure of an oxynitride material. Now we discuss a disordered or defective nature of these materials and to show that these systems could also have interesting physical properties.

Defects disrupt the periodicity of the crystal structures. They are defined by their chemical nature and their geometrical configuration and example includes line defects (dislocations), planar defects, surface defects (stacking faults) and point defects. Point defects are the most prevalent on an atomic scale as compared to others. Point defects can be divided into intrinsic (or native) defects, formed only from the host atom types, and extrinsic (or impurities) defects consisting of foreign atoms.

These defect can be missing atoms in a periodic lattice site (vacancies), atoms at the wrong lattice site (antisite/substitutional defects) or atoms in between the ordinary lattice sites (interstitial or self-interstitial defects). Vacancies, self-interstitial and antisite defects are classified under intrinsic defects whereas substitutional defects are extrinsic defects. The different kinds of point defects can form complexes especially, when a vacancy encounters an impurity, the two may bind together if the impurity is too large for the lattice

[216].

In a periodic crystal a defect can have a very large influence on the material properties. Defects can have a large impact on, for example, the strength of the material, its optical properties, the mechanical, or the electrical properties. Even defects with a concentration as low as 10^{16} cm^{-3} often predominantly determine the bulk properties of solids [217]. Defects are also responsible for most of the phenomena associated with atomic transport such as migration, diffusion, precipitation. Therefore, the basic science of defect formation, structure and properties are the key frontiers in the chemistry, physics and material science of most systems [161]. The most common type of intrinsic defect is the vacancy, i.e., a vacant atomic site. And interestingly, the effects of vacancy are seen to be responsible for the color of most of the transparent ionic crystals. This present work focuses only on the defects caused by a vacant atomic site (i.e. vacancy).

Crystal defects are also assumed in spinel structures, because of the deviation from the ideal composition. The relationship between the composition and lattice parameters of spinel aluminium oxynitride or γ-alons have been studied by Willems and *et al* [218]. They found out that the lattice parameter of γ-alons increases almost linearly as the aluminium nitride content increases. In this work however, our focus is to investigate how on creating a vacant atom in the spinel oxynitride structure can affect the electronic properties (such as the density of states) and the elastic properties.

7.1 Types of Defective Models

There are basically two types of defective models for spinel-type oxynitride structures. They are the Constant Anion Model and the Constant Cation Model proposed by McCauley [219] which he applied to the spinel aluminium oxynitride or γ-alons systems.

7.1.1 Constant Anion Model

In the constant anion model, the defects are assumed to be the cation vacancies, and as such for this study the vacancies are found in the B, Al, Ga and In atoms of their respective oxynitride structures. The constant anion model contains a constant number of 32 anions (the number of the anion sites in one spinel unit cell). The model assumes the following formula:

$$M_{(64+x)/3}V_{M[(8-x)/3]}\mathrm{O}_{32-x}\mathrm{N}_x \tag{7.1}$$

where M represents B, Al, Ga, and In respectively, V is the cation lattice vacancy, O is oxygen, and N is nitrogen. This model has been confirmed by the work done by Tabary *et al* [220], where they performed a structure refinements on aluminium oxynitride with x-ray diffraction (XRD) and neutron diffraction. Fang *et al* [150], also published a structural model based on *ab*-initio calculations that supports the constant anion model.

7.1.2 Constant Cation Model

The constant cation model is quite the opposite of the constant anion model. In this model, the octahedral and tetrahedral cation sites are always fully occupied. The predominant defects are the oxygen or nitrogen interstitials, instead of a *M* or cation vacancies, normally within the range of oxynitride material. The model assumes the following formula:

$$M_{24}\mathrm{O}_{(72-3x)/2}\mathrm{N}_x(\mathrm{O},\mathrm{N})_{i,[(72-x)/2-32]} \tag{7.2}$$

This model have been reported to be unlikely by the work done by Fang *et al* [150].

7.2 Structure of Spinel $M_{23}N_8O_{24}$ with M Vacancies

To model the defective spinel oxynitride of the various structure under study, we employed the constant anion model. Guided by the work of Fang *et al* [150] on aluminium oxynitride and Kroll *et al* [136] on gallium oxynitride, we started from our lowest energy model of M_3NO_3 with a 56-atom unit cell that comprises a spinel structure. We created a cation vacancy by removing one of the M atoms from their respective structures with a complete anion sublattice. The cation vacancy are created either on the tetrahedral or the octahedral sites. The N atoms are arranged as far as possible, to minimize the strong interactions between the N^{3-} ions thereby achieving a low energy structure. The nitrogen positions of the initial M_3NO_3 structure provide a good starting point for structures with either tetrahedral or octahedral M cation vacancy. Apart from creating a vacant cation M atom at the tetrahedral or octahedral sites, this structure is quite similar with the spinel oxynitride M_3NO_3 (See Section 4.2).

Ab-initio calculations are performed for the these defective structures with one M vacancy at the tetrahedral or octahedral site. The symmetry of the system is reduced because of the M vacancy. The calculated volumes of the cell and the lowest energy structure for both tetrahedral and octahedral sites are listed in Table 7.1 and are compared with the LDA and GGA result for the bulk M_3NO_3 oxynitride spinel and other available theoretical and experimental results. Energy difference between the bulk oxynitride systems with their vacancy related systems means that the bulk spinel are more likely to be synthesized. Fig. 7.1 shows the vacancy sites for the octahedral and tetrahedral configurations. The site without bond attached to the atoms indicates that an atom has been removed hence creating a vacancy.

Table 7.1 shows the vacancy site where the most stable (or lowest energy) structure of these materials are found. The lowest energy structure of $B_{23}N_8O_{24}$, $Ga_{23}N_8O_{24}$, and $In_{23}N_8O_{24}$ exhibits a tetrahedral vacancy whereas $Al_{23}N_8O_{24}$ exhibits an octahedral va-

cancy site (which is in agreement with Fang *et al* on $Al_{23}N_5O_{27}$ [150]). However, Table 7.1 shows that the vacancy sites are equally probable since total energy differences are so small. The calculated lattice geometry are very similar to being cubic. The calculated volume, using the LDA and GGA (in parentheses) is slightly higher by a small margin in comparison to their respective $M_{24}N_8O_{24}$ systems, however, this effect could lower their structural stability. We have also shown comparison for the defective aluminium and gallium spinel oxynitride systems with available experimental and other calculated values.

Table 7.1: Theoretical LDA and GGA (in parentheses) results for $M_{23}N_8O_{24}$. This results are compared with the available theoretical and experimental values of $M_{24}N_8O_{24}$.

	Energy (eV/atom)		Volume $(\text{Å})^3$	
Defective spinel	Oh site	Td site	Oh site	Td site
$B_{23}N_8O_{24}$	-8.331 (-7.331)	-8.368 (-7.352)	327.1 (363.0)	328.7 (351.2)
$Al_{23}N_8O_{24}$	-8.115 (-7.312)	-8.114 (-7.311)	500.5 (523.9)	500.2 (523.6)
$Ga_{23}N_8O_{24}$	-6.775 (-5.923)	-6.777 (-5.926)	570.2 (596.8)	569.5 (595.8)
$In_{23}N_8O_{24}$	-5.806 (-5.393)	-6.294 (-5.395)	738.3 (812.2)	733.8 (811.4)
Other Calculation				
$Al_{23}N_5O_{27}$			492.8[a]	
			503.6[a][Expt.]	
$Ga_{23}N_5O_{27}$			541.1.8 (571.4)[b]	
	Energy (eV/atom)		Volume $(\text{Å})^3$	
"Ideal" spinel				
$B_{24}N_8O_{24}$	-8.398 (-7.382)		320.3 (335.3)	
$Al_{24}N_8O_{24}$	-8.211 (-7.382)		500.0 (523.0)	
$Ga_{24}N_8O_{24}$	-6.854 (-5.986)		565.0 (598.0)	
$In_{24}N_8O_{24}$	-6.366 (-5.455)		738.0 (800.5)	
Other Calculation				
$Al_{24}N_8O_{24}$			493.8 (525.6)[a]	
			507.2[a][Expt.]	
$Ga_{24}N_8O_{24}$	-6.874[c] (-6.209)[b]		546.6 (577.2)[b]	

[a]Reference [150]
[b]Reference [136]
[c]Reference [137]

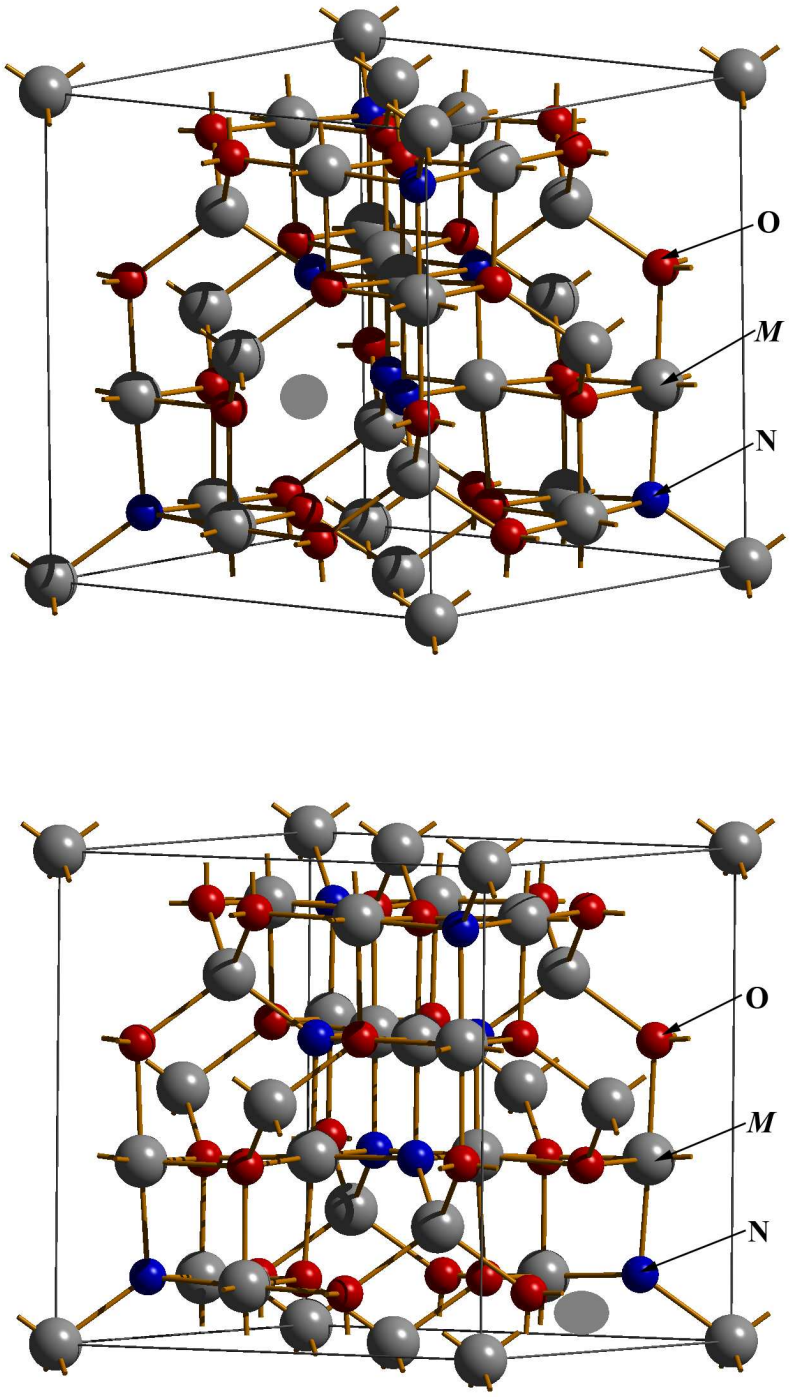


Figure 7.1: The unit cell structure of the defective oxynitride spinel structure showing the octahedral (top) and tetrahedral (bottom) configurations. The non bonded atom shows a vacancy site.

7.3 Elastic Constants of the Defective Oxynitride Spinel.

The three cubic elastic constants c_{11}, c_{12}, and c_{44} for the defective oxynitride system with vacancies at their tetrahedral and octahedral sites have been examined. We have followed same procedure used for the bulk oxynitride spinel systems (see Section 4.3), since with the vacancies, the unit cells appeared to be slightly cubic. The calculated elastic constants and shear properties are shown in Table 7.2. These values have been compared with their respective bulk systems. And as with their bulk systems, there seems to be a definite trend- the steady increase in bulk and shear moduli in going from the vacancies of boron to indium systems, yet as expected, these leads to reduction elastic and shear values with the introduction of vacancies at these sites. Again as we pointed out with total energies for the vacancy sites, the values for the bulk and shear modulus of the oxynitride spinel are very close and as such we suggest that their are no site preferences.

The calculated elastic and shear properties of boron at their various vacancy sites have been omitted in Table 7.2. We noticed that, as with the bulk boron oxynitride spinel, a tetragonal elastic instability yet exist for the boron vacancy sites when the value of $(c_{11} - c_{12})$ was calculated.

7.4 Band Structure and DOS of Defective Oxynitride Spinel

The calculated defect-related band structures and their density of states (DOS) of the various defects in oxynitride spinel systems are shown in Fig. A.1 to A.2. Analysis of band structures and DOS of these defective phase oxynitride spinel shows a similarity with their bulk oxynitride systems. The defect behavior of the systems exhibit an acceptor characteristics with vacancy sites at the octahedral (Oh) and the tetrahedral (Td). The calculated energy gaps are summarized in Table 7.3 where comparison is also made with the energy band gap of the bulk systems. Here we see that the band gaps changes with vacancy sites

Table 7.2: Calculated LDA elastic constants and effective (Voigt) isotropic elastic modulii for defective oxynitride spinel. The values of the tetrahedral and octahedral vacancy sites have been compared with the bulk oxynitride spinel systems.

		c_{11}	c_{12}	c_{44}	B	G	B/G	E	ν
Td-Vacancy									
	Al_3NO_3	362	150	130	221	120	1.84	305	0.27
	Ga_3NO_3	293	180	107	218	87	2.51	230	0.32
	In_3NO_3	190	124	63	146	51	2.86	137	0.34
Oh-Vacancy									
	Al_3NO_3	322	172	152	222	122	1.82	309	0.27
	Ga_3NO_3	296	180	109	219	89	2.46	235	0.32
	In_3NO_3	185	121	61	142	49	2.90	132	0.35
Bulk M_3NO_3									
	B_3NO_3	140	381	411	301	198	1.52	488	0.23
	Al_3NO_3	344	179	184	234	143	1.64	357	0.25
	Ga_3NO_3	316	202	131	240	101	2.38	266	0.32
	In_3NO_3	212	136	76	161	61	2.64	162	0.33

although the octahedral and tetrahedral sites are equally probable due to similar energies. Therefore, we suggest that site preferences of oxynitride spinel system could be well associated with their energy band gaps.

Table 7.3: Calculated band gaps of the oxynitride spinels and their vacancy sites related structures.

	Band gap (eV)			Band gap (eV)	
Spinel	LDA	GGA	Vacancy	Td site	Oh site
B_3NO_3	4.60	4.43	B	3.41	3.37
Al_3NO_3	4.02	3.70	Al	4.16	4.06
Ga_3NO_3	1.72	1.37	Ga	1.82	1.67
In_3NO_3	0.40	0.40	IN	0.46	0.20

7.5 Conclusions

In conclusion, we found that defective oxynitride spinel of boron, gallium and indium favors vacancies on tetrahedral sites over the octahedral vacancies for their lowest energy

structures. This is not the case for aluminium oxynitride spinel whose lowest energy state favors vancancies on the octahedral sites. However, they could be equally probable due to similar energies in their vacancy sites. The energy differences suggest that having vacancies at either octahedral or tetrahedral sites, makes these systems less likely to be synthesized. We also deduced that since the volume of the defective systems are slightly higher than their respective bulk systems, the structural stability could be adversely affected and thus be lowered. And finally, we suggest that site preferences of these systems could be related with their energy band gaps.

Chapter 8

Conclusion

This thesis has been concerned with the computational study of spinel-type potentially important oxynitride systems incorporating boron and other metals such as aluminium, gallium and indium. Using the modern computational methods for material modeling, we can simulate the properties of real materials from zero temperature to finite temperature and make prediction of new phenomena and at times explain experimental observations. In this present thesis we have applied *ab*-initio (first principles) calculations, based on density functional theory (DFT) and molecular dynamics simulation on a series of Tersoff empirical potentials on these oxynitride spinel materials which could be highly interesting materials for modern and future industrial applications.

We have presented an extensive investigation on the structural, electronic, elastic properties and the relative stabilities of the bulk and the nature of the resulting vacancies or defect-related properties of these systems. Calculations on M_2O_3 and MN (where M = B, Al, Ga and In) shows good agreement with experimental results and this have served as a benchmark for the investigation of the oxynitride spinel systems. The oxynitride structure in this thesis adopts a cubic symmetry, $P\bar{4}3m$, and described using the 56-atom unit cell as is commonly used for the spinel structure. The properties are calculated with the LDA and GGA functionals. The trends in bulk modulus as well as the relative stabilities to

M_2O_3 and MN phases are in close similarity, indicating a linear relationship between the mechanical and energetic properties of these systems. The predicted bulk modulus of these systems ranges between 160 and 350 GPa, a shear modulus between 50 and 210 GPa, and a young's modulus ob 160 and 510 GPa and we suggest that these systems with aluminium oxynitride in particular could well be potentially hard material with possible applications as industrial abrasive device. The calculated band gaps of the spinel phase of Ga and In are very similar to that of their respective binary nitrides and therefore could be a potentially important new material for various types of electronic applications. More so, results shows that the structural stability of oxynitride systems could be lowered by creating a vacant cation atoms and the formation of the defective non-stoichiometry oxynitride systems may be unfavorable.

At finite temperature, we have also predicted their thermodynamical properties such as the Debye temperature, thermal expansion co-efficient, and specific heat by using adjusted Tersoff potentials for this multi-component oxynitride systems. It is suggested that these materials will have thermal properties comparable to their binary nitride counterparts.

The present work has shown that the theoretical tools employed in this thesis have the potential not only to aid in understanding the physics of these systems but also to predict basic physical properties. This theoretical understanding could be useful for a possible synthesis of the oxynitride spinel systems of B_3NO_3, Al_3NO_3, Ga_3NO_3, and In_3NO_3.

8.1 Recommendation for Further Work

The oxynitride spinel systems, from this thesis shows that these systems are an important class of materials and are therefore open for many future research avenues. Notably among them is to find out the actual composition of the oxynitride systems. In this thesis we have employed a stoichiometric spinel composition M_3NO_3 ($1M_2O_3$:$1M$N) which is typical for spinel materials for example $MgAl_2O_4$ ($1MgO$:$1Al_2O_3$). Corbin, [221] in his work,

reported however, that the composition of the oxynitride spinel use a constant anion lattice of nitrogen and oxygen where the spinel cation vacancies decrease as the nitrogen content increases and as a result could favor a stable state spinel phase with a disordered vacancy.

A further work should also be directed to the the boron oxynitride spinel, B_3NO_3. We found out a tetragonal instability in the bulk and defective spinel phase when the value of $(c_{11} - c_{12})$ was calculated. A conclusive explanation for this behavior could not be given at this stage although we have attributed it to the asymmetric nature of B-O and B-N strong bonding in the B_3NO_3 spinel unit cell. We did check both the size of calculational displacement in the appropriate distortion of $(c_{11} - c_{12})$ and for the usual convergence criterion and have found rather this surprising result and as such it is worth investigating.

Finally, a first principle calculation of the phase transition of the oxynitride spinel systems could be a field of research with great possibilities, to determine and understand their intrinsic properties. Recently [222] it was deduced from plate impact experiments up to 180 GPa that Al oxynitride phase undergoes a phase transition at about 130 GPa, with the Al shifting from fourfold to sixfold coordination, and we now suggest that other spinel structures should be investigated in this respect.

Appendix A

Band Structures and Density of States of Defective Oxynitride Spinel

The band structures and densities of states for the defective oxynitride spinel structure are plotted in the following pages. These plots shows the octahedral (Oh) and tetrahedral (Td) vacancy sites. In the DOS-plots the x-axis is energy and the y-axis is the number of the eigenvalues (states) at a particular energy level, whereby the energy distribution are measured relative to their Fermi energy. The Fermi energy level is indicated by a vertical dotted line. The energy scale is chosen so that the Fermi energy level is located at 0 eV at which point the energy band gaps are calculated. The band structure and DOS are calculated with the local density approximation (LDA).

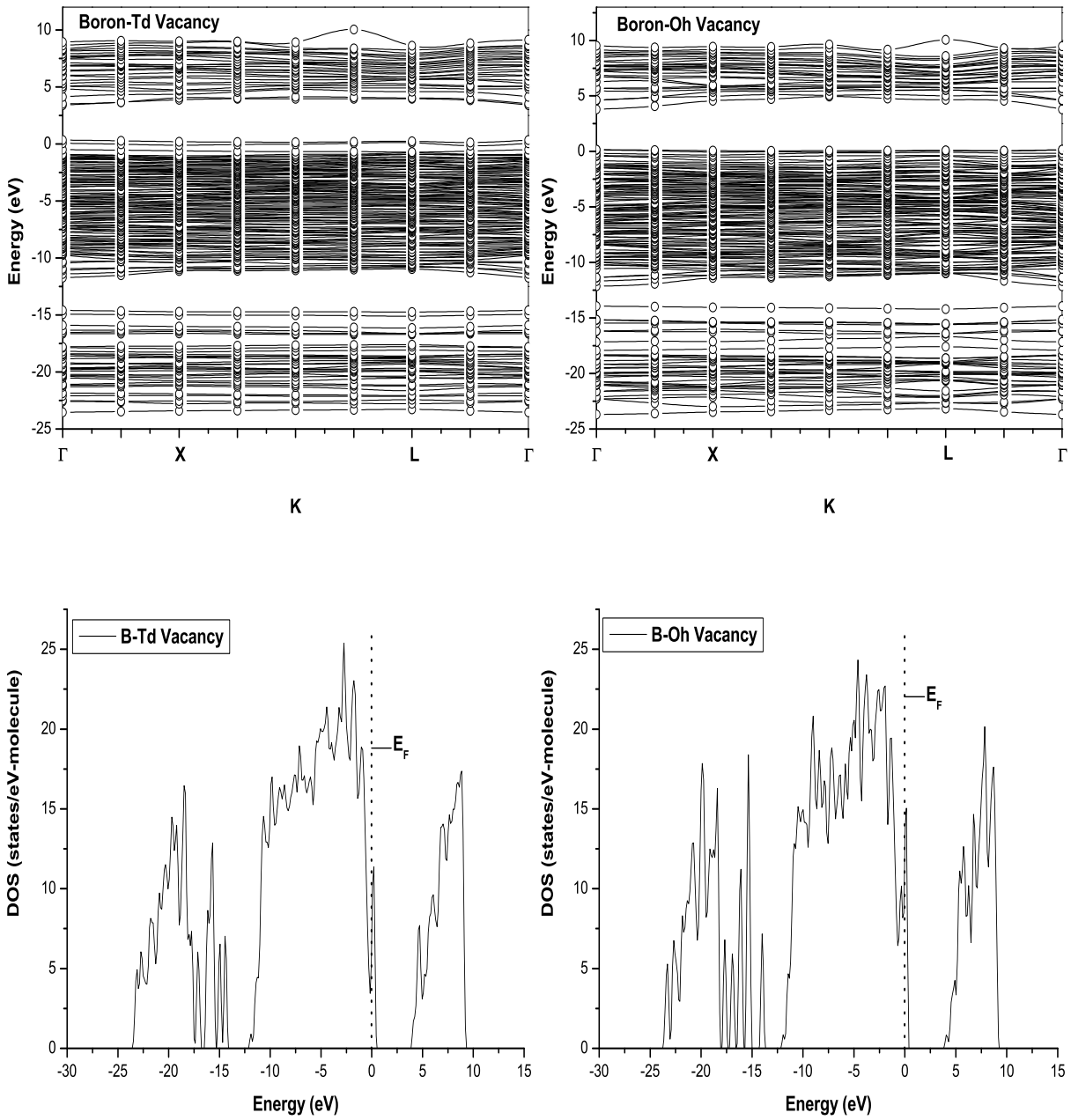


Figure A.1: Band structure and DOS of Oh and Td vacancy sites for B_3NO_3. The Fermi energy level is at zero energy.

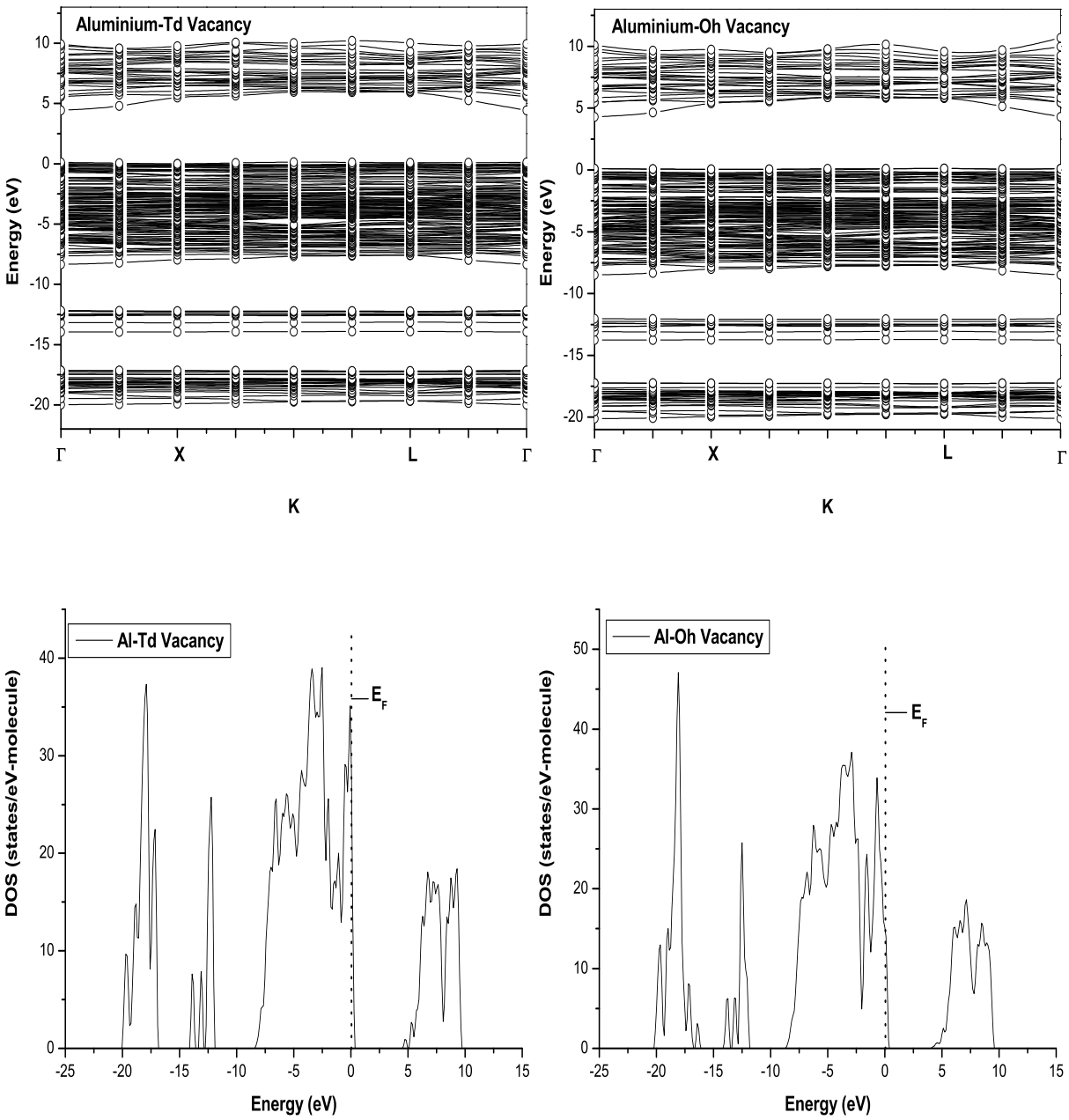


Figure A.2: Band structure and DOS of Oh and Td vacancy sites for Al_3NO_3. The Fermi energy level is at zero energy.

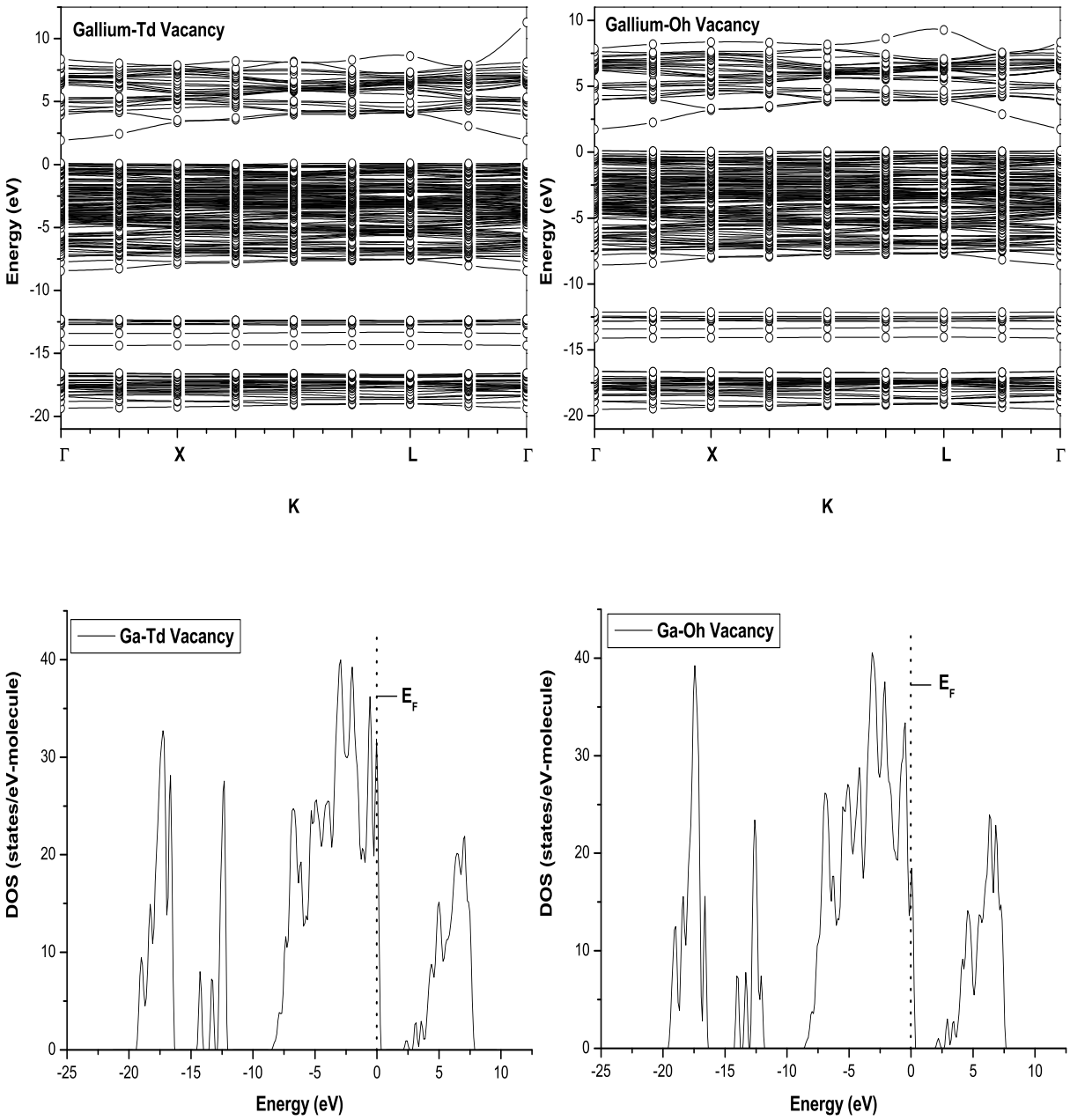


Figure A.3: Band structure and DOS of Oh and Td vacancy sites for Ga_3NO_3. The Fermi energy level is at zero energy.

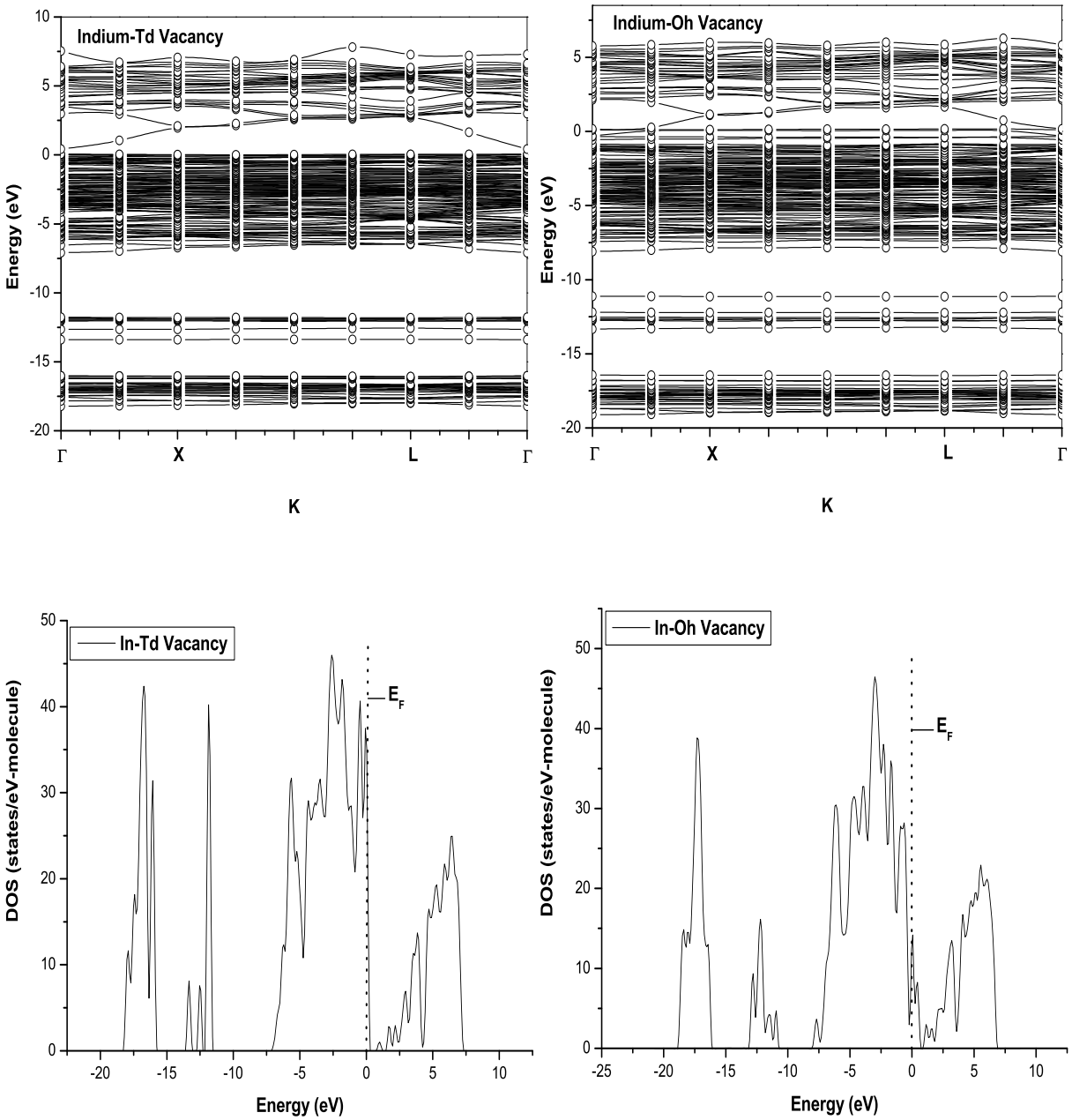


Figure A.4: Band structure and DOS of Oh and Td vacancy sites for In_3NO_3. The Fermi energy level is at zero energy.

Appendix B

RDF Plots for the Ternary Oxynitride Spinel Materials

This section shows radial distribution function (RDF) for all the pair atoms for the spinel materials. At finite temperatures, the RDF plots shows the behavior of these materials, and in particular, how the pairs of atoms in this structure are affected in terms of their peak distances. The RDF is an example of a pair correlation function, which describes how on average, the atoms in a system are radially packed around each other. We run the molecular dynamics simulation at a number of temperatures ranging from 0 K to 2500 K. Figures B.1, B.2, B.3 and B.4 display the pair distribution function for B_3NO_3, Al_3NO_3, Ga_3NO_3 and In_3NO_3 respectively. At 0 K, we see a number of obvious sharp peaks indicating that the atoms pack around each other. The occurrence of peaks at long range indicates a high degree of ordering. At higher temperatures the number of peak decreases, usually the peaks are broad, indicating thermal motion. Here we see that the peak distance is a function of temperature.

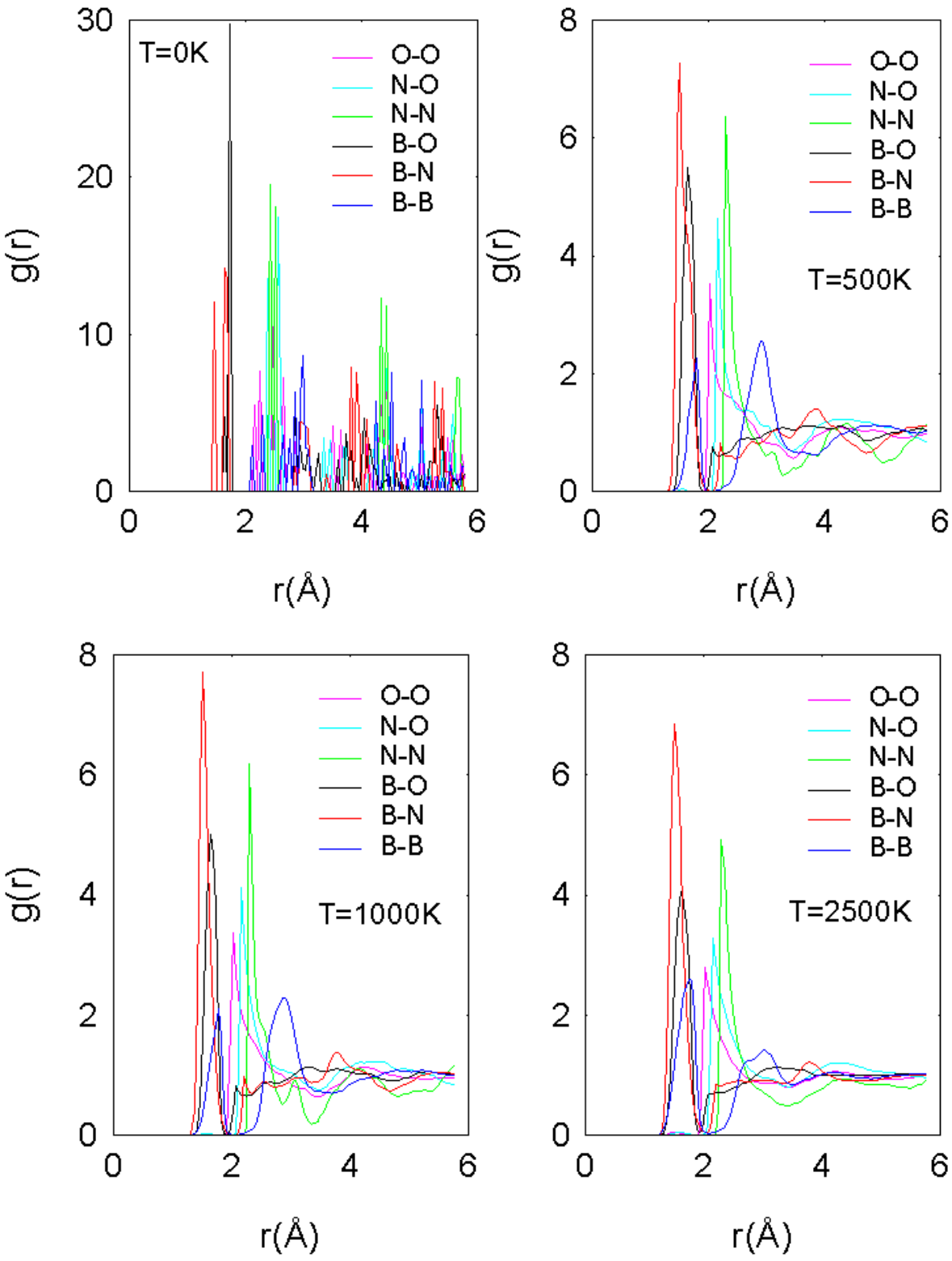


Figure B.1: Pair distribution function for B_3NO_3 at 0, 500, 1000 and 2500 K.

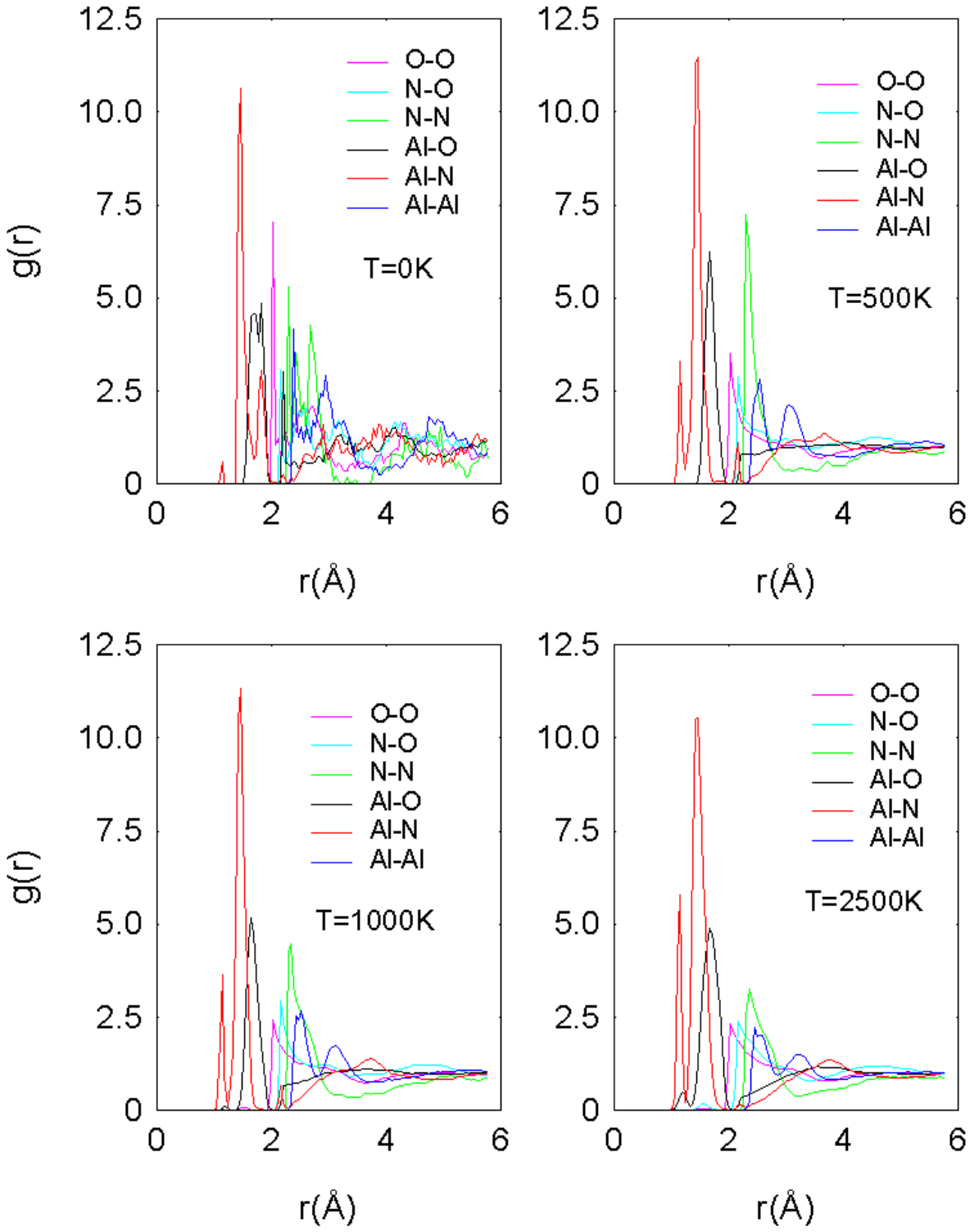


Figure B.2: Pair distribution function for Al_3NO_3 at 0, 500, 1000 and 2500 K.

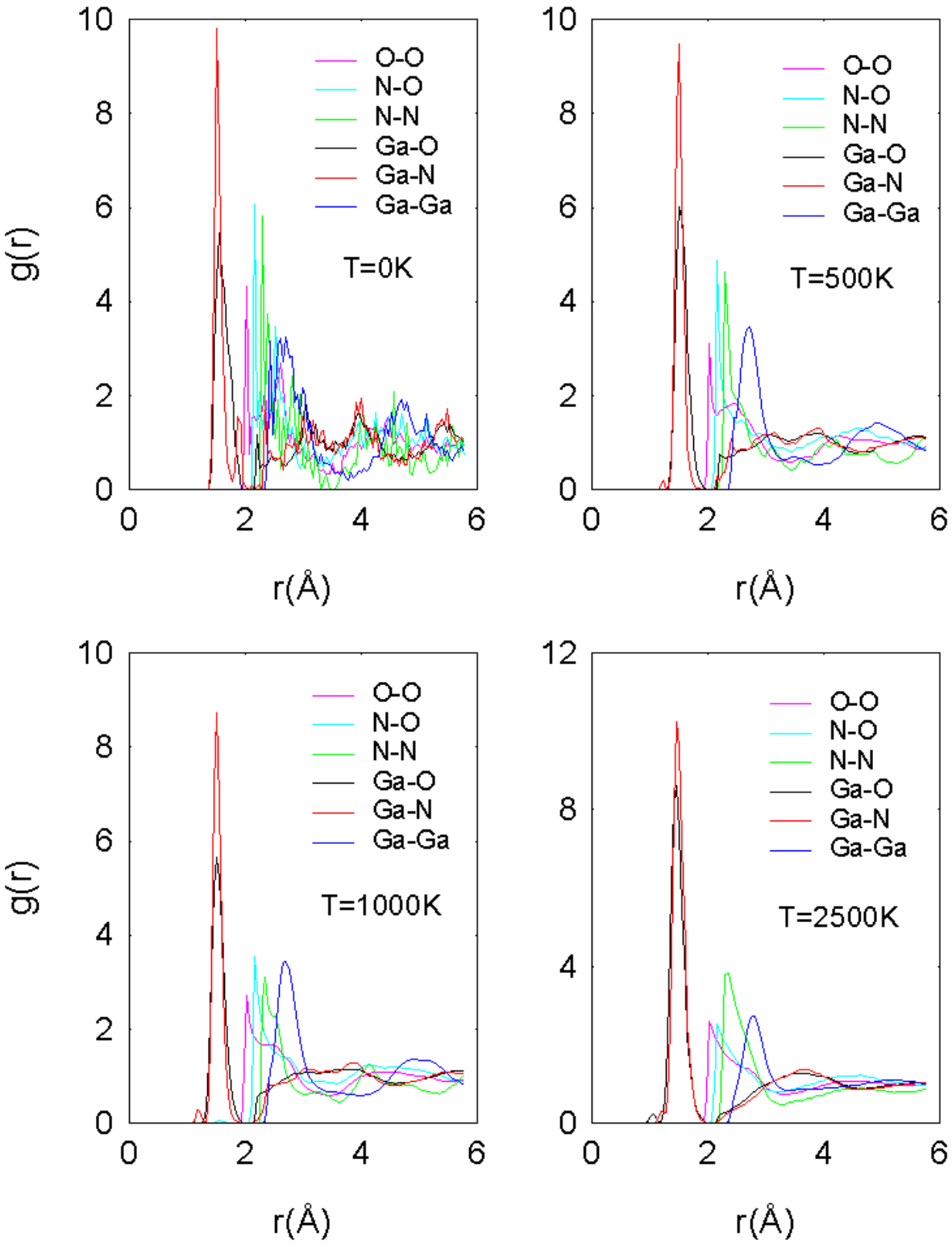


Figure B.3: Pair distribution function for Ga_3NO_3 at 0, 500, 1000 and 2500 K.

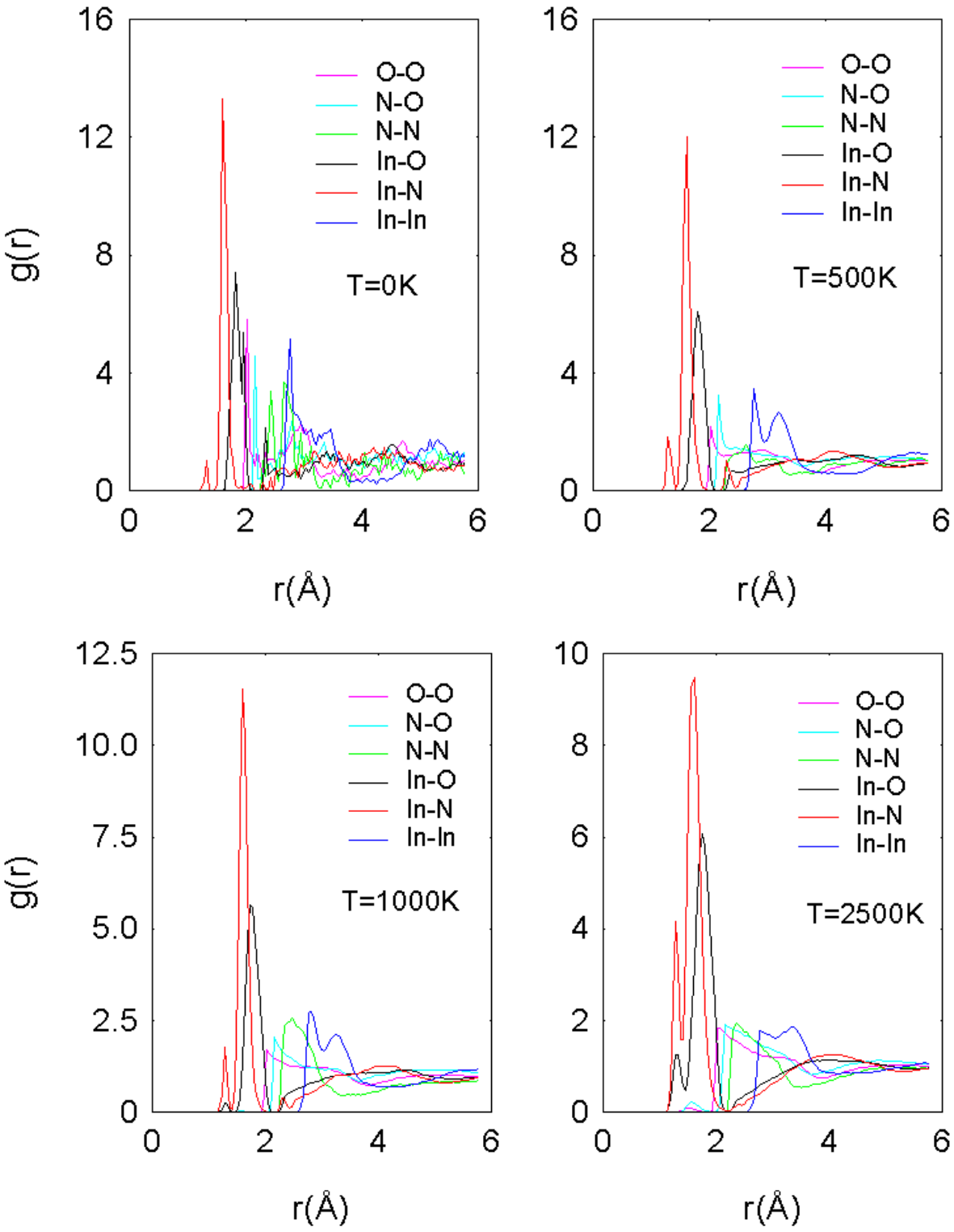


Figure B.4: Pair distribution function for In_3NO_3 at 0, 500, 1000 and 2500 K.

References

[1] R. Riedel (Ed.), Hand Book of Ceramic Hard Materials, Vol. 1, WILEY-VCH, Weinheim, 2000.

[2] M. T. Futschek, Structural, electronic and magnetic properties of transition metal clusters., Ph.D. thesis, Institute für Materialphysik, Center for Computational Materials Science, Universität Wein (2005).

[3] Z. Y. Chen, H. J. Xiang, J. Yang, J. G. Hou, Q. Zhu, cond-mat/0508506.

[4] M. Mattesini, S. F. Mater, Phys. Rev. B 65 (2002) 075110.

[5] C.-M. Sung, M. Sung, Mat. Chem. and Phys. 43 (1996) 1–18.

[6] A. Zerr, R. Riedel, T. Sekine, J. E. Lowther, W.-Y. Ching, I. Tanaka, Advanced Materials 18 (2006) 107.

[7] S. Group, Http://mineral.galleries.com/minerals/oxides/spinel.htm.

[8] B. A. Cook, J. L. Harringa, T. L. Lewis, A. M. Russell, Scripta Mater. 42 42 (2000) 597.

[9] H. W. Hugusson, A theoretical treatise on the electronic structure designer hard materials, Ph.D. thesis, Uppsala University (2001).

[10] F. Gao, Phys. Rev. B 65 (2004) 094113.

[11] S. Vepřek, J. Vac. Sci. Technol. A 17 (1999) 2401.

[12] D. G. Clerc, J. Phys. Chem. Sol. 60 (1999) 103.

[13] J. M. Léger, J. Haines, B. Blanzat, J. Mater. Sci. Lett. 13 (1994) 1688.

[14] J. M. Léger, P. Djemia, F. Ganot, J. Haines, A. S. Pereira, J. A. H. Da Jornada, Appl. Phys. Lett. 79 (2001) 2169.

[15] J. K. Dewhurst, Computational modeling of superhard metal dioxides, Ph.D. thesis, University of the Witwatersrand, Johannesburg (1999).

[16] A. Beads, Http://www.africajohns.com/glossaryrz.htm.

[17] E. M. Yoshimura, E. G. Yukihara, Radiation Measurement 41 (2006) 163.

[18] D. Bacorisen, R. Smith, J. A. Ball, R. W. Grimes, B. P. Uberuaga, K. E. Sickafus, W. T. Rankin, Nuclear Instruments and Methods in Physics Research B 250 (2006) 36.

[19] F. C. Romeijn, Physical and Crystallographical Properties of Some, Eindhoven Press, 1953.

[20] J. M. Recio, R. Franco, M. Pendas, M. A. Blanco, L. Pueyo, Phys. Rev. B 63 (2001) 184101.

[21] K. E. Sickafus, J. M. Wills, N. W. Grimes, J. Am Ceram. Soc. 82 (1999) 3279.

[22] J. E. Lowther, M. Schwarz, E. Kroke, R. Riedel, J. Solid State Chem 176 (2003) 549.

[23] T. Mathew, Synthesis and characterization of mixed oxides containing cobalt, copper and iron and study of their catalytic activity, Ph.D. thesis, University of Pune, Indian (2002).

[24] W. Y. Ching, M. Shang-Di, I. Tanaka, M. Yoshiya, Phys. Rev. B 63 (2001) 064102.

[25] E. J. W. Verwey, F. D. Boer, J. H. V. Santen, J. Chem. Phys. 16 (1948) 1091.

[26] T. F. W. Barth, E. Ponsnjak, Zeits F. Kristall 82 (1932) 325.

[27] E. J. W. Verwey, E. L. Heilman, J. Chem. Phys. 15 (1947) 174.

[28] W. Y. Ching, M. Shang-Di, L. Ouyang, I. Tanaka, M. Yoshiya, Phys. Rev. B 61 (2000) 10609.

[29] O. M. Moon, B. C. Kang, J. H. Boo, Thin Solid Films 464-465 (2004) 164.

[30] D. Halil, S. Ömer, S. I. Mehmet, F. Hassan, Thermochimica Acta 445 (2006) 1.

[31] M. Renzhi, B. Yoshio, Chem. Phys. lett. 374 (2003) 358.

[32] W. H. Zachariasen, J. Am. Chem. Soc. 54 (1932) 3841.

[33] J. Krogh-Moe, J. Non-Cryst. Solids 1 (1969) 269.

[34] S. J. Hwang, C. Fernandez, J. P. Amoureux, J. Cho, S. W. Martin, Solid State Nucl. Magn. Reson. 8 (1997) 109.

[35] L. Huang, J. Kieffer, Phys. Rev. B 74 (2006) 224107.

[36] J. Seung-Hoon, K. Young-Kyun, Phys. Rev. B 71 (2005) 035408.

[37] G. Simon, B. Hehlen, E. Courtens, E. Longueteau, R. Vacher, Phys. Rev. Lett. 96 (2006) 105502.

[38] J. Swenson, L. Börjesson, Phys. Rev. B 55 (1997) 11138.

[39] G. E. Gurr, P. W. Montgomery, C. D. Knutson, B. T. Gorres, Acta Cryst. B 26 (1970) 906.

[40] C. T. Prewitt, R. D. Shannon, Acta Cryst. B 24 (1968) 869.

[41] N. S. Delia, L. Paul, C. Wilson, M. Mohamed, Phys. Rev. B 70 (2004) 214108.

[42] G. Paglia, A. L. Rohl, C. E. Buckley, J. D. Gale, Phys. Rev. B 71 (2005) 224115.

[43] R. H. French, H. Müllejans, D. J. Jones, J. Am. Ceram. Soc. 81 (1998) 2549.

[44] A. Khanna, D. G. Bhat, Surf. Coat. Tech. 201 (2006) 168.

[45] S. Cava, S. M. Tebcherani, S. A. Pianaro, C. A. Paskocimas, E. Longo, J. A. Varela, Mater. Chem. and Phys. 97 (2006) 102.

[46] Y. Y. Park, S. O. Lee, T. Tran, S. J. Kim, M. J. Kim, Int. J. Miner. Process. 80 (2006) 126.

[47] B. C. Lippens, J. H. d. Boer, Acta Cryst. 17 (1964) 1312.

[48] S. Jahn, P. A. Madden, M. Wilson, Phys. Rev. B 74 (2006) 024112.

[49] S.-D. Mo, W. Y. Ching, Phys. Rev. B 57 (1998) 15219.

[50] C. Wolverton, K. C. Hass, Phys. Rev. B 63 (2000) 024102.

[51] B. W. Veal, A. P. Paulikas, R. C. Birtcher, Appl. Phys. Lett. 89 (2006) 161916.

[52] R. S. Zhou, R. L. Snyder, Acta Crystallogr. , Sect. B: Struct. Sci. 47 (1991) 617.

[53] M. Nieminen, L. Niinistö, E. Rauhala, J. Mater. Chem. 6(1) (1996) 27.

[54] X. Liu, G. Qiu, Y. Zhao, N. Zhang, R. Yi, J. Alloys and Compd. 439 (2007) 275.

[55] S. Sharma, M. K. Sunkara, J. Am. Chem. Soc. 124 (2002) 12288.

[56] B. Cheng, E. T. Samulski, J. Mater. Chem. 11 (2001) 2901.

[57] S. E. Collins, M. A. Baltanás, A. L. Bonivardi, J. Phys. Chem. B 110 (2006) 5498.

[58] R. Roy, V. G. Hill, E. F. Osborn, J. Am. Chem. Soc. 74 (1952) 719.

[59] G. Sinha, K. Adhikary, S. Chaudhuri, J. Cryst. Growth 276 (2005) 204.

[60] Y. Hou, L. Wu, X. Wang, Z. Ding, Z. Li, X. Fu, J. Catal. 250 (2007) 12.

[61] H. D. Xiao, H. L. Ma, W. Liang, C. S. Xue, H. Z. Zhuang, J. Ma, W. R. Hu, Mater. Chem. Phys. 94 (2005) 261.

[62] D. D. Edwards, P. E. Folkins, T. O. Mason, J. Am. Ceram. Soc. 80 (1997) 253.

[63] S. Cho, J. Lee, I. Y. Park, S. Kim, Mater. Lett. 57 (2002) 1004.

[64] H. Xie, L. Chen, Y. Liu, K. Huang, Solid State. Commun. 141 (2007) 12.

[65] A. F. Pasquevich, M. Uhrmacher, L. Ziegeler, K. P. Lieb, Phys. Rev. B 48 (1993) 10052.

[66] D. Yu, D. Wang, Y. Qian, J. Solid State Chem. 177 (2004) 1234.

[67] S. Luo, W. Zhuo, Z. Zhang, J. Shen, L. Liu, W. Ma, X. Zhao, D. Liu, L. Song, Y. Xiang, J. Zhou, S. Xie, W. Chu, Appl. Phys. Lett. 89 (2006) 093112.

[68] Y. Liu, W. Yang, D. Hou, Superlattices Microstructures In Press.

[69] C. Y. Wang, V. Cimalla, H. Romanus, T. Kups, G. Ecke, T. Stauden, M. Ali, V. Lebedev, J. Pezoldt, O. Ambacher, Appl. Phys. Lett. 89 (2006) 011904.

[70] S. Z. Karazhanov, P. Ravindran, P. Vajeeston, A. Ulyashin, T. G. Finstad, H. Fjellvag, Phys. Rev. B 76 (2007) 075129.

[71] R. D. Shannon, Solid State Commun. 4 (1966) 629.

[72] I. Tanaka, M. Mizuno, H. Adachi, Phys. Rev. B 56 (1997) 3536.

[73] K. Kim, W. R. L. Lambrecht, B. Segall, Phys. Rev. B 53 (1996) 16310.

[74] K. Karch, F. Bechstedt, Phys. Rev. B 56 (1997) 7404.

[75] K. Lawniczak-Jablonska, T. Suski, I. Gorczyca, N. E. Christensen, K. E. Attenkofer, R. C. C. Perera, E. M. Gullikson, J. H. Underwood, D. L. Ederer, Z. L. Weber, Phys. Rev. B 61 (2000) 16623.

[76] V. A. Gubanov, Z. W. Lu, B. M. Klein, C. Y. Fong, Phys. Rev. B 53 (1996) 4377.

[77] J. Olander, K. Larsson, Phys. Rev. B 68 (2003) 075411.

[78] A. Bosak, J. Serrano, M. Krisch, K. Watanabe, T. Taniguchi, H. Kanda, Phys. Rev. B 73 (2006) 041402.

[79] J. B. MacNaughton, A. Moewes, R. G. Wilks, X. T. Zhou, T. K. Sham, T. Taniguchi, K. Watanabe, C. Y. Chan, W. J. Zhang, B. I., S. T. Lee, H. Hofsäss, Phys. Rev. B 72 (2005) 195113.

[80] H. Sachdev, R. Haubner, H. Nöth, B. Lux, Diamond Relat. Mater. 6 (1997) 286.

[81] S. Bohr, R. Haubner, B. Lux, Diamond. Relat. Mater. 4 (1995) 714.

[82] G. Satta, G. Cappellini, V. Olevano, L. Reining, Phys. Rev. B 70 (2004) 195212.

[83] A. C. Ferrari, S. Reich, R. Arenal, A. Loiseau, I. Bello, J. Robertson, Phys. Rev. B 71 (2005) 205201.

[84] M. J. Paisley, R. F. Davis, J. Cryst. Growth 127 (1993) 136.

[85] F. Litimein, B. Bouhafs, Z. Dribi, P. Ruterana, New J. Phys. 4 (2002) 64.

[86] V. Darakchieva, B. J., M. Schubert, T. Paskova, S. Tungasmita, G. Wagner, A. Kasic, B. Monemar, Phys. Rev. B 70 (2004) 045411.

[87] N. Nepal, K. B. Nam, J. Li, M. L. Nakarmi, J. Y. Lin, H. X. Jiang, Appl. Phys. Lett. 88 (2006) 261919.

[88] I. Vurgaftman, J. R. Meyer, J. Appl. Phys. 94 (2003) 3675.

[89] E. Oh, J. H. Choi, H. K. Seong, H. J. Choi, Appl. Phys. Lett. 89 (2006) 092109.

[90] J. Serrano, A. Rubio, E. Hernández, A. Muñoz, A. Mujica, Phys. Rev. B 62 (2000) 16612.

[91] A. Zoroddu, F. Bernardini, P. Ruggerone, V. Fiorentini, Phys. Rev. B 64 (2001) 045208.

[92] R. Miotto, G. P. Srivastava, A. C. Ferraz, Phys. Rev. B 59 (1999) 3008.

[93] G. Chris, V. d. Walle, J. Neugebauer, J. Appl. Phys. 95 (2004) 3851.

[94] A. G. Bhuiyan, A. Hashimoto, A. Yamamoto, J. Appl. Phys. 94 (2003) 2779.

[95] S. N. Mohammad, H. Morkoc, Prog. Quantum Electron 20 (1996) 361.

[96] I. J. Lee, H. J. Shin, S. S. Chang, Appl. Phys. Lett. 82 (2003) 2981.

[97] V. Cimalla, J. Pezoldt, G. Ecke, R. Kosiba, O. Ambacher, Spieß, G. Teichert, H. Lu, W. J. Schaff, Appl. Phys. Lett. 83 (2003) 3468.

[98] W. Kohn, Rev. Mod. Phys. 71 (1999) 1253.

[99] J. A. Pople, Rev. Mod. Phys. 71 (1999) 1267.

[100] W. Koch, M. C. Holthausen, A Chemist's Guide to Density Functional Theory, WILEY-VCH, 2001.

[101] R. G. Parr, W. Yang, Density-Functional Theory of Atoms and Molecules, Oxford University Press, New York, 1989.

[102] D. Joubert (Ed.), Density Functionals: Theory and Applications, Springer Lecture Notes in Physics Vol. 500, 1998.

[103] P. Hohenberg, W. Kohn, Phys. Rev. B 136 (1964) 864.

[104] W. Kohn, L. J. Sham, Phys. Rev. A 140 (1965) 1133.

[105] M. C. Payne, M. P. Teter, D. C. Allan, T. A. Arias, J. D. Joannopoulos, Rev. Mod. Phys. 64 (1992) 1045.

[106] R. M. Martin, Electronic Structure: Basic Theory and Practical Methods, Cambridge University Press, 2004.

[107] P. A. M. Dirac, Proc. Cambridge Phil. Soc. 26 (1930) 376.

[108] D. M. Ceperley, B. J. Alder, Phys. Rev. Lett. 45 (1980) 566.

[109] L. Hedin, B. Lundqvist, J. Phys. C 4 (1971) 2064.

[110] S. H. Vosko, L. Wilk, M. Nusair, Can. J. Phys. 58 (1980) 1200.

[111] J. P. Perdew, A. Zunger, Phys. Rev. B 23 (1981) 5048.

[112] J. P. Perdew, Y. Wang, Phys. Rev. B 45 (1992) 13244.

[113] J. P. Perdew, K. Burke, M. Ernzerhof, Phys. Rev. Lett. 77 (1996) 3865.

[114] A. D. Becke, Phys. Rev. A 38 (1988) 3098.

[115] M. Filatov, W. Thiel, Mol. Phys. 91 (1997) 847.

[116] J. P. Perdew, J. A. Chevary, S. H. Vosko, K. A. Jackson, M. R. Pederson, D. J. Singh, C. Fiolhais, Phys. Rev. B 46 (1992) 6671.

[117] G. J. Laming, N. C. Termath, V. Handy, J. Chem. Phys. 99 (1993) 8765.

[118] G. J. Laming, N. C. Handy, R. D. Amos, Mol. Phys. 80 (1993) 1121.

[119] A. D. Berke, J. Chem. Phys. 84 (1986) 4524.

[120] D. J. Lacks, R. G. Gordon, Phys. Rev. A 47 (1993) 4681.

[121] N. W. Ashcroft, N. D. Mermin, Solid State Physics, Saunders College, Philidelphia, 1976.

[122] H. J. Monkhorst, J. D. Pack, Phys. Rev. B 13 (1976) 5188.

[123] G. B. Bachelet, D. R. Hamann, M. Schlüter, Phys. Rev. B 25 (1982) 2103.

[124] L. Kleinman, D. Bylander, Phys. Rev. Lett. 48 (1982) 1425.

[125] D. Vanderbilt, Phys. Rev. B 41 (1990) 7892.

[126] N. Troullier, J. L. Martins, Phys. Rev. B 43 (1991) 1993.

[127] P. E. Blöchl, Phys. Rev. B 50 (1994) 17953.

[128] G. Kresse, D. Joubert, Phys. Rev. B 59 (1999) 1758.

[129] G. Kresse, J. Hafner, Phys. Rev. B 47 (1993) 558.

[130] G. Kresse, J. Hafner, Phys. Rev. B 49 (1994) 14251.

[131] G. Kresse, J. Furthmüller, Phys. Rev. B 54 (1996) 11169.

[132] G. Kresse, J. Furthmüller, Computat. Mater. Sci. 6 (1996) 15.

[133] D. J. Chadi, M. L. Cohen, Phys. Rev. B 8 (1973) 5747.

[134] J. E. Lowther, M. Wagner, K. Isabel, R. Riedel, J. Alloy and Compd. 376 (2004) 1.

[135] P. Kroll, Phys. Rev. B 72 (144407) 2005.

[136] P. Kroll, R. Dronskowski, M. Martin, J. Mater. Chem. 15 (2005) 3296.

[137] E. Soignard, D. Machon, D. M. McMillan, B. Dong, J. Xu, K. Leinenweber, Chem. Mater. 17 (2005) 5465.

[138] L. W. Finger, R. M. Hazen, J. Appl. Phys. 49 (1978) 5823.

[139] C. Y. Wang, V. Cimalla, H. Romanus, T. Kups, G. Ecke, T. Stauden, M. Ali, Appl. Phys. Lett. 89 (2006) 011904.

[140] R. W. G. Wyckoff, Crystal Structures, Interscience, New York, 1948.

[141] C. Kittel, Introduction to Solid State Physics, 6th Edition, Wiley, New York, 1986.

[142] F. D. Murnaghan, Proc. Natl. Acad. Sci. U.S.A. 30 (1944) 244.

[143] F. Birch, Phys. Rev. 71 (1947) 809.

[144] F. Birch, J. Geophys. Res 83 (1978) 1257.

[145] P. Vinet, J. Ferrante, J. R. Smith, J. H. Rose, J. Phys. C 19 (1986) L467.

[146] P. Vinet, J. Ferrante, J. H. Rose, J. R. Smith, J. Geophys. Res. 92 (1987) 9319.

[147] P. Vinet, J. Rose, J. H.and Ferrante, J. R. Smith, J. Phys.: Condens Matter 1 (1989) 1941.

[148] E. Knittle, A. Rudy, R. Jeanloz, Phys. Rev. B 31 (1985) 588.

[149] R. Jeanloz, Phys. Rev. B 38 (1988) 805.

[150] C. M. Fang, R. Metselaar, H. T. Hintzen, G. D. With, J. Am. Ceram. Soc. 84 (2001) 2633.

[151] C. Filippi, D. J. Singh, C. J. Umrigar, Phys. Rev. B 50 (1994) 14947.

[152] S. Shang, Y. Wang, Z. K. Liu, Appl. Phys. Lett. 90 (2007) 101909.

[153] D. Machon, P. F. McMillan, B. Xu, J. Dong, Phys. Rev. B 73 (2006) 094125.

[154] J. F. Nye, Physical Properties of Crystals, Their Representation by Tensors and Matrices, Oxford University Press, 1957.

[155] D. C. Wallace, Thermodynamics of Crystals, Wiley, New York, 1972.

[156] O. U. Okeke, J. E. Lowther, Phys. Rev. B 77 (2008) 094129.

[157] F. Bechstedt, J. Furhmüller, J. Crystal Growth 246 (2002) 315.

[158] K. Matsunaga, C. Fisher, H. Matsubara, Jpn. J. Appl. Phys. 39 (2000) L48.

[159] J. M. Haile, Molecular Dynamics Simulation: Elementary Methods, Wiley, New York, 1992.

[160] N. Ogbonna, Http://www.aims.ac.za/resources/archive/2003.php.

[161] L. Hong Li, A computational study of lattice relaxation about defects in diamond, Master's thesis, University of the Witwatersrand, Johannesburg (1995).

[162] I. T. Todorov, N. L. Allan, J. A. Purton, M. T. Dove, W. Smith, J. Mater. Sci. 42 (2007) 1920.

[163] B. J. Alder, T. E. Wainwrite, J. Chem. Phys. 27 (1957) 1208.

[164] B. J. Alder, T. E. Wainwrite, J. Chem. Phys. 31 (1959) 459.

[165] W. Smith, The CCP5 Molecular Simulation Summer School, Sheffield University, Collaborative Computational Project (2008).

[166] M. P. Allen, D. J. Tildesley, Computer Simulation of Liquids, Clarendon Press, Oxford, 1987.

[167] T. I. Todorov, W. Smith, Phil. Trans. R. Soc. Lond. A 362 (2004) 1835.

[168] J. F. Ziegler, J. P. Biersack, U. Littmark, The Stopping and Range of Ions in Solids, Pergamon Press, New York, U.S.A, 1985.

[169] F. H. Stillinger, T. A. Weber, Phys. Rev. B 31 (1985) 5262.

[170] D. W. Brenner, Phys. Rev. B 42 (1990) 9458.

[171] M. W. Finnis, Phil. Mag. A 50 (1984) 45.

[172] J. Tersoff, Phys. Rev. Lett. 56 (1986) 632.

[173] Wikipedia, Http://en.wikipedia.org/wiki/bond_order_potential.

[174] J. Tersoff, Phys. Rev. B 37 (1988) 6991.

[175] J. Tersoff, Phys. Rev. B 38 (1988) 9902.

[176] J. Tersoff, Phys. Rev. B 39 (1989) 5566.

[177] M. Nakamura, H. Fujioka, K. Ono, M. Takeuchi, T. Mitsui, M. Oshima, J. crystal Growth 209 (2000) 232.

[178] D. Conrad, K. Scheerschmidt, Phys. Rev. B 58 (1998) 4538.

[179] K. Matsunaga, Y. Iwamoto, J. Am. Ceram. Soc. 84 (2001) 2213.

[180] Y. Umeno, T. Kitamura, K. Date, M. Hayashi, T. Iwasaki, Compt. Mater. Sci. 25 (2002) 447.

[181] S. Muneto, T. Motooka, K. Moriguchi, A. Shintani, Comp. Mater. Sci. 39 (2007) 334.

[182] W. Sekkal, A. Laref, H. Aourag, A. Zaoui, M. Certier, Superlatticess Microstruct. 28 (2000) 55.

[183] W. Sekkal, H. Aourag, M. Certier, J. Phys. Chem. Solids 59 (1998) 1293.

[184] F. Benkabou, M. Certier, H. Aourag, Mol. Sim. 29 (2003) 201.

[185] J. Nord, K. Nordlund, K. Albe, Nucl. Instrum. Meth. B 202 (2003) 93.

[186] K. Albe, W. Möller, Comp. Mater. Sci. 10 (1998) 111.

[187] I. Todorov, W. Smith, The Dlpoly 3 User Manual, STFC Daresbury Laboratory Daresbury, Warrington WA4 4AD Cheshire, UK (2008).

[188] D. Powell, A. Migliorato, A. G. Cullis, Phys. Rev. B 75 (2007) 9.

[189] P. M. Kroll, Ph.D. thesis, Technische Hochschule Darmstadt (1996).

[190] S. Munetoh, T. Motooka, K. Moriguchi, A. Shintani, Comput. Mater. Sci. 23 (2007) 617.

[191] D. Frenkel, B. Smit, Understanding Molecular Simulations: From Algorithms to Applications, Academic Press, London, 2002.

[192] J. D. Gale, A. L. Rohl, Mol. Simul. 29 (2003) 291.

[193] J. D. Gale, J. Phys. Chem. B 102 (1998) 5423.

[194] C. R. Ross II, S. L. Webb, J. Appl. Cryst. 23 (1990) 439.

[195] J. W. Kang, H. J. Hwang, Comp. Mater. Sci. 31 (2004) 237.

[196] O. U. Okeke, J. E. Lowther, Physica B, 404 (2009) 3577.

[197] W. H. Moon, M. S. Son, H. J. Hwang, Physica B 336 (2003) 329.

[198] E. Ruiz, S. Alvarez, Phys. Rev. B 49 (1994) 7115.

[199] M. E. Sherwin, T. J. Drummond, J. Appl. Phys. 69 (1991) 8423.

[200] A. F. Wright, J. Appl. Phys. 82 (1997) 2833.

[201] W. H. Moon, H. J. Hwang, Phys. Lett. A 315 (2003) 319.

[202] M. Iuga, G. Steinle-Neumann, J. Meinhardt, Eur. Phys. J. B 58 (2007) 127.

[203] M. Ferhat, A. Zaoui, M. Certier, H. Aourag, Physica B 252 (1998) 229.

[204] M. Grimsditch, E. S. Zouboulis, A. Polian, J. Appl. Phys. 76 (1994) 832.

[205] S. Y. Davydov, Semicondoctors 36 (2002) 41.

[206] W. Sekkal, H. Aourag, M. Certier, Comput. Mater. Sci. 9 (1998) 295.

[207] Y. D. Guo, X. S. Song, X. B. Li, X. D. Yang, Solid State Commun. 141 (2007) 577.

[208] W. Sekkal, A. Zaoui, A. Laref, H. Aourag, M. Certier, J. Phys.: Condens. Matter 11 (1999) 3875.

[209] W. Sekkal, B. Bouhafs, H. Aourag, M. Certier, J. Phys.: Condens. Matter 10 (1998) 4975.

[210] S. Goumri-Said, M. B. Kanoun, A. E. Merad, G. Merad, H. Aourag, Chem. Phys. 302 (2004) 135.

[211] F. Benkabou, P. Becker, M. Certier, H. Aourag, Phys. Stat. Sol. (b) 209 (1998) 223.

[212] J. E. Field, Properties of Diamond, Academic Press, London, 1979.

[213] T. Tohei, A. Kuwabara, F. Oba, I. Tanaka, Phys. Rev. B 73 (2006) 064304.

[214] G. A. Slack, S. F. Bartram, J. Appl. Phys. 46 (1975) 89.

[215] L. Bergman, M. T. McClure, J. T. Glass, R. J. Nemanich, J. Appl. Phys. 76 (1994) 3020.

[216] V. Baykov, Point defect interactions and structural stability of compounds, Ph.D. thesis, Royal Institute of Technology, Stockholm, Sweden (2008).

[217] M. Spaeth, J, J. R. Niklas, R. H. Bartram, Structural Analysis of Point Defects in Solids, Springer-Verlag, Heidelberg, 1992.

[218] H. X. Willems, G. D. With, R. Metselaar, R. B. Helmholdt, K. K. Petersen, J. Mater. Sci. Lett. 12 (1993) 1470.

[219] J. W. McCauley, J. Am. Ceram. Soc. 61 (1978) 372.

[220] P. Tabary, C. Servant, J. Appl. Cryst. 32 (1999) 241.

[221] N. D. Corbin, J. Eur. Ceram. Soc. 5 (1989) 143.

[222] T. Sekine, X. Li, T. Kobayashi, Y. Yamashita, P. Patel, J. W. McCauley, J. Appl. Phys. 94 (2003) 4803.

Conferences and Workshops

- O. U. Okeke and J. E. Lowther, Electronic Structures and Stability of a Novel Spinel Structure (DST/NRF Center of Excellence in Strong Materials Annual Workshop, Johannesburg, April, 2007) [***Poster Presentation***].

- Onyekwelu Okeke and J. E. Lowther, Electronic Structures and Stability of a Novel Spinel Structure by *Ab initio* Calculations, (South African Institute of Physics (SAIP), Johannesburg, July, 2007) [***Oral Presentation***].

- Onyekwelu U. Okeke and J. E. Lowther, Theoretical Electronic Structures and Relative Stabilities of the Spinel Oxynitrides M_3NO_3 (M = B, Al, Ga, In) (School of Physics, Wits University, Johannesburg, April, 2008) [***Oral Presentation***].

- Onyekwelu U. Okeke and J. E. Lowther, Theoretical Electronic Structures and Relative Stabilities of the Spinel Oxynitrides M_3NO_3 (M = B, Al, Ga, In) (DST/NRF Center of Excellence in Strong Materials Annual Workshop, Johannesburg, April, 2008) [***Oral Presentation***].

- Onyekwelu U. Okeke and J. E. Lowther, Electronic Structures and Relative Stabilities of the Spinel Oxynitrides M_3NO_3 (M = B, Al, Ga, In) (CCP5 Summer School 2008, University of Sheffield, UK) [***Poster Presentation***].

- Onyekwelu U. Okeke and J. E. Lowther, Electronic Structures and Relative Stabilities of the Spinel Oxynitrides M_3NO_3 (M = B, Al, Ga, In) (Postgraduate Cross Faculty Symposium, Wits University, Johannesburg, November, 2008) [***Oral Presentation***].